

Search for Excited Charged Leptons in Electron-Positron Collisions

by

Brigitte Marie Christine Vachon

B.Sc., McGill University, 1997

A Dissertation Submitted in Partial Fulfillment of the
Requirements for the Degree of

DOCTOR OF PHILOSOPHY

in the Department of Physics and Astronomy.

We accept this dissertation as conforming
to the required standard

Dr. R. McPherson, Co-supervisor (Department of Physics and Astronomy)

Dr. R. Sobie, Co-supervisor (Department of Physics and Astronomy)

Dr. A. Astbury, Departmental Member (Department of Physics and Astronomy)

Dr. R.K. Keeler, Departmental Member (Department of Physics and Astronomy)

Dr. D. Harrington, Outside Member (Department of Chemistry)

Dr. D. Hanna, External Examiner (Department of Physics, McGill University)

© Brigitte Marie Christine Vachon, 2002
University of Victoria

All rights reserved. This dissertation may not be reproduced in whole or in part, by
photocopying or other means, without the permission of the author.

Co-supervisor: Dr. R. McPherson

Co-supervisor: Dr. R. Sobie

Abstract

A search for evidence that fundamental particles are made of smaller constituents is performed. The existence of excited states of fundamental particles would be an unambiguous indication of their composite nature. Experimental signatures compatible with the production of excited states of charged leptons in electron-positron collisions are studied. The data analysed were collected by the OPAL detector at the LEP collider. No evidence for the existence of excited states of charged leptons was found. Upper limits on the product of the cross-section and the electromagnetic branching fraction are inferred. Using results from the search for singly produced excited leptons, upper limits on the ratio of the excited lepton coupling constant to the compositeness scale are calculated. From pair production searches, 95% confidence level lower limits on the masses of excited electrons, muons and taus are determined to be 103.2 GeV.

Examiners:

Dr. R. McPherson, Co-supervisor (Department of Physics and Astronomy)

Dr. R. Sobie, Co-supervisor (Department of Physics and Astronomy)

Dr. A. Astbury, Departmental Member (Department of Physics and Astronomy)

Dr. R.K. Keeler, Departmental Member (Department of Physics and Astronomy)

Dr. D. Harrington, Outside Member (Department of Chemistry)

Dr. D. Hanna, External Examiner (Department of Physics, McGill University)

Contents

Abstract	ii
Contents	iii
List of Tables	iv
List of Figures	v
Acknowledgments	vi
Dedication	vii
1 Introduction	1
1.1 Theory Overview	1
1.2 Analysis Overview	4
2 Theory	5
2.1 The Standard Model	5
2.2 Beyond the Standard Model	7
2.3 Model of Excited Leptons	8
2.3.1 Excited Lepton Decays	11
2.3.2 Pair Production	12
2.3.3 Single Production	15
3 Experimental Environment	18
3.1 The Large Electron Positron Collider	18
3.2 The OPAL Detector	20
3.2.1 The Central Tracking System	22
3.2.2 Calorimeters	27
3.2.3 Muon Chambers	29
3.3 Data Acquisition	29
3.4 OPAL Data and Simulated Event Samples	30

4	Selection of Candidate Events	33
4.1	Preselection	33
4.2	Jet Classification	34
4.2.1	Photon Identification	34
4.2.2	Muon Identification	35
4.2.3	Electron Identification	36
4.2.4	Hadronic Tau Lepton Identification	36
4.3	Event Selection	37
4.3.1	Selection of $ll\gamma\gamma$ Final States	37
4.3.2	Selection of $ll\gamma$ Final States	39
4.3.3	Selection of $e\gamma$ Final State	45
5	Kinematic Fits	49
5.1	Motivation	49
5.2	General Principles	49
5.3	Inputs	51
5.3.1	Photon Candidates	51
5.3.2	Electron Candidates	52
5.3.3	Muon Candidates	52
5.3.4	Tau Candidates	52
5.4	General Constraints	53
5.5	Kinematic Fits for Each Event Final States	54
5.5.1	Kinematic Fits for $ll\gamma\gamma$ Events	54
5.5.2	Kinematic Fits for $ll\gamma$ Events	56
5.5.3	Kinematic Fit for $e\gamma$ Events	58
6	Results	61
6.1	Results	61
6.2	Hypothesis Testing	66
6.2.1	The Likelihood Ratio	66
6.3	Background and Signal Expectations	68
6.3.1	Background Expectation	68
6.3.2	Signal Expectation	69
6.3.3	Systematic Uncertainties	71
6.4	Limit Calculations	74

6.4.1	Treatment of Systematic Uncertainties	76
6.4.2	Limits on Excited Lepton Production Rate	76
6.4.3	Mass Limits	77
6.4.4	Limits on f/Λ	78
6.5	Comparisons with Existing Constraints	79
7	Conclusions	83
A	Tracks and Clusters Requirements	85
B	General Solution to Kinematic Fit	86
C	Error Estimates of Kinematic Fit Input Variables	90
C.1	Electromagnetic Calorimeter Response	91
C.2	Tracking Detectors Response	94
C.3	Taus	102
D	Efficiency, Mass Resolution and Correction Factor Interpolation	106
E	Confidence Level Calculation	114
E.1	The Modified Frequentist Approach	115
F	Excited electron contribution to the $e^+e^- \rightarrow \gamma\gamma$ cross-section	118
	Bibliography	122

List of Tables

1.1	Properties of Standard Model fermions	2
1.2	Properties of Standard Model bosons	3
2.1	Lepton quantum numbers	7
2.2	Excited lepton quantum numbers	9
3.1	Centre-of-mass energy and integrated luminosity of data analysed	31
3.2	Event generators used to simulate the Standard Model processes	32
4.1	Cutflow table for $ll\gamma$ event final states	45
4.2	Cutflow table for the $e\gamma$ event final state	48
6.1	Observed numbers of events in the data and expected numbers of background events for $ll\gamma\gamma$ event final states	62
6.2	Observed numbers of events in the data and expected numbers of background events for $ll\gamma$ and $e\gamma$ event final states	63
6.3	Systematic uncertainties on the signal efficiencies	74
6.4	Systematic uncertainties on the background estimates	75
C.1	Energy and angular resolution parameterisations	96
D.1	Parameterisations of the signal efficiency, mass resolution and efficiency correction factor for different event final states	108

List of Figures

2.1	Feynman diagram of the interaction between two Standard Model charged leptons and a gauge boson	7
2.2	Feynman diagrams of excited charged lepton interactions with Standard Model particles	9
2.3	Electromagnetic branching fraction of excited charged leptons and neutrinos as function of f/f' for different excited lepton masses	13
2.4	Branching fraction of excited charged leptons as function of mass for $f = f'$ and $f = -f'$	13
2.5	Feynman diagrams for the pair production of charged excited leptons . . .	14
2.6	Excited charged lepton pair production cross-section	15
2.7	Feynman diagrams for the single production of excited charged leptons . .	16
2.8	Differential cross-section of singly produced excited charged leptons . . .	16
2.9	Excited charged lepton single production cross-section	17
3.1	Schematic diagram of the accelerator complex at the CERN laboratory . .	21
3.2	Schematic diagram of the OPAL detector	23
3.3	Schematic diagram of the OPAL tracking subdetectors	24
3.4	Cross-sectional diagram of the OPAL silicon microvertex detector	25
3.5	Plot of dE/dx versus track momentum for different types of particles . . .	26
4.1	Schematic diagram of the production of $ll\gamma\gamma$ events	37
4.2	R_{vis} distributions for $ll\gamma\gamma$ events	38
4.3	Event display of typical $ll\gamma\gamma$ events	40
4.4	Schematic diagram of the production of $ll\gamma$ events	41
4.5	R_{vis} distributions for $ll\gamma$ events	42
4.6	Distribution of the quantity $\cos \theta_{e\gamma}$ for $ee\gamma$ events	43
4.7	Distributions of the quantities $E_{\text{total}}^{\text{EM}}/\sqrt{s}$ and $ \cos \theta_{\text{miss}} $ for $\tau\tau\gamma$ events . . .	44

4.8	Schematic diagram of the production of $e\gamma$ events	46
4.9	Distribution of the quantities R_{vis} , $\cos \theta_{e\gamma}$ and $ \cos \theta_\gamma $ for $e\gamma$ events	47
5.1	Example of bias in $l\gamma$ invariant mass of pair produced excited leptons	56
5.2	Probability distributions for $ll\gamma\gamma$ events	57
5.3	Example of bias in the $l\gamma$ invariant mass of singly produced excited leptons	58
5.4	Probability distributions for $ll\gamma$ events	59
5.5	Probability distribution of $e\gamma$ events	60
6.1	Reconstructed $l\gamma$ invariant mass distributions for $ll\gamma\gamma$ events	64
6.2	Reconstructed $l\gamma$ invariant mass distributions for $ll\gamma$ events	65
6.3	Reconstructed $l\gamma$ invariant mass distribution for $e\gamma$ events	66
6.4	Background shape parameterisation for $ll\gamma$ and $ll\gamma\gamma$ event final states	70
6.5	Background shape parameterisation for the $e\gamma$ event final state	71
6.6	Limits on the product of the cross-section at $\sqrt{s} = 208.3$ GeV and the electromagnetic branching fraction	78
6.7	Limits on f/Λ	79
6.8	Feynman diagram of excited electron contribution to the process $e^+e^- \rightarrow \gamma\gamma$	80
6.9	Feynman diagram of excited electron production in ep collisions	81
6.10	Feynman diagram of excited lepton contribution to the anomalous magnetic moment	81
6.11	Summary of constraints on the $e^*e\gamma$ coupling strength	82
C.1	Distributions $(E - E_{\text{beam}})/\sigma_E$ for electron pair events	92
C.2	Distributions of the quantities $(\theta_1 + \theta_2 - \pi)/\sqrt{\sigma_{\theta_1}^2 + \sigma_{\theta_2}^2}$ and $(\phi_1 - \phi_2 - \pi)/\sqrt{\sigma_{\phi_1}^2 + \sigma_{\phi_2}^2}$ for electromagnetic energy clusters using the uncertainties calculated as part of the standard OPAL event reconstruction	93
C.3	Angular resolution parameterisation of electromagnetic energy clusters	95
C.4	Distributions of the quantities $(\theta_1 + \theta_2 - \pi)/\sqrt{\sigma_{\theta_1}^2 + \sigma_{\theta_2}^2}$ and $(\phi_1 - \phi_2 - \pi)/\sqrt{\sigma_{\phi_1}^2 + \sigma_{\phi_2}^2}$ for electromagnetic energy clusters using the new resolution parameterisation	97
C.5	Distributions of the quantity $(p - E_{\text{beam}})/\sigma_p$ for electron and muon pair events	98

C.6	Distributions of the quantities $(\theta_1 + \theta_2 - \pi)/\sqrt{\sigma_{\theta_1}^2 + \sigma_{\theta_2}^2}$ and $(\phi_1 - \phi_2 - \pi)/\sqrt{\sigma_{\phi_1}^2 + \sigma_{\phi_2}^2}$ for tracks using uncertainties obtained by the OPAL track reconstruction algorithm	100
C.7	Track polar angle resolution parameterisation	101
C.8	Track azimuthal angle resolution parameterisation	102
C.9	Distributions of the quantities $(\theta_1 + \theta_2 - \pi)/\sqrt{\sigma_{\theta_1}^2 + \sigma_{\theta_2}^2}$ and $(\phi_1 - \phi_2 - \pi)/\sqrt{\sigma_{\phi_1}^2 + \sigma_{\phi_2}^2}$ for tracks using the new angular resolution parameterisation	103
C.10	Tau angular resolution parameterisation	104
C.11	Distributions of the quantities $(\theta_1 + \theta_2 - \pi)/\sqrt{\sigma_{\theta_1}^2 + \sigma_{\theta_2}^2}$ and $(\phi_1 - \phi_2 - \pi)/\sqrt{\sigma_{\phi_1}^2 + \sigma_{\phi_2}^2}$ for tau pair events using uncertainties from the angular resolution parameterisation	105
D.1	Efficiency parameterisations for the $ll\gamma$ and $ll\gamma\gamma$ selections	107
D.2	Efficiency parameterisation for the $e\gamma$ selection	109
D.3	Resolution parameterisations for $ll\gamma$ and $ll\gamma\gamma$ events	110
D.4	Resolution parameterisation for $e\gamma$ events	111
D.5	Parameterisations of the efficiency correction factors for $ll\gamma$ and $ll\gamma\gamma$ events	112
D.6	Parameterisation of the efficiency correction factor for $e\gamma$ events	113
E.1	Example of likelihood ratio probability density distributions	117
F.1	Feynman diagrams of the Standard Model and excited electron contributions to the process $e^+e^- \rightarrow \gamma\gamma$	119

Acknowledgements

The road that led to this thesis was an adventure, a great adventure.

I have met extraordinary people.

I have been to places I never imagined I would see.

I have done things that sometimes I felt were not possible.

First and foremost, I want to thank my supervisors Rob McPherson and Randy Sobie. Without them, none of this would have been possible. They are both excellent supervisors and brilliant physicists. I could burst into their office at any time, and they would always make me feel welcome and take the time to answer my questions. They complemented each other perfectly in their interest and approach to physics. Their unconditional support and patience has helped me over the years build confidence in my own abilities and look forward to a fruitful career in physics. I am deeply indebted to them.

I also want to acknowledge the support of Richard Keeler, both as a supervisor for the first couple of years of my graduate studies and as the head of the particle physics group at Victoria. Richard, among other people, made it possible for me to attend many conferences and spend an extended time at CERN, all of which allowed me to meet and collaborate with a large number of scientists from around the world.

It has been a real pleasure to be part of the particle physics group at Victoria. I would like to thank all the faculty members, research assistants and students with whom I have had many stimulating discussions. Activities such as the ritual lunch time hour, Friday afternoon beer and participation in team sports all contributed in fostering a pleasant and fun work environment. Special thanks go to Alan Astbury for his continuous support and invaluable advice.

I also want to extend my gratitude to the many OPALists and friends that have made my stay at CERN a unique and unforgettable experience. Special thanks go to Gordon Long, Carla Sbarra, Rob McPherson, Ian Bailey and Laura Kormos for their invaluable help in running/maintaining the OPAL event reconstruction system.

Finally, Matt, thank you.

*À mes parents, Gilles et Paulette, et à mon frère, Hugo,
merci pour tout...*

Introduction

This thesis presents a search for evidence that the fundamental particles¹ of nature are themselves composed of subconstituents of a new type of matter yet undiscovered. The observation of excited states of fundamental particles would be an unambiguous indication of their composite nature. Much like a hydrogen atom, the subconstituents would generate a series of excitations, each of which would decay to the ground state, the known particles, via the emission of radiation. A search for evidence of these excited states is performed by looking for the simultaneous presence of emitted radiation and ground state particles in electron-positron collisions.

The remainder of this chapter summarises our current understanding of the subatomic world followed by a brief description of the work presented in this thesis. Chapter 2 introduces the relevant aspects of the Standard Model of particle physics as well as details of the theoretical framework used to interpret results of the analysis performed. The experimental apparatus is presented in Chapter 3. Chapters 4 and 5 describe the selection criteria that were developed to identify the experimental signatures relevant for this work and the kinematic fit technique used to improve the sensitivity of the search. Results are presented in Chapter 6. Chapter 7 summarises the work described in this thesis and presents a brief outlook on the future of the subject.

1.1 Theory Overview

In order to determine if the current known set of fundamental particles are themselves composite, it is important to understand their basic properties. The most familiar form of matter is composed of two leptons, the electron (e) and electron neutrino (ν_e), and two

¹Fundamental particles are considered to be point-like and indivisible.

Fermions (spin=1/2)

	Leptons			Quarks		
	flavour	Q	mass (GeV)	flavour	Q	mass (GeV)
1 st generation	ν_e	0	$< 3 \times 10^{-9}$	u	$+\frac{2}{3}$	$\sim 3 \times 10^{-3}$
	e	-1	5.11×10^{-4}	d	$-\frac{1}{3}$	$\sim 7 \times 10^{-3}$
2 nd generation	ν_μ	0	$< 1.9 \times 10^{-4}$	c	$+\frac{2}{3}$	~ 1.2
	μ	-1	0.106	s	$-\frac{1}{3}$	~ 0.1
3 rd generation	ν_τ	0	$< 18.2 \times 10^{-3}$	t	$+\frac{2}{3}$	174
	τ	-1	1.777	b	$-\frac{1}{3}$	~ 4.2

Table 1.1: Properties of Standard Model leptons and quarks arranged in three generations. The electric charge (Q) is expressed in units of the positron (e^+) charge. For each particle in the table there exists a corresponding antiparticle.

types of quarks, the up (u) and the down (d) quarks². These spin 1/2 particles, called fermions, make up the first generation of matter. More exotic types of particles, observed in cosmic rays or produced in high energy collisions, form the second and third generation. Table 1.1 shows some of the properties of the three generations of leptons and quarks. Particles of different generations have identical properties except for their masses which increases from one generation to the other. This three-fold replica of nature and mass hierarchy are fundamental aspects of the Standard Model which are not currently understood. In addition to the leptons and quarks presented in Table 1.1, there exists for every particle a corresponding antiparticle with the same mass³. For example, the antiparticle of an electron (e^-) is called a positron (e^+).

Particles interact with each other via the electromagnetic, weak and strong forces. Although a fourth force exists in nature, the force of gravity, its relative strength between two subatomic particles is more than 30 orders of magnitude smaller than the relative strength of the other three forces and its effect can therefore be safely neglected. The electro-

²Atomic nuclei are made up of protons and neutrons which are themselves made up of quarks. Protons are bound states of two up and one down quarks while neutrons are composed of two down and one up quarks.

³Antiparticles are usually identified with a horizontal line over the corresponding particle's symbol. The electron antineutrino, for example, is written as $\bar{\nu}_e$.

Bosons (spin = 1)

	electric charge	mass (GeV)	force
γ	0	0	Electromagnetic
W^\pm	± 1	80.4	Weak
Z^0	0	91.2	
g (8 gluons)	0	0	Strong

Table 1.2: Properties of Standard Model bosons and the force they mediate.

magnetic force is responsible for the Coulomb attraction of oppositely charged particles. Nuclear beta decay, on the other hand, is a phenomena accounted for by the existence of the weak force. Finally, the strong force tightly binds together quarks to form particles called hadrons. Leptons, such as the electron and electron neutrino, are particles that only interact through the weak and electromagnetic forces. Each force is mediated by integer spin particles called bosons. For example, the messenger of the electromagnetic force is the photon, represented by the Greek letter γ . The repulsive electromagnetic force between two negatively charged electrons results from the exchange of photons. Table 1.2 summarizes some properties of the known bosons and the force they mediate. Leptons and bosons are considered to be fundamental building blocks of nature.

The Standard Model embodies our knowledge of how the fundamental building blocks of our universe interact with each other. It forms a coherent and predictive framework that has been tested to unprecedented precision. Yet, many aspects of the Standard Model remain unexplained. The observed mass spectrum of leptons and the well-ordered pattern of generations, for example, were historically introduced in the Standard Model based on experimental observations. Additional shortcomings include the lack of a unified theoretical framework that could describe all four forces.

Many different extensions of the Standard Model have been proposed over the years in an attempt to address some of these issues. One such idea is based on the assumption that leptons and quarks, thought to be fundamental buildings blocks of nature, could instead be made of even smaller subconstituents. The substructure of these particles would be visible only when probed at very small distance scales or alternatively, at very high energy⁴. One

⁴To experimentally resolve small structures requires a small wavelength. In quantum mechanics, the

natural consequence of lepton and quark compositeness would be the existence of excited states of leptons and quarks.

1.2 Analysis Overview

The work presented in this thesis consists of a search for experimental signatures compatible with the production and subsequent decay, via the emission of a photon, of excited charged leptons (ℓ^*) in electron-positron collisions.

Excited charged leptons could be created in pairs ($e^+e^- \rightarrow \ell^*\ell^*$) or singly in association with a Standard Model lepton ($e^+e^- \rightarrow \ell^*\ell$)⁵. Such states would promptly decay to a photon and a Standard Model lepton and thus cannot be directly observed. The invariant mass⁶ of the detected photon and Standard Model lepton should be equal to the mass of the excited state. For excited states produced in a pair, the invariant mass of both photon and lepton pairs should be equal.

A set of criteria was developed to select experimental signatures consistent with the production of excited charged leptons. The sensitivity of the search is substantially enhanced by the use of a kinematic fit technique which improves the estimates of the energy and direction of the particles detected. This information is used to precisely calculate the invariant mass of each possible pair of lepton and photon observed.

The invariant mass of the excited lepton candidates is compared with predictions from the Standard Model. No evidence indicating the existence of excited leptons is found. The results of the analysis are used to calculate constraints on parameters describing the properties of excited states in theoretical extension of the Standard Model. The limits presented in this thesis are currently the most stringent constraints on the existence of excited leptons.

wavelength associated with a particle is inversely proportional to its momentum. Thus the higher the energy of particles, the smaller scale that can be probed.

⁵To keep the notation simple throughout the thesis, the electric charge of leptons is often not explicitly written. Charge conjugation is assumed. Thus, the notation $e^+e^- \rightarrow \ell^*\ell$ implies both reactions $e^+e^- \rightarrow \ell^{*+}\ell^-$ and $e^+e^- \rightarrow \ell^{*-}\ell^+$.

⁶The invariant mass of two particles is defined as $m_{12} = \sqrt{(E_1 + E_2)^2 - (\mathbf{p}_1 + \mathbf{p}_2)^2}$, where E_1, E_2 and $\mathbf{p}_1, \mathbf{p}_2$ are the energy and momentum vector of the two particles.

Theory

The first section of this chapter introduces particular aspects of the Standard Model most relevant for the work presented in this thesis. This is then followed by general remarks about some of the outstanding problems and shortcomings of the Standard Model. The last section is devoted to the particular theoretical framework describing the properties and interactions of excited states of leptons and quarks.

2.1 The Standard Model

The Standard Model is based on two quantum field theories: the electroweak model of Glashow, Weinberg and Salam [1] which describes in a common framework both the electromagnetic and weak forces, and the theory of quantum chromodynamics (QCD) which offers a description of the strong force exclusively experienced by quarks. Interactions between particles are a natural consequence of the invariance of the quantum field theories under a class of local symmetry transformations associated with the $SU(3)_c \times SU(2)_L \times U(1)_Y$ gauge group. The invariance of a theory under local gauge transformations is a crucial property that ensures the renormalisability of a theory [2], i.e. the fact that physical observables such as the lifetime and production rate of particles are finite quantities calculable to all energies and all orders in coupling constants. The quantum mechanical description of particles is made invariant under some set of symmetry transformations by introducing integer spin fields (gauge bosons) which couple to the particles. The local $SU(3)_c$ symmetry transformation generates the strong interaction between quarks which couples to the colour charge (c) of particles. Similarly, the electroweak force is a result of the invariance of the theory under local $SU(2)_L \times U(1)_Y$ transformations where the subscript L indicates that only left-handed fermions transform non-trivially under the $SU(2)$ group symmetry. The electroweak force is proportional to the weak isospin (T) and

weak hypercharge (Y) of particles defined such that $Q = T_3 + Y/2$ where Q is the electric charge and T_3 , the third component of weak isospin.

Fermion fields exist in two different chiralities, left and right-handed components. Left-handed fields form weak isospin doublets while right-handed one only exist in weak isospin singlets. For leptons of the first generation, the eigenstates of the electroweak theory can be written as

$$L_L = \begin{pmatrix} \nu_e \\ e \end{pmatrix}_L, \quad L_R = e_R \quad (2.1)$$

where e and ν_e represent the electron and electron neutrino fields and the subscripts refer to the eigenstates chirality. Table 2.1 summarises the quantum numbers of leptons of the first generation which dictate their transformation properties under the $SU(2)_L \times U(1)_Y$ symmetry.

By analogy to the formalism used in classical mechanics, the dynamics of particle fields and their interactions are usually expressed, in quantum field theories, in terms of a function called the Lagrangian density (\mathcal{L}). As an example, the Lagrangian density describing the interaction between two leptons and a gauge boson ($V = \gamma, Z^0, W^\pm$) can be written as

$$\mathcal{L}_{LLV} = \bar{L}_L \gamma^\mu \left[g \frac{\boldsymbol{\tau}}{2} \mathbf{W}_\mu + g' \frac{Y}{2} B_\mu \right] L_L + \bar{L}_R \gamma^\mu \left[g' \frac{Y}{2} B_\mu \right] L_R \quad (2.2)$$

where $\boldsymbol{\tau}$ denotes the Pauli matrices¹, Y is the weak hypercharge, $\mathbf{W}_\mu = (W_\mu^1, W_\mu^2, W_\mu^3)$ and B_μ are the gauge fields associated with the $SU(2)_L$ and $U(1)_Y$ symmetry. These are related to the physical gauge boson fields observed in nature by the transformation

$$W_\mu^\pm = \frac{1}{\sqrt{2}} (W_\mu^1 \mp i W_\mu^2) \quad (2.3)$$

$$Z_\mu = -B_\mu \sin \theta_W + W_\mu^3 \cos \theta_W \quad (2.4)$$

$$A_\mu = B_\mu \cos \theta_W + W_\mu^3 \sin \theta_W \quad (2.5)$$

where $\sin \theta_W$ is called the weak mixing angle and is a free parameter of the Standard Model which needs to be experimentally measured. The parameters g and g' are the $SU(2)_L$ and $U(1)_Y$ coupling constants. The interaction between two charged leptons and a gauge boson can be equivalently described by the Feynman diagram shown in Figure 2.1 where the

¹In group theory, the Pauli matrices are said to be the generators of the $SU(2)$ group. They consist of three linearly independent 2×2 matrices which satisfy the commutation relations $[\tau_i, \tau_j] = 2i \epsilon_{ijk} \tau_k$ where ϵ_{ijk} represent the totally antisymmetric structure constants of the group.

Lepton	T	T_3	Y	Q
ν_{eL}	$\frac{1}{2}$	$\frac{1}{2}$	-1	0
e_L	$\frac{1}{2}$	$-\frac{1}{2}$	-1	-1
e_R	0	0	-2	-1

Table 2.1: Quantum numbers of leptons of the first generation where T , T_3 , Y and Q are the weak isospin, third component of the isospin, the weak hypercharge and electric charge, respectively.

arrows represent the flow of the electroweak current.

Fermions and bosons in the Standard Model are given masses by introducing a scalar Higgs field [3] which spontaneously breaks the electroweak $SU(2)_L \times U(1)_Y$ symmetry of the theory. This mechanism is needed as mass terms cannot be directly added ‘by hand’ to the Lagrangian without spoiling gauge invariance. Instead, the coupling of the Higgs field to the weak gauge bosons and fermions is found to generate the appropriate mass terms without destroying the gauge symmetry of the theory. The symmetry of the Lagrangian is simply hidden by the choice of a specific ground state or vacuum expectation value.

2.2 Beyond the Standard Model

The Standard Model has been extremely successful at describing the interactions between particles observed in nature. It has so far been tested to an impressive one part in 10^6 . Despite all its achievements, the Standard Model however remains somewhat of an *ad hoc* theory which relies on the experimental measurements of many fundamental quantities such as the masses of particles and their couplings. It also fails to explain the three-fold pattern of fermion generations and the observed mass spectrum. Other shortcomings of the Standard Model include the inability to explain the existence of left-handed doublets and right-handed singlets as well as the lack of unification between all forces including gravity.

A number of models attempt to address some of the mysterious aspects of the Standard Model, albeit with varying degree of success. One approach postulates that particles

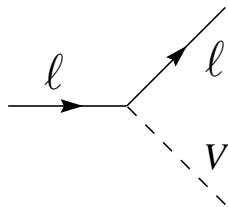


Figure 2.1: Feynman diagram of the interaction between two Standard Model charged leptons ($l = e, \mu, \tau$) and a gauge boson ($V = \gamma, Z^0$).

currently considered to be fundamental might instead be composed of smaller subconstituents. Historically, in our understanding of nature from atoms to quarks, systems that were originally thought to be fundamental building blocks of the universe have revealed substructure when probed at increasingly larger energy scales. Fermions that are thought to be point-like particles in the Standard Model could then appear to be made of smaller constituents when studied at high energy. This unique approach to physics beyond the Standard Model could explain in a natural way the pattern of fermion generations as well as the observed mass spectrum.

2.3 Model of Excited Leptons

There have been various attempts at building a complete model of composite fermions [4]. It has however proved to be quite challenging to develop a model consistent with current experimental observations and precision measurements. Despite the lack of a complete model, searches for possible experimental consequences of fermion compositeness have been and continue to be pursued. These searches are carried out in the framework of a low energy approximation of what the complete and yet unknown theory might predict.

Experimental consequences of fermion compositeness could include the existence of excited states of the Standard Model fermions. Much like the arrangement of subconstituents in a hydrogen atom or a hadron results in bound states with properties different than the ground states of the system, excited fermions are expected to exhibit unique characteristics distinguishing them from the known Standard Model fermions.

The theoretical framework used in this thesis to calculate constraints on the existence of excited electrons (e^*), muons (μ^*) and taus (τ^*) is a phenomenological model [5, 6]. This model describes the possible interactions between excited leptons and Standard Model particles without explicitly describing the nature and dynamics of the fermion subconstituents. Although this phenomenological model is described here only in terms of the leptonic sector relevant for the present work, it is straight forward to extend the formalism to include excited states of quarks.

Excited states of Standard Model fermions are assumed here to have both spin and weak isospin 1/2, although other spin assignments have also been considered in the literature [7]. To accommodate the fact that the unobserved excited states must be much heavier than the Standard Model fermions, they are assumed to acquire their mass prior to the spontaneous symmetry breaking of the Standard Model Lagrangian. Details of how the

excited lepton	T	T_3	Y	Q
ν_{eL}^*	$\frac{1}{2}$	$\frac{1}{2}$	-1	0
ν_{eR}^*	$\frac{1}{2}$	$\frac{1}{2}$	-1	0
e_L^*	$\frac{1}{2}$	$-\frac{1}{2}$	-1	-1
e_R^*	$\frac{1}{2}$	$-\frac{1}{2}$	-1	-1

Table 2.2: Quantum numbers of excited leptons of the first generation where T , T_3 , Y and Q are the weak isospin, third component of the isospin, the weak hypercharge and electric charge, respectively.

masses of these excited states arise is not relevant for the low energy phenomenology in the present theoretical framework. They should however be part of any model attempting to describe the full dynamics of fermion constituents. In order to retain the fundamental $SU(2)_L \times U(1)_Y$ gauge invariance of the Standard Model in the presence of additional mass terms, excited states must exist in both left-handed (L) and right-handed (R) weak isodoublets, unlike Standard Model fermions. For excited leptons of the first generation, the two weak isodoublets can be written as

$$L_L^* = \begin{pmatrix} \nu_e^* \\ e^* \end{pmatrix}_L, \quad L_R^* = \begin{pmatrix} \nu_e^* \\ e^* \end{pmatrix}_R \quad (2.6)$$

where e^* and ν_e^* represent the excited electron and excited electron neutrino fields respectively.

Given the assumptions presented above, the quantum numbers of excited leptons are fixed to the values given in Table 2.2. Furthermore, in order to be able to calculate experimental observables such as the production rate and decay of these excited states, the two interaction vertices shown in Figure 2.2 must also be introduced.

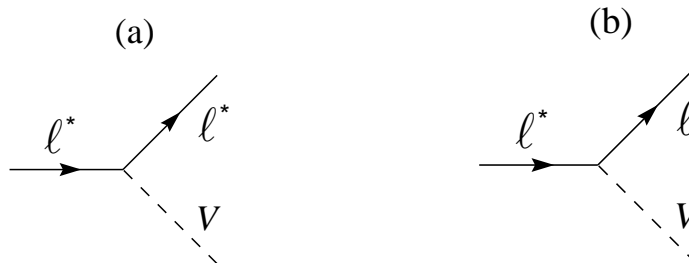


Figure 2.2: Diagrams showing the interactions of charged excited leptons ($\ell^* = e^*, \mu^*, \tau^*$) with Standard Model leptons ($\ell = e, \mu, \tau$) and gauge bosons ($V = \gamma, Z^0$).

The interaction between two excited leptons and one gauge boson (L^*L^*V) is assumed to have the same form and coupling strength as the corresponding Standard Model interaction between two leptons and one boson. In addition, only excited leptons from the same generation can interact with each other. Following closely Equation 2.2, the Lagrangian density describing the L^*L^*V coupling is usually written as

$$\mathcal{L}_{L^*L^*V} = \bar{L}_L^* \gamma^\mu \left[g \frac{\boldsymbol{\tau}}{2} \mathbf{W}_\mu + g' \frac{Y}{2} B_\mu \right] L_L^* + \bar{L}_R^* \gamma^\mu \left[g \frac{\boldsymbol{\tau}}{2} \mathbf{W}_\mu + g' \frac{Y}{2} B_\mu \right] L_R^* \quad (2.7)$$

Given the composite nature of leptons in the present model, the interaction described above should contain form factors to take into account deviations from a point-like interaction due to the presence of subconstituents. However, for large value of the compositeness scale, the effects of these form factors are negligible.

The particular choice of the interaction Lagrangian density describing the transition between an excited lepton, a lepton and a gauge boson (L^*LV) dictates not only the decays of excited states but also, as will be discussed later, their single production in e^+e^- collisions. The requirement that the interaction be $SU(2)_L \times U(1)_Y$ gauge invariant uniquely determines the coupling between a spin 1/2 excited lepton, a Standard Model lepton and gauge boson to be of a tensorial nature [7]. A simple vectorial interaction similar to Equations 2.2 and 2.7 would not be gauge invariant under $SU(2)_L$ symmetry as the right-handed component of excited leptons forms a weak isodoublet which transforms differently from the usual Standard Model right-handed weak singlet. Furthermore, in light of existing constraints on the existence of excited leptons, described in details in Section 6.5, only left-handed leptons are allowed to couple to excited states. A coupling without this chiral symmetry would lead to large contributions to the anomalous magnetic moment of leptons, in conflict with current precision measurements of this quantity. For these reasons, the interaction between an excited lepton, a Standard Model lepton and a gauge boson is usually described by the following chiral conserving $SU(2)_L \times U(1)_Y$ gauge invariant Lagrangian density [5–7]

$$\begin{aligned} \mathcal{L}_{L^*LV} = & \frac{1}{2\Lambda} \bar{L}_R^* \sigma^{\mu\nu} \left[g f \frac{\boldsymbol{\tau}}{2} \mathbf{W}_{\mu\nu} + g' f' \frac{Y}{2} B_{\mu\nu} \right] L_L + \\ & \frac{1}{2\Lambda} \bar{L}_L \sigma^{\mu\nu} \left[g f \frac{\boldsymbol{\tau}}{2} \mathbf{W}_{\mu\nu} + g' f' \frac{Y}{2} B_{\mu\nu} \right] L_R^* \end{aligned} \quad (2.8)$$

where $\sigma^{\mu\nu}$ is the covariant bilinear tensor², $\mathbf{W}_{\mu\nu}$ and $B_{\mu\nu}$ represent the Standard Model

² $\sigma^{\mu\nu} = \gamma^\mu \gamma^\nu - \gamma^\nu \gamma^\mu$ where γ^μ and γ^ν represent Dirac matrices.

gauge field tensors³ and the couplings g, g' are the $SU(2)_L$ and $U(1)_Y$ coupling constants of the Standard Model introduced in Section 2.1. The compositeness scale is set by the parameter Λ which has units of energy. Finally, the strength of the L^*LV couplings is governed by the constants f and f' . These constants can be interpreted as weight factors associated with the different gauge groups.

The only unknown parameters of the phenomenological model presented in this section are the mass of excited leptons, the compositeness scale Λ and the strength of the couplings f and f' . To reduce the number of free parameters it is customary to assume either a relation between f and f' or set one coupling to zero. For easy comparison with previously published results, limits calculated in this paper correspond to the coupling choice $f = f'$. As will be shown in the next section, this assignment is a natural choice which forbids excited neutrinos from decaying electromagnetically.

Physical observables such as the production and decay rates of excited leptons are calculated from the Lagrangians 2.8 and 2.7. Approximate expressions for these observables are presented below as an indication of the expected physical properties of excited leptons. In the analysis presented in this thesis, efficiencies and expected distributions of kinematical variables for excited leptons are instead obtained using the Monte Carlo event generator EXOTIC based on the exact expressions for the production and decay rates.

2.3.1 Excited Lepton Decays

The decay of an excited charged lepton into a Standard Model lepton and a gauge boson is shown schematically in Figure 2.2(b) and is determined by the Lagrangian density given in Equation 2.8.

Neglecting the decay width of the gauge bosons ($\Gamma_V \rightarrow 0$), the decay rate⁴ into the different gauge bosons can be approximated, for excited lepton masses larger than M_V , by the following formula

$$\Gamma = \frac{\alpha}{4} \frac{m_*^3}{\Lambda^2} f_V^2 \left(1 - \frac{M_V^2}{m_*^2}\right)^2 \left(1 + \frac{M_V^2}{2m_*^2}\right) \quad (2.9)$$

where m_* and M_V are the excited lepton and gauge boson masses respectively and the quantities f_V are defined in terms of the parameters f and f' , the excited states electric

³ $\mathbf{W}_{\mu\nu} = \partial_\mu \mathbf{W}_\nu - \partial_\nu \mathbf{W}_\mu$

⁴The branching fraction of a particle into a specific final state is defined as the ratio of the final state decay rate to the total decay rate of all possible final states.

charge (Q) and third component of the weak isospin for left-handed states (T_{3L})

$$f_\gamma = Qf' + T_{3L}(f - f') \quad (2.10)$$

$$f_W = \frac{1}{\sqrt{2} \sin \theta_W} f \quad (2.11)$$

$$f_Z = \frac{4 T_{3L} (\cos^2 \theta_W f + \sin^2 \theta_W f') - 4 Q \sin^2 \theta_W f'}{4 \sin \theta_W \cos \theta_W} . \quad (2.12)$$

The branching fractions of excited neutrinos (ν^*) are identical to that of excited charged leptons (ℓ^*) under the transformation $f' \rightarrow -f'$. This symmetry is a direct consequence of the weak isospin assignment of excited leptons. Figure 2.3 shows the predicted electromagnetic branching fraction of excited charged leptons and excited neutrinos for different values of f and f' . As seen from Equation 2.10, the branching fraction for excited charged leptons decaying into a lepton and photon vanishes for the special case $f = -f'$. Alternatively, the electromagnetic branching fraction of excited neutrinos is zero under the assumption that $f = f'$.

Figure 2.4 shows a comparison of the branching fraction of excited charged leptons into each possible gauge boson as function of mass for two specific coupling assignments, $f = f'$ and $f = -f'$. These branching fractions were calculated from the complete formula found in [5], without relying on the assumptions that led to the approximate decay rate given in Equation 2.9. For excited charged lepton masses below the W^\pm and Z^0 masses, the electromagnetic branching fraction is 100% regardless of the values of the couplings f and f' , except for $f = -f'$ which entirely forbids this particular decay. Given that the electromagnetic branching fraction of excited charged leptons is non-negligible for most values of f , f' and the clean characteristic experimental signatures expected, the photon decay constitutes one of the most sensitive channels for the search for excited leptons

2.3.2 Pair Production

Charged excited leptons could be produced in e^+e^- collision in pairs for masses up to approximately half the centre-of-mass energy. The pair production would proceed through the exchange of a photon or a Z^0 boson as presented in Figure 2.5(a). Excited electrons could also be produced via the t -channel diagram shown in Figure 2.5(b). This production mechanism, however, depends directly on two interactions between an excited electron, an electron and a gauge boson. Given the existing constraints on the strength of this coupling

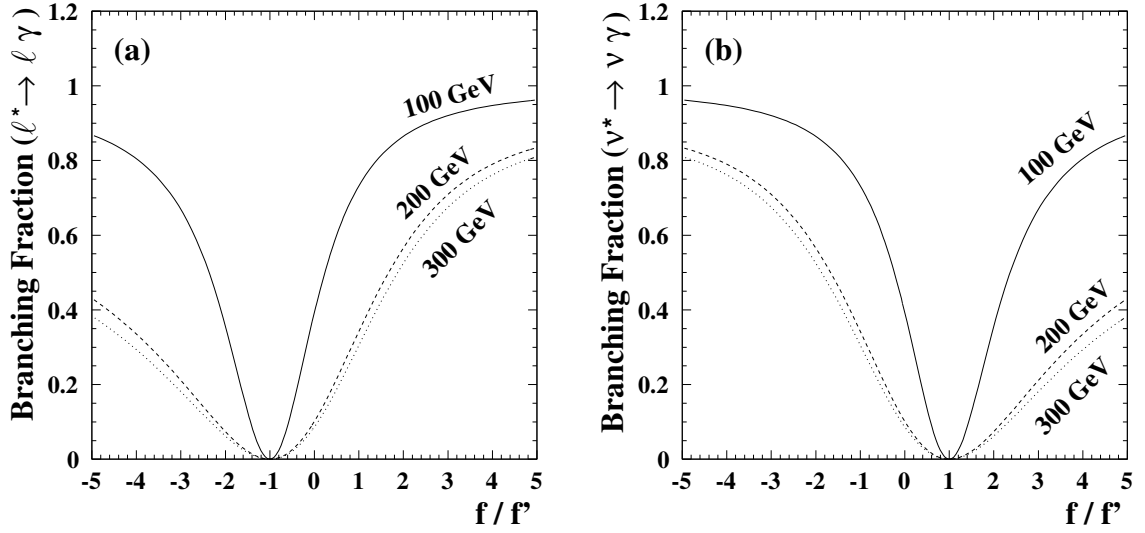


Figure 2.3: Electromagnetic branching fraction of (a) excited charged leptons and (b) excited neutrinos for different values of f , f' and for excited lepton masses of 100, 200 and 300 GeV.

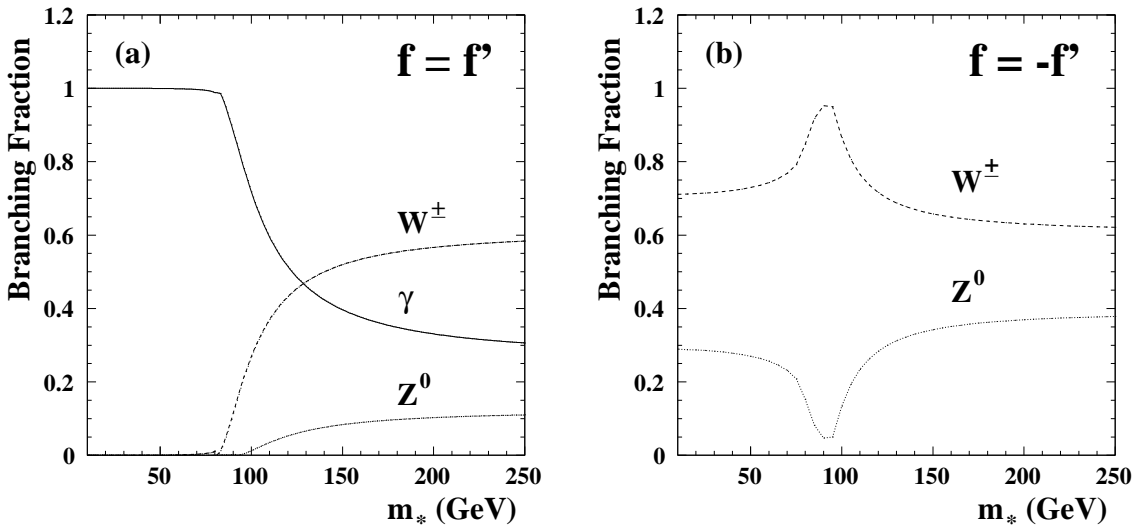


Figure 2.4: Branching fraction of excited charged leptons as a function of mass for (a) $f = f'$ and (b) $f = -f'$. These figures equivalently represent the branching fraction for excited neutrinos upon the substitution $f' \rightarrow -f'$.

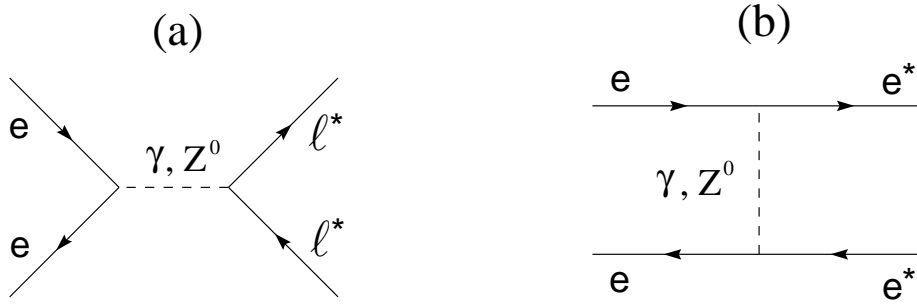


Figure 2.5: Pair production of excited charged leptons via a (a) s -channel and (b) t -channel diagrams.

discussed in Section 6.5, the contribution of the t -channel diagram (Figure 2.5(b)) for the pair production of excited electrons is much smaller than that of the s -channel diagram and can be safely neglected.

The interaction described in Equation 2.7 therefore completely determines the pair production rate, or cross-section, of excited leptons. Neglecting the decay width of the heavy gauge bosons ($\Gamma_V \rightarrow 0$), the pair production cross-section can be approximated as

$$\sigma = \frac{2\pi\alpha^2}{3s} \beta (3 - \beta^2) \left[1 + \frac{2 v_e v_{\ell^*}}{1 - M_Z^2/s} + \frac{(a_e^2 + v_e^2) v_{\ell^*}^2}{(1 - M_Z^2/s)^2} \right] \quad (2.13)$$

where α is the fine structure constant, M_Z is the mass of the Z^0 boson, \sqrt{s} is the collision centre-of-mass energy and $\beta = \sqrt{1 - 4m_*^2/s}$. The constants v_e , v_{ℓ^*} and a_e are defined in terms of the electric charge and weak isospin as

$$v_{e,\ell^*} = \frac{2 T_{3L}^{e,\ell^*} + 2 T_{3R}^{e,\ell^*} - 4 Q \sin^2 \theta_W}{4 \sin \theta_W \cos \theta_W} \quad (2.14)$$

$$a_e = \frac{2 T_{3L}^e - 2 T_{3R}^e}{4 \sin \theta_W \cos \theta_W} . \quad (2.15)$$

The pair production cross-section at a given centre-of-mass energy only depends on the mass of the excited leptons. An example of the expected total cross-section for the pair production of excited charged leptons as function of mass is presented in Figure 2.6.

The pair production of excited charged leptons followed by a prompt electromagnetic decay of each excited state would result in event final states, observed in the detector, containing exactly two leptons of the same flavour and two isolated photon ($\ell\ell\gamma\gamma$). The

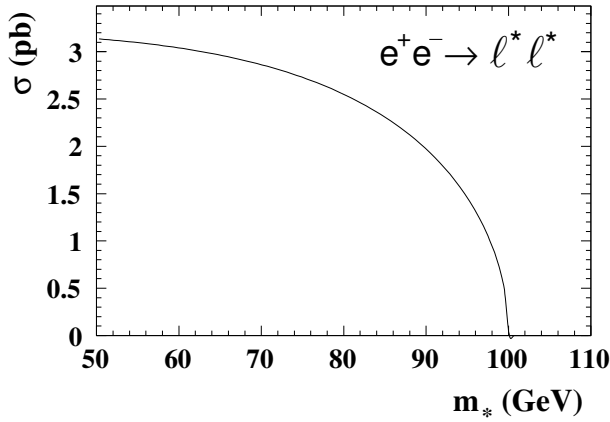


Figure 2.6: Total cross-section (σ) for the pair production of excited charged leptons as a function of mass (m_*) in e^+e^- collisions at a centre-of-mass energy of 200 GeV.

search for pair produced excited charged leptons thus consists in identifying events of the type $ee\gamma\gamma$, $\mu\mu\gamma\gamma$ and $\tau\tau\gamma\gamma$.

2.3.3 Single Production

Excited charged leptons could also be produced in association with a Standard Model lepton. In contrast with the pair production discussed in the previous section, excited states with masses up to the centre-of-mass energy could be singly produced. The single production of excited charged leptons would proceed via the exchange of a photon or a Z^0 boson coupling directly to an excited state and a lepton as described by the Lagrangian density of Equation 2.8 and shown schematically in Figure 2.7(a). In addition, excited electrons could be produced via the t -channel diagram shown in Figure 2.7(b). Unlike the pair production of excited electrons for which the contribution from this t -channel diagram is relatively small, both diagrams shown in Figure 2.7 depend on the strength of the L^*LV coupling and thus contribute to the single production of excited electrons. The interaction Lagrangian of Equation 2.8 dictates the single production rate of excited charged leptons. Given the coupling assignment $f = f'$, the single production rate only depends on the unknown quantity f/Λ and the mass of the excited state.

The complete equation describing the differential cross-section of singly produced excited leptons will not be presented here as it is non-trivial and not particularly enlightening. It can however be found in [5] and [6]. Figure 2.8 shows the single production differential cross-section expected for different excited charged lepton flavours. As a consequence of the existence of the t -channel diagram (Figure 2.7(b)), excited electrons are expected to be singly produced predominantly in the forward direction unlike excited muons and taus.

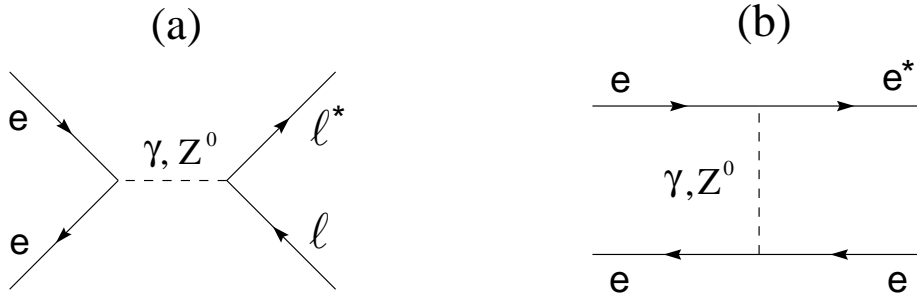


Figure 2.7: Diagrams contributing to the single production of excited charged leptons; (a) s -channel and (b) t -channel diagrams.

The total cross-section for the single production of excited muons or taus is given by

$$\sigma = \frac{\pi\alpha^2\beta^2}{\Lambda^2} \left(1 - \frac{\beta}{3}\right) \left[f_\gamma^2 - \frac{2v_e f_\gamma f_Z}{1 - M_Z^2/s} + \frac{(a_e^2 + v_e^2) f_Z^2}{(1 - M_Z^2/s)^2} \right] \quad (2.16)$$

where the quantities f_γ , f_Z and v_e , a_e have been previously defined in Equations 2.10, 2.12, 2.15 and 2.14, respectively, and $\beta = 1 - m_*^2/s$. The total cross-section for singly produced excited electron is more complicated due to the additional contribution of Diagram 2.7(b). For centre-of-mass energy greater than the Z^0 mass and keeping only the dependence on the electron mass (m_e) in the leading terms, the total cross-section can be approximated to

$$\sigma = \pi\alpha^2\beta \frac{f_\gamma^2}{\Lambda^2} \left[\left(1 - \frac{2}{3}\beta\right) \beta - \beta - 3 + \frac{1 + \beta^2}{\beta} \log \left(\frac{s}{m_e^2} \frac{\beta^2}{(1 - \beta)^2} \right) \right] . \quad (2.17)$$

Figure 2.9 shows the total cross-section of singly produced excited charged leptons as

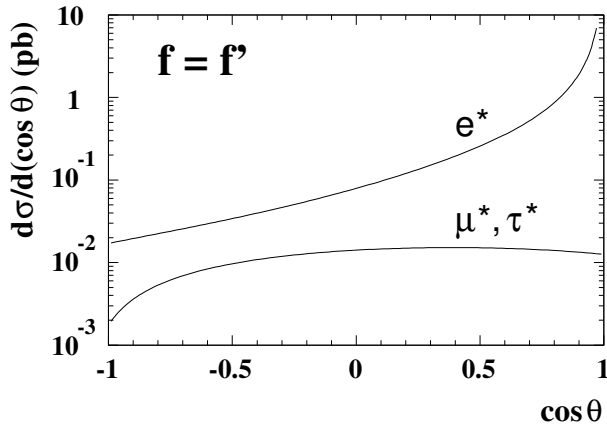


Figure 2.8: Differential cross-section of singly produced excited charged leptons with a mass of 150 GeV at a centre-of-mass energy of 200 GeV and assuming $f/\Lambda = f'/\Lambda = 1 \text{ TeV}^{-1}$.

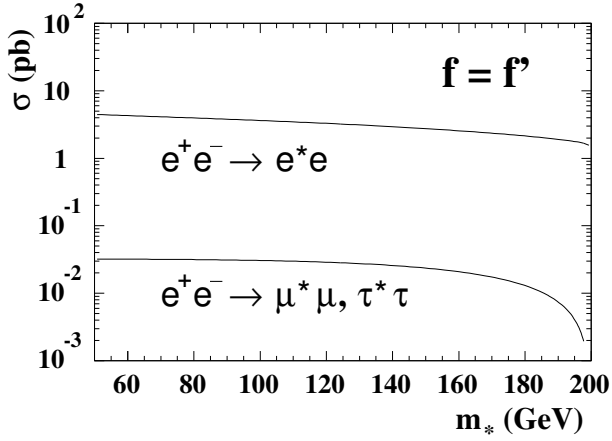


Figure 2.9: Total cross-section (σ) for the single production of excited charged leptons as a function of mass (m_*) in e^+e^- collisions at a centre-of-mass energy of 200 GeV and assuming $f/\Lambda = f'/\Lambda = 1 \text{ TeV}^{-1}$.

function of mass.

As can be seen from Equations 2.16 and 2.17, for $f = f'$, the total cross-section of singly produced excited leptons is directly proportional to $(f/\Lambda)^2$. Given existing constraints on the coupling parameters f/Λ , the production rate of singly produced excited charged leptons is expected to be orders of magnitude smaller than that of pair production. However, the single production search extends the kinematic reach of an experiment to masses up to the centre-of-mass energy.

The prompt decay of excited charged leptons singly produced would lead to event final states containing two leptons of the same flavour and one energetic photon ($ll\gamma$). Since excited electrons are expected to be predominantly produced in the forward region of the detector, the electron produced in association with the excited state may be outside the detector acceptance resulting in event final states containing only one electron and one photon ($e\gamma$). The search for singly produced excited charged leptons which promptly decay electromagnetically therefore consists in identifying events of the types $ee\gamma$, $e\gamma$, $\mu\mu\gamma$ and $\tau\tau\gamma$.

Experimental Environment

The CERN laboratory, located just outside Geneva in Switzerland, was home of the Large Electron Positron (LEP) collider. It was recently decommissioned in December 2000 after 10 years of remarkable operation. Particles created in e^+e^- collisions were detected by four large all-purpose detectors ALEPH, DELPHI, L3 and OPAL.

During its first phase of operation from 1990 to 1995, LEP produced millions of Z^0 bosons which allowed physicists to study to unprecedented precision the various properties of this particle and test the Standard Model to a precision better than one part in 10^4 . Phase 2 of LEP operation (LEP2) began in 1995 after major upgrades of various accelerator components which increased the rate of collisions and the centre-of-mass energy. The substantial amount of data recorded combined with the highest centre-of-mass energy ever reached in e^+e^- collisions provided a unique environment to search for new phenomena beyond the Standard Model.

This chapter first presents some details of LEP operation and describes the various components of the OPAL detector relevant for this work. The recording of data and subsequent reconstruction of events are also briefly discussed. Finally, the data set and various event simulation programs used are described.

3.1 The Large Electron Positron Collider

The Large Electron Positron collider [8] was a 26.6 km in circumference storage ring commissioned in 1989. The ring consisted of eight 500 m long straight sections interspaced with eight 2.8 km arcs. All LEP components were contained in a tunnel approximately 100 m underground. Electron and positron beams travelled in opposite directions inside an evacuated aluminum tube of about 10 cm in diameter. Dipole magnets guided the beams around the arcs while focusing of the beams was achieved by various combinations of

quadrupole and sextupole magnets. The energy needed to accelerate and subsequently maintain the two beams at the nominal collision energy was supplied by Radio Frequency (RF) resonant cavities. Electrons and positrons circulating around the ring constantly lost energy via the emission of photons. Each electron lost on average about 2% of its energy from synchrotron radiation in one revolution around the ring. In its last year of running, the LEP accelerating system consisted of 288 superconducting RF cavities (272 niobium-coated copper and 16 pure niobium) and 56 conventional copper RF cavities providing together a total RF voltage of about 3400 MV per revolution.

The two beams were made to collide at four specific points around the ring, at the heart of massive detectors (ALEPH, DELPHI, L3 and OPAL) designed to record the remnants of the collisions. During the accelerating phase, separator magnets located near the interaction regions separated the two beams to avoid collisions. When the electron and positron beams finally reached the desired energy, they were brought into collisions by turning off the separator magnets. In addition, superconducting quadrupole magnets, also located near the interaction regions, squeezed the beams down to a cross-sectional size of approximately $10 \mu\text{m}$ in the vertical plane and $250 \mu\text{m}$ in the horizontal plane. Such a small beam size was desirable in order to increase the collision rate. The rate of a particular physics process is related to the beam intensity, or luminosity \mathcal{L} , according to $\text{Rate} = \mathcal{L} \sigma$, where σ is the cross-section (or probability of occurrence) of a particular physics process. Luminosities of $10^{32} \text{ cm}^{-2}\text{s}^{-1}$ were routinely achieved at LEP.

The entire CERN accelerator complex is shown in Figure 3.1. The LEP injection system was designed to exploit the existing CERN accelerators. Electrons were initially produced by an electron gun and immediately accelerated to an energy of 200 MeV using a short linear accelerator (linac). A fraction of these electrons were then directed to a tungsten target to produce positrons. Both the positrons and the remaining electrons were further accelerated to 600 MeV by a second linac and stored in the electron-positron accumulator (EPA). Pulses (or bunches) of electrons and positrons were stored in the EPA until the next injection cycle of the Proton Synchrotron (PS). The PS, CERN's oldest accelerator, operated as a 3.5 GeV e^+e^- synchrotron. Electrons and positrons were subsequently injected into the Super Proton Synchrotron (SPS). Both PS and SPS operated in a multi-cycle mode whereby electrons and positrons were accelerated between proton cycles and thus simultaneously provided both electron/positron and proton beams to various CERN experiments. The SPS boosted the energy of electrons and positrons to 22 GeV before they were finally injected into the LEP ring. The final acceleration stage took place in

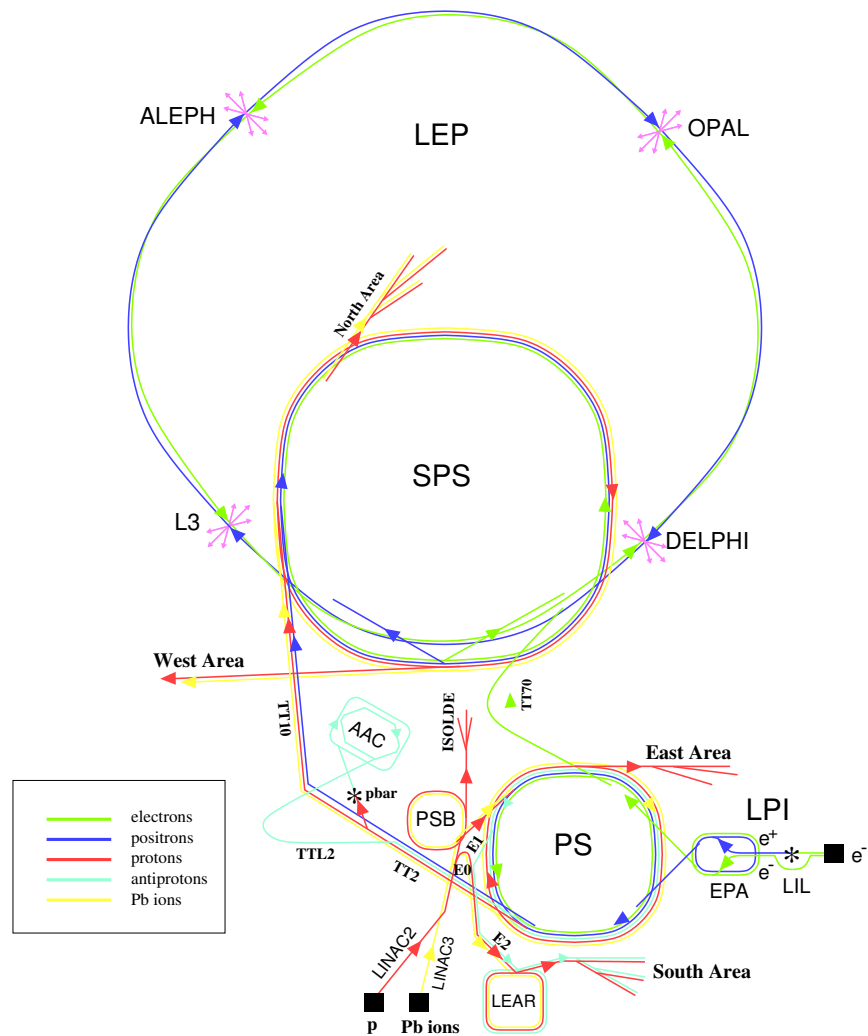
LEP where, since 1996, beams have been accelerated to energy greater than 80.5 GeV. In its last year of running, beams up to 104.5 GeV were routinely successfully brought into collision at the heart of the four LEP detectors.

The LEP storage ring mostly operated in a configuration where 4 bunches of electrons and 4 bunches of positrons circulated simultaneously in the machine. Each bunch was composed of approximately 45×10^{10} particles resulting in a total current circulating in the machine of about 5 mA at the beginning of a collision cycle. As time went by during a collision cycle, the particle density in each bunch decreased resulting in a decrease in the collision rate. The ring was emptied of its remaining circulating particles when the collision rate had decreased significantly, at which point it was more efficient to refill the machine with new particles. In its last year of running, the highest collision energies were reached using “miniramps”, a novel technique in which beams were further accelerated in small incrementing steps while in stable collision mode. Using this technique, collisions at a centre-of-mass energy of 209 GeV were achieved, an energy beyond the original machine design of 200 GeV.

Many analyses, including the work presented in this thesis, rely on a precise measurement of the collision energy. At LEP2, the beam energy was determined using nuclear magnetic resonance (NMR) probes [9] located in dipole magnets around the LEP ring. The 16 NMR probes were calibrated at lower energy using resonance depolarisation [10], a technique that can only be used for beam energy less than approximately 60 GeV. Precision on the beam energy measurement is currently limited by the uncertainty on the linear extrapolation to physics energy of the NMR probe readings. Other methods of measuring the beam energy were used as consistency checks and as a mean of estimating various systematic errors. In particular, a dedicated spectrometer [11] was installed in the fall 1999 with the aim of measuring the beam energy to a relative accuracy of one part in 10^4 . Studies of the spectrometer response necessary to achieve this goal are still ongoing. The preliminary uncertainties on the beam energy for the data set analysed varies from 20-25 MeV.

3.2 The OPAL Detector

The OPAL (Omni-Purpose Apparatus at LEP) detector [12] was one of four multi-purpose detectors at LEP. As shown in Figure 3.2, its cylindrical shape longitudinally aligned with respect to the beam direction provided nearly full angular coverage of the interaction re-



LEP: Large Electron Positron collider
 SPS: Super Proton Synchrotron
 AAC: Antiproton Accumulator Complex
 ISOLDE: Isotope Separator OnLine DEvice
 PSB: Proton Synchrotron Booster
 PS: Proton Synchrotron

LPI: Lep Pre-Injector
 EPA: Electron Positron Accumulator
 LIL: Lep Injector Linac
 LINAC: LINear ACcelerator
 LEAR: Low Ener gy Antiproton Ring

Rudolf LEY, PS Division, CERN, 02.09.96

Figure 3.1: Schematic diagram of the accelerator complex at the CERN laboratory, showing each component of the LEP injection system as well as protons/antiprotons and heavy ions accelerators.

gion¹. Particles created in an e^+e^- collision traversed different components of the detector, called subdetectors, as they travelled radially outward from the interaction region. In order of increasing radius, the first subdetectors surrounding the beam pipe consisted of a set of tracking devices which recorded the spatial position of charged particles as they moved through the subdetectors' volumes. A solenoidal coil wound outside the tracking subdetectors provided a constant uniform longitudinal magnetic field of 0.435 Tesla within the tracking volume. Surrounding the solenoidal coil, the electromagnetic calorimeter measured the energy of electrons, positrons and photons. Other types of particles occasionally deposited only a fraction of their energy in the electromagnetic calorimeter and continued their journey outward, entering next the hadronic calorimeter. Most remaining particles at this point deposited all their energy and stopped in the hadronic calorimeter. Muons however usually continued on and escaped the detector volume after traversing the outermost subdetector, called the muon chambers. In the following sections, subdetectors particularly pertinent to this work are described in more detail.

3.2.1 The Central Tracking System

The central tracking system consisted of four subdetectors: a high resolution silicon microvertex detector, a small drift chamber, a large volume jet chamber and Z-chambers. Together, these subdetectors provided information on charged particles momenta, track vertices and particle identification through ionization energy loss measurements. Figure 3.3 shows a schematic diagram of the central tracking system where the size and position of individual components can be inferred.

The silicon microvertex subdetector [13] was located in the small volume between the beam pipe and the inner wall of the pressure vessel. It provided a precise starting point for track reconstruction. This information is crucial for reconstructing possible secondary vertices resulting from the decay of short-lived particles. The silicon microvertex detector consisted of two concentric cylinders made of flat rectangular “ladders” arranged in a slightly overlapping geometry as shown in Figure 3.4. Each ladder was made of back-to-back pairs of silicon wafers oriented at an angle to each other in order to provide a measurement of both the z and ϕ directions. Read-out electronics were located at both

¹The OPAL coordinate system is defined to be right-handed, with the z -axis pointing along the electron beam direction and the x -axis pointing toward the centre of the LEP ring. The polar angle θ is measured with respect to the z -axis and the azimuthal angle ϕ is given by a rotation about the z -coordinate from the x -axis.

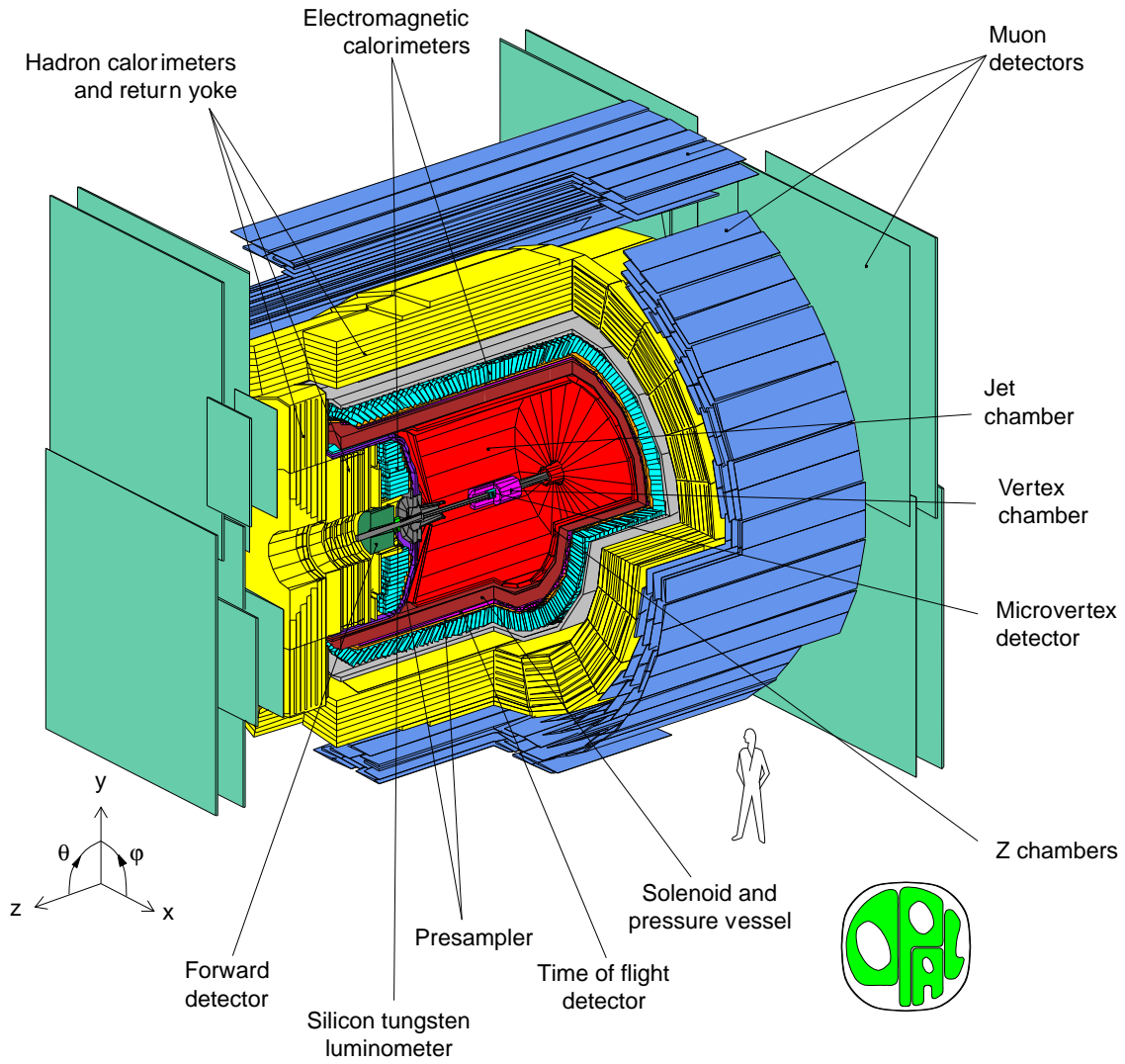


Figure 3.2: Schematic diagram of the OPAL detector showing the layout of different components.

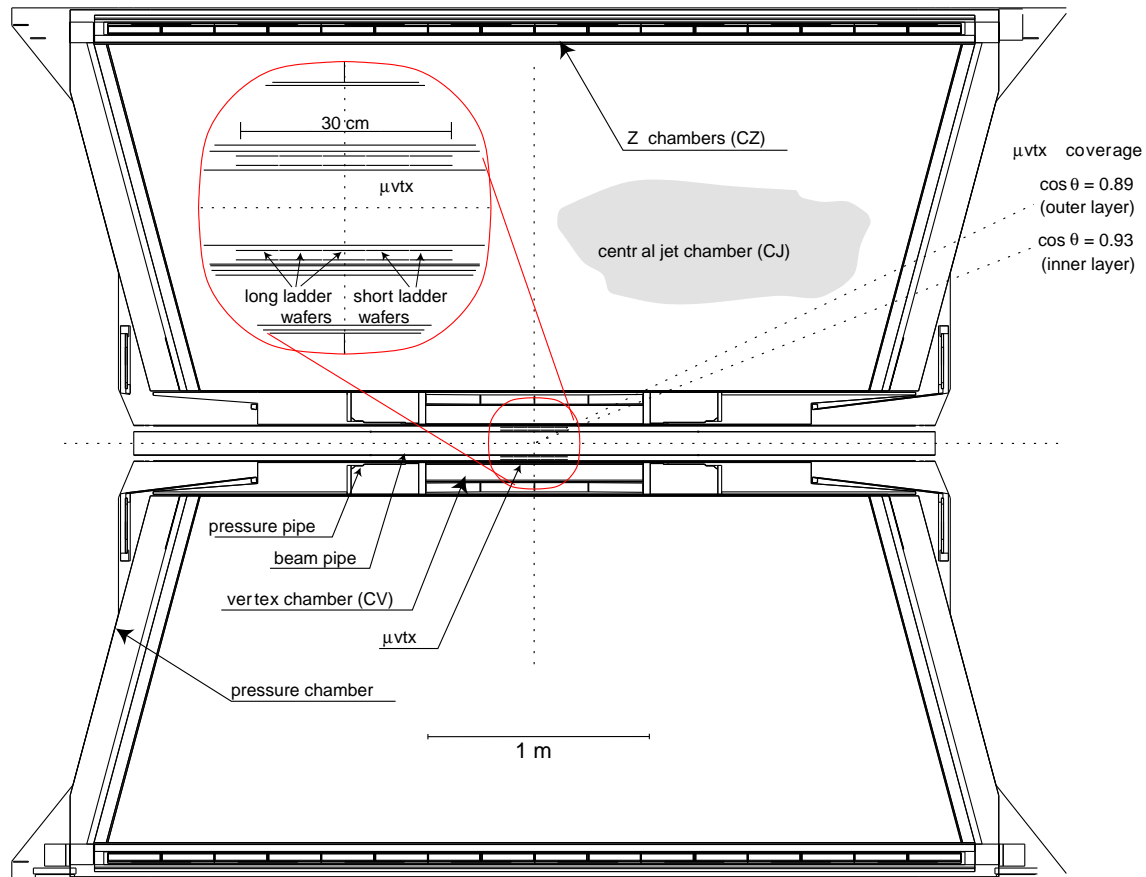


Figure 3.3: Schematic diagram of the OPAL tracking subdetectors. A Silicon microvertex surrounds the beam pipe. The central vertex drift chamber, large volume jet chamber and the Z-chambers are contained within a common pressure vessel which maintains a pressure of 4 atmospheres .

ends of each ladder. As a charged particle traversed a layer of silicon, a small current was produced and recorded as a “hit”. In the process of reconstructing the path of a charged particle, hits in the silicon microvertex were associated with the information coming from the other tracking subdetectors.

The central vertex detector, the jet chamber and the Z-chambers were drift chambers of various geometries. They were all contained in a common pressure vessel and operated within an Argon/Methane/Isobutane gas mixture at a pressure of 4 bar.

Drift chambers consist of a gas filled volume across which thin sense (anode) wires are strung and, together with cathode wires or planes, produce a constant electric field. As charged particles travel through the volume of these detectors, they ionize the surrounding

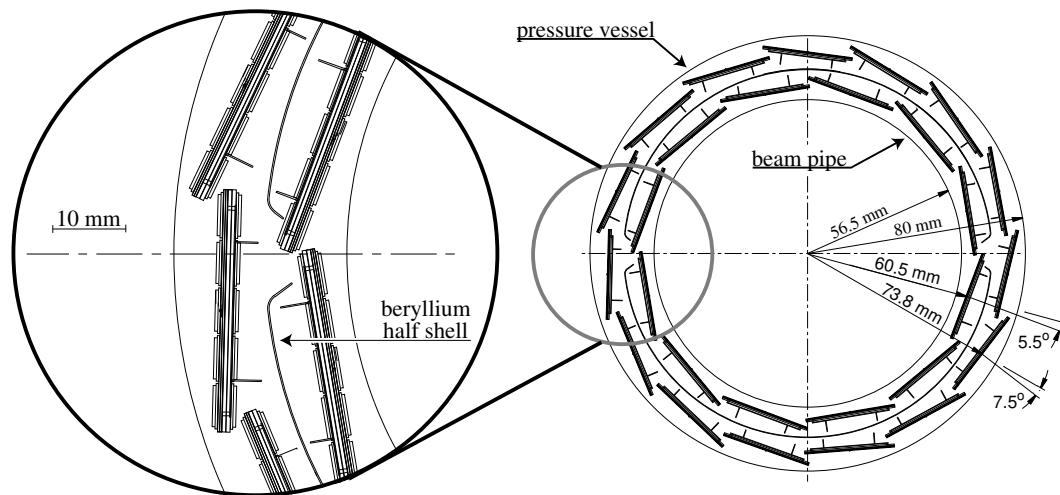


Figure 3.4: Schematic cross-sectional diagram of the OPAL silicon microvertex detector.

gas. Electrons resulting from the gas ionization drift in toward the anode wires where they cause an avalanche in the high electric field, resulting in electric pulses read out from the ends of the wires. The particular gas mixture and pressure used to operate the OPAL chambers were chosen to maximize the spatial resolution over the widest possible momentum range and obtain precise measurements of a charged particle ionization energy loss in the gas.

The central vertex detector [14] was a small cylindrical drift chamber of 1 m in length and 23.5 cm radius. It consisted of an inner layer of axial wires strung longitudinally and an outer layer composed of stereo wires mounted with a 4° angle between endplates. The inner layer of wires provided a high resolution spatial measurement in the r - ϕ plane while the slightly off axis stereo outer wires allowed a measurement of the z coordinate. A total of 18 hits (12 axial + 6 stereo) could be recorded for 92% of the full solid angle. Originally designed as the main vertex detector of OPAL, it has mainly been used, after the addition in 1996 of a higher resolution silicon microvertex detector, to match track segments between the jet chamber and the silicon microvertex.

The main component of the tracking system was the large volume central jet chamber [15] measuring 4 m long and extending from an inner radius of 0.5 m to an outer radius of 3.7 m. The chamber was composed of 24 identical pie shaped sectors each containing 159 longitudinally strung anode wires and two cathode wire planes forming the boundaries between adjacent sectors. Anode wires were staggered by $100 \mu\text{m}$ to resolve the left-right

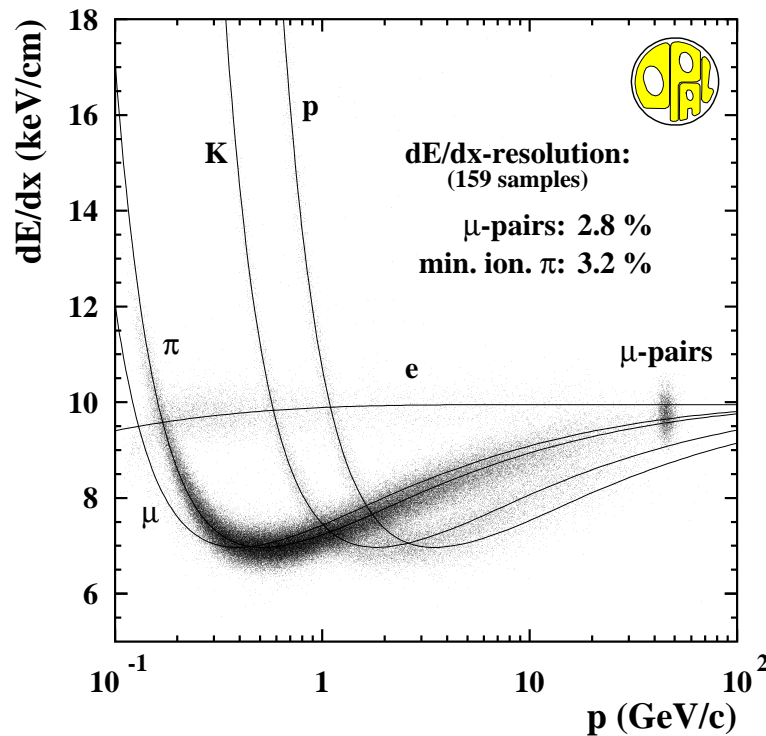


Figure 3.5: Scatter plot showing the measured ionization energy loss (dE/dx) of tracks contained in hadronic and muon pair events. The solid lines show the energy loss predicted by the Bethe-Bloch equation [16].

ambiguity of a signal recorded on a given wire. Full three dimensional spatial information was extracted from the position of the wire (r), the measured drift time of electrons to the anode (ϕ) and the ratio of the integrated charges at both ends of the wire (z). In addition, the total integrated charges on a wire provided a measurement of a particle's ionization energy loss (dE/dx) in the gas.

A total of 159 wire hits along a charged particle trajectory in the jet chamber could be recorded for 73% of the total solid angle. As charged particles travelled radially outward, their trajectories were bent by the constant longitudinal magnetic field of the magnet wound around the outside of the tracking detectors. The curvature of a track as measured in the central jet chamber is directly proportional to the particle momentum component transverse to the beam direction. Combined with a measurement of the ionization energy loss in the gas, good particle identification could be achieved. Figure 3.5 shows the ionization energy loss of different types of particles as function of their momentum. The charge of a particle could be inferred from the direction of curvature in the magnetic field.

Finally, an accurate measurement of the z -coordinate of a particle trajectory was possible using the Z-chambers [17]. These 24 thin rectangular drift chambers were mounted longitudinally around the outside of the jet chamber. Each chamber was 4 m long, 50 cm wide and 59 mm thick. The Z-chambers covered the polar angle region between 44° and 136° . Unlike the vertex and central jet chambers, wires in the Z-chambers were strung perpendicular to the beam direction in order to precisely measure the z -coordinate of particles leaving the jet chamber. A total of six layers of anode wires were positioned at increasing radii. A spatial resolution in the z -direction better than $300 \mu\text{m}$ was achieved. A measurement of the ϕ coordinate of a track is also obtained using a charge division method in order to facilitate matching hits with tracks observed in the central jet chamber.

The combined performance of the tracking subdetectors resulted in a momentum resolution of $\sigma_p/p^2 \approx 1.6 \times 10^{-3} \text{ GeV}^{-1}$ and a spatial resolution of the impact parameter in the plane perpendicular to the beam axis (d_0) of $21 \mu\text{m}$.

3.2.2 Calorimeters

Calorimeters are detectors that measure the energy of particles. The calorimetry system of the OPAL detector consisted of electromagnetic and hadronic calorimeters, the main components of which are described briefly below.

The energy of electrons, positrons and photons was measured by the electromagnetic calorimeter [18] surrounding the tracking system. It was a total absorption calorimeter made of lead glass² blocks and divided into a barrel part and two endcaps.

Electrons, positrons and photons entering the high density lead glass initiated an electromagnetic cascade of lower energy secondary particles until all the energy of the incident particle was completely absorbed. Čerenkov light produced by relativistic charged particles in the shower was internally reflected and collected by photomultipliers glued to each block. The energy deposited by a particle was proportional to the amount of light collected. Each block represented the equivalent of 24.6 radiation lengths³ of material ensuring the full containment of most electromagnetic showers.

A total of 9440 blocks of lead glass made up the barrel part of the electromagnetic calorimeter. Each block measured approximately $10 \text{ cm} \times 10 \text{ cm} \times 37 \text{ cm}$ and weighed about 20 kg. Blocks in the barrel were arranged in a nearly pointing geometry min-

²The lead glass used in OPAL has a composition of (% by weight) 23.90% SiO_2 and 74.80% PbO .

³A radiation length (X_0) is defined to be the mean distance over which a high energy electron loses all but $1/e$ of its energy by bremsstrahlung.

imizing the probability of a particle traversing more than one block while preventing neutral particles from escaping through gaps between blocks. Due to tight geometrical constraints, each endcap consisted of an array of 1132 lead glass blocks mounted parallel to the beam line. The barrel and both endcaps together covered 98% of the total solid angle. The energy resolution of the electromagnetic calorimeter was approximately $\sigma_E/E = 1.5\% \oplus 16\%/\sqrt{E[\text{GeV}]}$ [19, 20] where the first term represents instrumental uncertainties and the second corresponds to inherent fluctuations in the development of electromagnetic showers. A spatial resolution for electromagnetic showers of about 5 mm was also achieved.

The instrumented iron return yoke of the magnet, surrounding the electromagnetic calorimeter, formed the hadronic calorimeter [21]. The hadronic calorimeter was used to measure the energy of hadronic showers and help in identifying muons. This sampling calorimeter, made of a barrel part and two doughnut-shaped endcaps, consisted of layers of 100 mm thick iron plates interspersed with limited streamer tube chambers. The hadronic calorimeter corresponded to 4 interaction lengths⁴ of material. Most particles which penetrated through the 2.2 interaction lengths of material in front of the hadronic calorimeter were absorbed before reaching the muon chambers. The energy of a hadronic shower was estimated by combining the information from both the electromagnetic and hadronic calorimeters. The energy resolution of hadronic showers was measured to be $\sigma_E/E = 17\% + 85\%/\sqrt{E[\text{GeV}]}$ using pions from τ decays [22].

The luminosity recorded by the OPAL detector was measured by two silicon-tungsten calorimeters encircling the beam pipe at ± 2.385 m from the interaction region in the z direction. Since the production cross-section of electron pair events at small angles is well-known, the luminosity recorded by the OPAL detector could be calculated by simply counting the number of e^+e^- events observed in the silicon-tungsten calorimeters. These two cylindrical sampling calorimeters covered the small polar angle region between 26 mrad and 59 mrad. They were made of 18 tungsten plates interleaved with 19 layers of silicon wafers. In order to obtain a luminosity measurement to better than 0.1%, the electron trajectories had to be accurately measured. The chosen silicon-tungsten calorimeter design allowed one to determine the radial position of electron showers in the calorimeters to a precision of 0.2 mm.

⁴Length scale used to describe hadronic cascades defined to be $\lambda_I \approx 35 \text{ g cm}^{-2} \text{A}^{1/3}$.

3.2.3 Muon Chambers

The muon chambers [23] made up the outermost layer of the OPAL detector. Muons primarily lose energy in matter by ionization. Therefore, they traversed the entire OPAL detector without stopping, only depositing a small amount of energy in the electromagnetic and hadronic calorimeters. The role of the muon chambers was to provide spatial information on charged particles leaving the detector. Muons were identified by matching hits in the muon chambers with tracks measured in the central tracking system. The muon detection system was divided into a barrel part and two endcaps, together covering 93% of the total solid angle. The barrel section consisted of four layers of large area drift chambers arranged in a slightly overlapping geometry to avoid gaps between chambers. The endcaps were made of 4 layers of streamer tubes arranged perpendicular to the beam direction to form an area of approximately 150 m^2 at both ends of the OPAL detector. The muon chambers achieved a spatial resolution of 2 mm.

3.3 Data Acquisition

A trigger system is a combination of hardware and software components which combine information from different subdetectors and determine whether an event should be saved for further analysis or rejected. At LEP, the crossing of electron and positron bunches at the interaction region occurred at a frequency of 22 MHz. However, most of the time, the electron and positron bunches simply passed through each other. Events, triggered by activity in the tracking detectors and calorimeters, were recorded at a rate of approximately 5 to 10 Hz. Approximately half of the recorded events were not from genuine electron-positron collisions but from different sources of background such as beam-wall collisions and cosmic rays. Digitized information from all subdetectors pertinent to an event was merged into a single data structure of 10 kbytes on average. A software system then performed a fast analysis of the selected events which permitted an online monitoring of data quality and subdetector's performance. Events kept for further analysis were archived both on 1.3 Gbytes magneto-optical disks and magnetic tape cartridges. Following the archiving of events, a system of 14 dedicated Hewlett-Packard workstations fully reconstructed raw detector information from each event into tracks and clusters of energy ready for offline analysis. The fully reconstructed events were stored on disks for ease of access. Data ready for offline analysis were available in less than one hour after collisions.

3.4 OPAL Data and Simulated Event Samples

The data analysed for the work presented in this thesis were recorded at centre-of-mass energies between 183 GeV and 209 GeV during the LEP runs in the years 1997 to 2000. The analysis is based on a total of 684.4 pb^{-1} of data⁵ for which all relevant detector components were fully operational. In order to accurately interpret the results in terms of limits on excited lepton masses and couplings, the data were divided into 16 centre-of-mass energy bins analysed separately. The energy range, luminosity weighted mean centre-of-mass energy and integrated luminosity of each bin are summarised in Table 3.1. In addition to the high energy data, approximately 10 pb^{-1} of calibration data collected in the year 1997 to 2000 at a centre-of-mass energy near the Z^0 mass were used to study the detector response.

Distributions of various kinematical quantities and overall properties of events are compared to the Standard Model predictions using Monte Carlo techniques [24]. Large numbers of e^+e^- collisions were simulated by various Monte Carlo event generators which output lists of four-vectors containing information on the final state particles for each simulated event. These four-vectors were then processed through a GEANT [25] simulation of the OPAL detector and saved into a data structure similar to raw OPAL data. Finally, simulated events were fully reconstructed using an identical procedure as that used for real data. In some cases, corrections were applied to some Monte Carlo samples in order to improve their modelling of real data. Comparisons between real data and simulated events are crucial in understanding the physics of the underlying process studied. Efficiency calculations and many estimates of possible systematic effects, for example, are carried out using simulated events.

All dominant Standard Model processes occurring in e^+e^- collisions were simulated using a variety of Monte Carlo event generators. In order to properly model the data, simulated event samples were generated at 11 different centre-of-mass energies (183, 189, 192, 196, 200, 202, 204, 205, 206, 207, 208 GeV) approximately corresponding to the energies at which most data were recorded. Table 3.2 lists all the Monte Carlo event generators and the total effective luminosity combining all the samples at different centre-of-mass energies used in this analysis.

⁵The time integrated luminosity ($\int \mathcal{L} dt$) is commonly used as a measure of the amount of data recorded at a particle colliding experiment. It is expressed in units of inverse barns (b^{-1}) where $1 \text{ barn} = 10^{-24} \text{ cm}^2$. The number of events of a particular type collected by an experiment is given by the product of the integrated luminosity and the cross-section of the process.

\sqrt{s} bin range (GeV)	$\langle \sqrt{s} \rangle$ (GeV)	\mathcal{L} (pb^{-1})
178.00 - 186.00	182.7	63.8
186.00 - 190.40	188.6	183.2
190.40 - 194.00	191.6	29.3
194.00 - 198.00	195.5	76.5
198.00 - 201.00	199.5	76.9
201.00 - 203.75	201.9	44.5
203.75 - 204.25	203.9	1.5
204.25 - 204.75	204.6	9.7
204.75 - 205.25	205.1	60.0
205.25 - 205.75	205.4	3.6
205.75 - 206.25	206.1	14.3
206.25 - 206.75	206.5	107.3
206.75 - 207.25	206.9	5.7
207.25 - 207.75	207.5	0.5
207.75 - 208.25	208.0	7.2
> 208.25	208.3	0.5
		684.4

Table 3.1: The luminosity weighted mean centre-of-mass energy and integrated luminosity of each energy bin.

The single ($e^+e^- \rightarrow \ell^*\ell$) and pair ($e^+e^- \rightarrow \ell^*\ell^*$) production of excited leptons were simulated using the EXOTIC [37] Monte Carlo event generator. The matrix elements [38] implemented in EXOTIC include all the spin correlations in the production and decay of excited leptons as well as a complete description of the transition between 3-body to 2-body decays. Samples of 1000 events were generated at different excited lepton masses and centre-of-mass energies.

Physics process	Event Generator	Luminosity (fb ⁻¹)
$e^+e^- \rightarrow e^+e^-(\gamma)$	BHWIDE [26]	9.47
$e^+e^- \rightarrow e^+(e^-)\gamma$	TEEGG [27]	5.04
$e^+e^- \rightarrow \mu^+\mu^-(\gamma)$	KK2F [28]	99.11
$e^+e^- \rightarrow \tau^+\tau^-(\gamma)$	KK2F	101.99
$e^+e^- \rightarrow q\bar{q}(\gamma)$	KK2F/PY6.125 [29]	34.15
$e^+e^- \rightarrow \nu\bar{\nu}(\gamma)$	NUNUGPV [30]	80.63
$e^+e^- \rightarrow \gamma\gamma(\gamma)$	RADCOR [31]	23.66
$e^+e^- \rightarrow 4 \text{ fermions}$	KORALW [32] grc4f 2.1 [33]	510.03
$e^+e^- \rightarrow \gamma^{(*)}\gamma^{(*)} \rightarrow (e^+e^-)f\bar{f}$	PHOJET [34] HERWIG [35] Vermaseren [36]	43.96

Table 3.2: Summary of event generators used to simulate the Standard Model processes and the total effective integrated luminosity used in the analysis for each process combining all the different centre-of-mass energy samples.

Selection of Candidate Events

This chapter describes the set of criteria used to isolate specific event types expected from the production and subsequent decay of charged excited leptons. General requirements applied to all types of events are first presented, followed by a description of the selections designed to identify events containing two leptons and two photons ($ll\gamma\gamma$), two leptons and one photon ($ll\gamma$) and one electron and one photon ($e\gamma$). The selections presented here were developed specifically for this analysis.

4.1 Preselection

Event final states expected from the production and electromagnetic decay of excited leptons contain no more than two leptons and two photons. These events, in contrast with multihadronic events¹, contain a small number of observed tracks and energy clusters in the detector, and are selected by requiring at least one but no more than six good tracks in an event. Good tracks are defined as charged particle trajectories reconstructed from a large number of hits on consecutive wires in the central tracking detector. Quality requirements are also imposed on electromagnetic and hadronic energy clusters deposited in the detector. The entire set of track and cluster quality requirements is summarised in Appendix A.

Collisions between high energy electrons or positrons and remaining gas molecules in the beam pipe or with the pipe itself can sometimes result in background in the detector. These beam-gas and beam-wall collisions mostly produce low energy secondary particles that often get absorbed in the few inner layers of the detector leading to short reconstructed

¹Events composed of many hadrons. These originate from quark producing processes such as $e^+e^- \rightarrow q\bar{q}$. Due to the nature of the strong force, primary quarks combine with other quarks, created from vacuum fluctuations, to form various types of hadrons in a process known as hadronisation.

tracks that do not point back to the e^+e^- interaction vertex. These background events are substantially reduced by requiring that the fraction of the number of good tracks to the total number of tracks reconstructed in the central detector be greater than 0.2

Cosmic rays travelling through or interacting in the detector are a further source of background events. The background from cosmic rays is reduced to a negligible level using the timing measurements from the time-of-flight counters and tracking information from the central tracking detectors. Events are rejected if they are not in time with the beam crossing or if reconstructed tracks do not point back to the interaction region.

Tracks and energy clusters are grouped together into ‘jets’ using the algorithm described in [39]. Jets are formed by iteratively looking at individual tracks and energy clusters, adding together the 4-momentum vectors of every additional object contained within a cone of 0.25 radians about the direction of the track or cluster under consideration. If the total energy contained in the cone is greater than 2.5 GeV, then the group of tracks and energy clusters is identified as a jet. The procedure is repeated until all possible jets in an event are found. A jet can, but is not required to contain one or more tracks. The parameters defining a jet were chosen to maximise the efficiency at detecting excited lepton events over the broadest possible range of masses and centre-of-mass energies. Events containing between two and four jets, inclusive, are retained.

A total of about 2.3 million events are selected by the above criteria out of approximately 96 million events.

4.2 Jet Classification

Each jet in an event is classified as a type of lepton or photon according to the criteria described below. The order in which the different classifications are presented represent the order in which they are applied to each jet. A jet can only be identified as one type of lepton or a photon.

4.2.1 Photon Identification

Photons travelling through the OPAL detector do not leave hits in the central tracking system owing to their neutral electric charge. They eventually stop in the electromagnetic calorimeter, depositing all their energy.

Jets containing a cluster of energy in the electromagnetic calorimeter and no tracks

are tagged as photons. To ensure that an electromagnetic energy cluster in a jet genuinely corresponds to a particle, all photon candidates are required to contain a minimum amount of energy equivalent to 5% of the beam energy. In the forward region of the detector, photons travel through additional material such as the vertex drift chamber read-out plates and various types of cables. This additional material increases the probability of photon interactions and is difficult to model accurately. Therefore, to avoid poorly modelled regions of the detector, all photon candidates must lie within $|\cos \theta| < 0.9$ to be considered in the rest of the analysis.

At LEP2 energies, approximately 10% of photons interact with material in the detector prior to entering the electromagnetic calorimeter and convert to an electron-positron pair. The characteristic signature of a photon conversion is the presence of two oppositely charged tracks very close to each other pointing to at least one cluster of energy in the electromagnetic calorimeter. A neural network technique [40] developed to identify photon conversions is used to select these photons². Jets are identified as a converted photon if the most energetic track in the jet has a neural network output greater than 0.9, on a scale from 0 to 1. To reduce the number of fake photon conversions, in particular from hadronic particles, the associated energy deposited in the hadronic calorimeter must be less than 10% of the beam energy.

4.2.2 Muon Identification

A jet is considered a muon candidate if it contains exactly one track lying within the larger angular acceptance of $|\cos \theta| < 0.95$. Since muons do not produce electromagnetic showers or interact strongly with matter, the forward region of the detector containing additional material is well modelled. Typically, muons deposit a small amount of energy in the electromagnetic and hadronic calorimeters before traversing the muon chambers. Muon candidates are required to contain less than 3 GeV of energy deposited in the electromagnetic calorimeter. For tracks pointing to the overlap region between the barrel and endcap parts of the calorimeter, the amount of electromagnetic energy must be less than 5 GeV.

²The neural network [40] uses the information from 9 different variables to judge how likely a pair of tracks resembles what is expected from a real photon conversion. The variables used as input to the neural network are: the distance between the two tracks, the radius of the first measured hit of both tracks, the radius of the reconstructed secondary vertex, the invariant mass of the pair assuming both tracks to be electrons, the impact parameter of the reconstructed photon with respect to the primary vertex of the event, the momentum of both tracks times the sign of their charge, the output of another neural network trained to identify electrons applied to the partner track.

Furthermore, a muon candidate must either have hits in the muon chambers matched with a track in the central detector or hits in the hadronic calorimeter associated with a track and consistent with the particle being a muon. Muons that occasionally stop in the hadronic calorimeter will generally deposit their energy in the last few layers of the calorimeter without producing a large cascade of secondary particles typical of strongly interacting particles. Thus, jets containing a minimum of four hits in the hadronic calorimeter of which at least one is located in the last three layers, are considered muon candidates. In addition, the number of strips per layer hit must be less than two corresponding to a very small number of secondary particles produced.

4.2.3 Electron Identification

Electron candidates must contain exactly one track required to lie within $|\cos\theta| < 0.9$ to avoid, as for photons, poorly modelled regions of the detector. Electrons, unlike muons or hadrons, generally deposit all their energy in the electromagnetic calorimeter. Thus, for electrons, the ratio of the electromagnetic energy to the track momentum (E/p) is close to unity. Jets considered as electron candidates must satisfy $0.8 < E/p < 1.2$. Jets that do not fulfill this requirement can still be selected as electrons if the output from a neural network [40] designed to identify electrons is greater than 0.9. This criteria particularly improves the detection efficiency for low energy electrons.

4.2.4 Hadronic Tau Lepton Identification

Tau leptons are unstable particles that promptly decay to different numbers and types of particles. Taus are not directly observed in the detector but only inferred by their decay products. Taus decaying to leptons³ are tagged as electron or muon candidates by the criteria described above. Unidentified jets containing at least one track and lying within $|\cos\theta| < 0.95$ are considered to be hadronically decaying tau leptons. Jets satisfying the electron or photon requirements in the region $0.90 < |\cos\theta| < 0.95$ are discarded from the sample of tau candidates.

³The branching fraction of taus into leptons is about 35%.

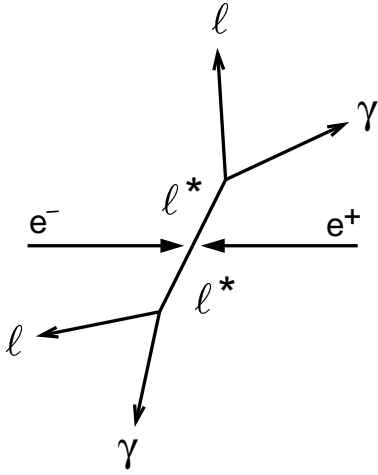


Figure 4.1: Schematic diagram representing the production of a pair of excited leptons (ℓ^*) and their subsequent decay. Due to their predicted short lifetime, only the decay products of the excited leptons would be observed in the detector.

4.3 Event Selection

In the context of a search for excited leptons decaying electromagnetically, three different types of event final states are studied: $\ell\ell\gamma\gamma$, $\ell\ell\gamma$ and $e\gamma$ events. The particular characteristics of each final state and the criteria used to identify these types of events are described in the following sections.

4.3.1 Selection of $\ell\ell\gamma\gamma$ Final States

The production and subsequent electromagnetic decay of a pair of excited leptons would result in events observed in the detector containing exactly two leptons and two photons. A schematic diagram of this reaction is shown in Figure 4.1 where the flight paths of the excited leptons have been exaggerated for illustrative purposes only.

Candidate events for the pair production of excited leptons are required to contain exactly two lepton candidates of the same flavour and two photons in the event. Events containing two leptons of a different flavour and two photons are selected as $\tau\tau\gamma\gamma$ candidates.

For $ee\gamma\gamma$ and $\mu\mu\gamma\gamma$ candidates, the sum of the energy of the two leptons and two photons is expected to add up to the centre-of-mass energy of the collision. Figure 4.2 shows the distributions of the variable R_{vis} , defined as the sum of the energies of the two leptons and two photons divided by the centre-of-mass energy. Candidate events are required to have a value of R_{vis} greater than 0.8 for $ee\gamma\gamma$ and $\mu\mu\gamma\gamma$ candidates and greater than 0.4 for $\tau\tau\gamma\gamma$ candidates where some energy is lost due to the presence of neutrinos in the event. This criteria almost completely eliminates background events from Standard

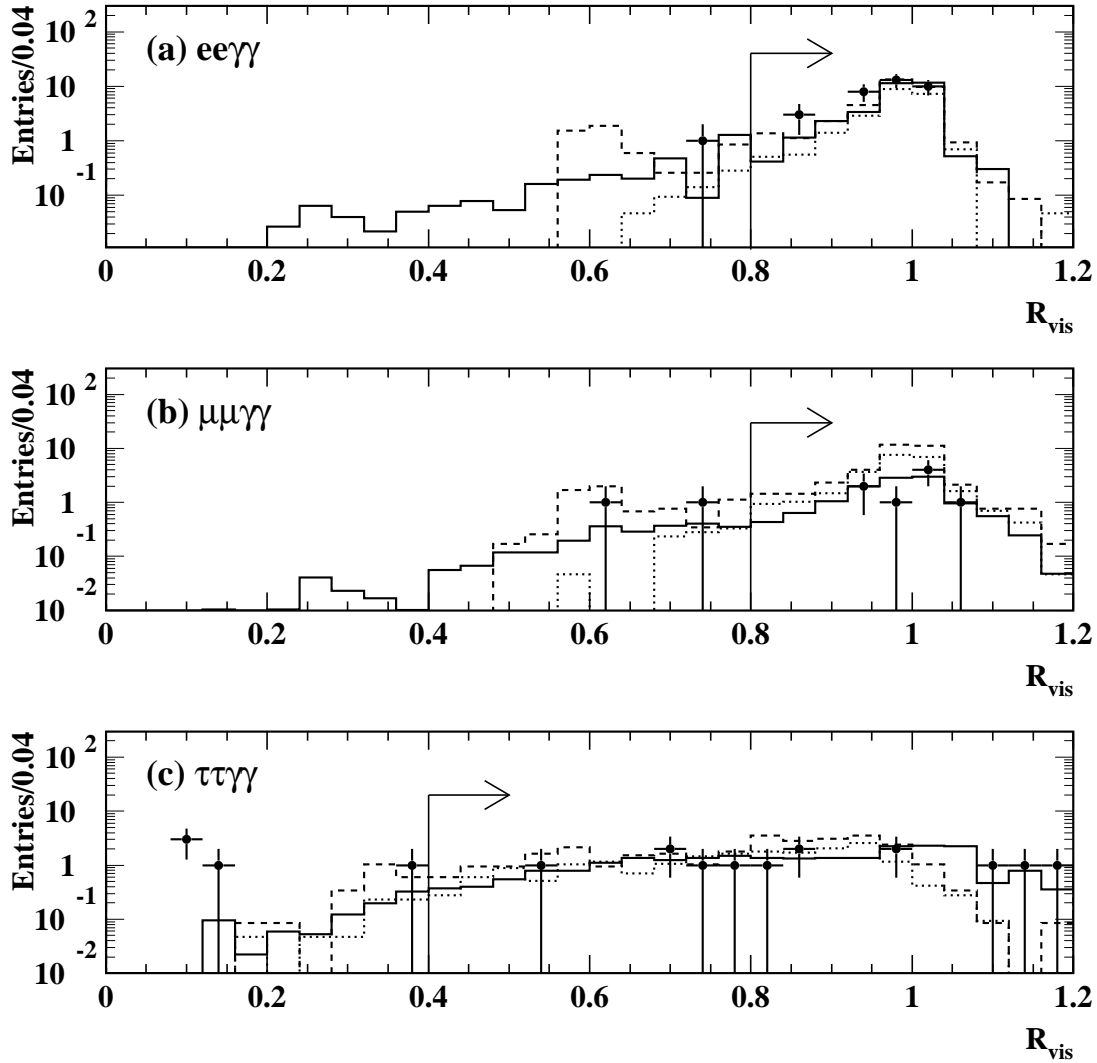


Figure 4.2: Distributions of the sum of the energies of the two leptons and two photons divided by the centre-of-mass energy (R_{vis}) for pair production candidate events. The points represent the data from all centre-of-mass energies combined while the solid lines show the total expected background from Standard Model processes. The dashed and dotted lines represent an example of pair produced excited lepton events with arbitrarily chosen masses of 40 GeV and 90 GeV, respectively, and with an electromagnetic branching fraction calculated assuming a coupling over compositeness scale of $f/\Lambda = 1 \text{ TeV}^{-1}$. The arrows indicate the position of each cut.

Model two-photon interactions ($e^+e^- \rightarrow (e^+e^-)l\bar{l}$ or $(e^+e^-)q\bar{q}$). Two-photon events typically contains particles produced in the forward region outside the detector acceptance resulting in events with a large amount of missing energy.

The remaining background in the $ee\gamma\gamma$ and $\mu\mu\gamma\gamma$ samples is composed almost entirely of Standard Model electron and muon pair events with more than one photon radiated off the leptons. The background in the $\tau\tau\gamma\gamma$ sample consists mostly of radiative $\tau^+\tau^-$ events and a small fraction of $q\bar{q}$ events. A total of 34, 8 and 13 events in the entire data set are selected as $ee\gamma\gamma$, $\mu\mu\gamma\gamma$ and $\tau\tau\gamma\gamma$ candidates, respectively. Examples of candidate events of each type selected by the requirements described above are shown in Figure 4.3.

4.3.2 Selection of $ll\gamma$ Final States

Events consisting of two leptons and one photon are the characteristic signature expected from singly produced excited leptons. The schematic diagram of Figure 4.4 illustrates the mechanism producing such final states.

Events considered as $ll\gamma$ candidates must contain two lepton candidates of the same flavour and at least one photon. In addition, events with two leptons of a different flavour and at least one photon are tagged as $\tau\tau\gamma$ candidates. If more than one photon is identified in the event, the most energetic photon is chosen and the other one is ignored. Events selected as candidates for the pair production of excited leptons by the criteria described in the previous section are also considered as single production candidates.

Typical $ee\gamma$ and $\mu\mu\gamma$ events resulting from the single production of excited electrons and muons are expected to have very little missing energy, i.e. the sum of the energies of the two leptons and most energetic photon should approximately add up to the centre-of-mass energy of the e^+e^- collision. Distributions of the quantity R_{vis} , defined as the sum of the energies of the two leptons and one photon scaled by the centre-of-mass energy, are shown in Figure 4.5. Only $ee\gamma$ and $\mu\mu\gamma$ events with a value of R_{vis} greater than 0.8 are retained. Due to the presence of neutrinos produced in the decay of tau leptons, events selected as $\tau\tau\gamma$ candidates must have, instead, a value of R_{vis} greater than 0.4.

The observed discrepancies at small values of R_{vis} in Figure 4.5(a) and (b) correspond to a region where the background is dominated by leptonic two-photon events ($e^+e^- \rightarrow (e^+e^-)l\bar{l}$). The discrepancy is less pronounced in the $\tau\tau\gamma$ sample since additional Standard Model processes, such as four-fermion and two-fermion interactions,

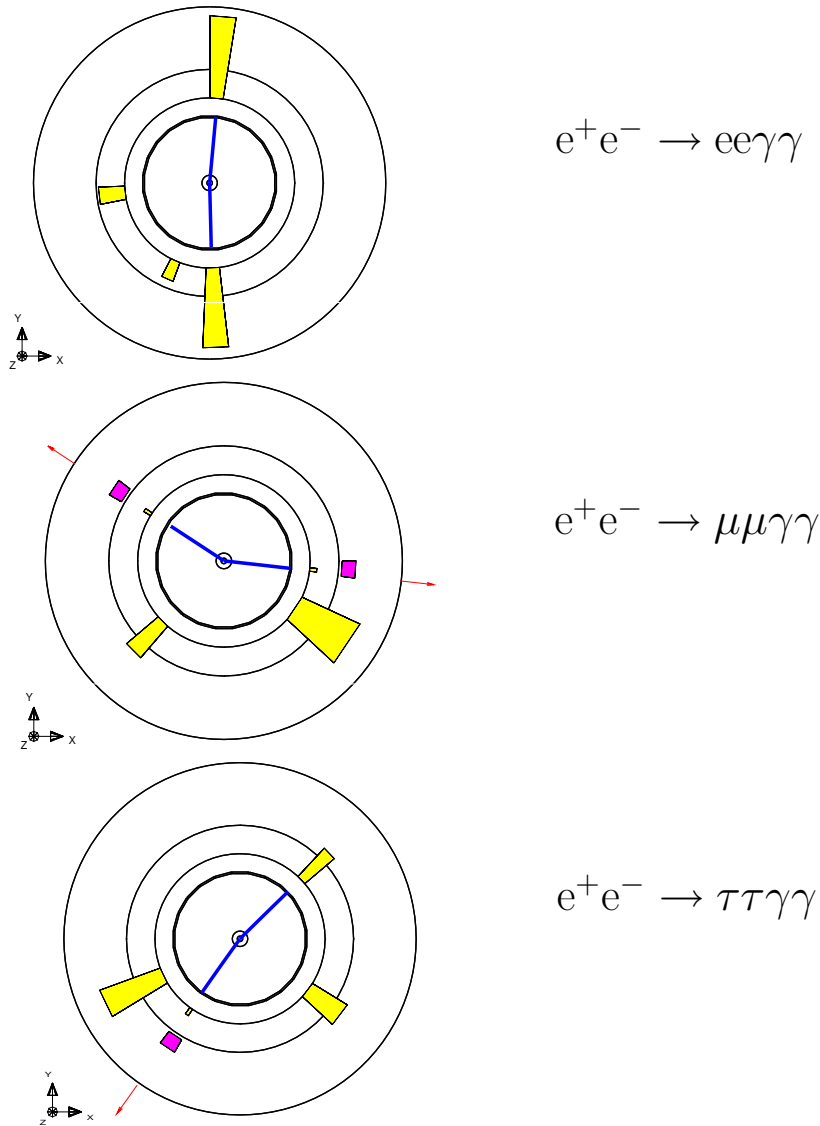


Figure 4.3: Examples of $ee\gamma\gamma$, $\mu\mu\gamma\gamma$ and $\tau\tau\gamma\gamma$ candidate events in the data selected by the criteria described in the text. Each figure shows a cross-section of the OPAL detector where each concentric circle represents the boundary of a detector system. The electron-positron beams travel in the direction perpendicular to the plane of the paper and collide at the centre of each picture. Lines travelling outward represent tracks produced by charged particles. Light and dark grey boxes represent energy deposited in the electromagnetic and hadronic calorimeters, respectively. The size of the boxes is proportional to the amount of energy deposited. Arrows indicate hits in the muon chambers. The $ee\gamma\gamma$, $\mu\mu\gamma\gamma$ and $\tau\tau\gamma\gamma$ events shown were recorded at a centre-of-mass energy of 188.7, 188.7 and 204.8 GeV, respectively.

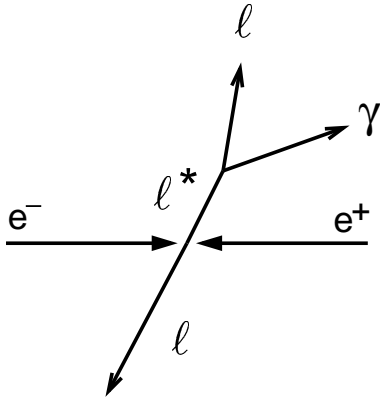


Figure 4.4: Schematic diagram representing the production of an excited lepton in association with a Standard Model lepton. The excited lepton is expected to decay promptly leading to event final states containing two leptons and one photon.

contribute in producing events with small values of R_{vis} . This mis-modelling does not affect the analysis since the event final states of interest lie in a region of R_{vis} that is well modelled.

The background in the $ee\gamma$ sample is further reduced by requiring that the angle between the most energetic electron and photon ($\theta_{e\gamma}$) be greater than 90° . Figure 4.6 shows the $\theta_{e\gamma}$ distribution obtained for all data combined and for two different masses of excited electron events. The expected angle $\theta_{e\gamma}$ measured for signal events depends on the mass of the excited electron produced. For masses close to the kinematic limit, the excited electron would be produced almost at rest in association with a low energy electron, resulting in its decay products travelling mostly back-to-back. Conversely, an excited electron with a smaller mass would be produced with a non-negligible momentum fraction resulting in its decay products being boosted in its momentum direction. The electron recoiling against the excited electron, in this case, could also have higher energy than the electron produced by the decay of the excited state. For small masses, the $\theta_{e\gamma}$ distribution expected from the production of excited electrons is thus broader and has a smaller mean angle than for larger excited lepton masses. The search for singly produced excited leptons primarily focuses on excited states with masses greater than about 90 GeV, as smaller masses would be observed in the pair production search. The cut position allows one to reduce the background from e^+e^- events without loss in signal detection efficiency for high excited lepton masses.

The sample of $\tau\tau\gamma$ events contains background from e^+e^- and $\mu^+\mu^-$ events where one electron or muon is misidentified. Electron pair events deposit most of their energy in the electromagnetic calorimeter while muon pair events deposit only very little energy. Since tau leptons decay to different types of particles, $\tau\tau\gamma$ events are expected to contain on av-

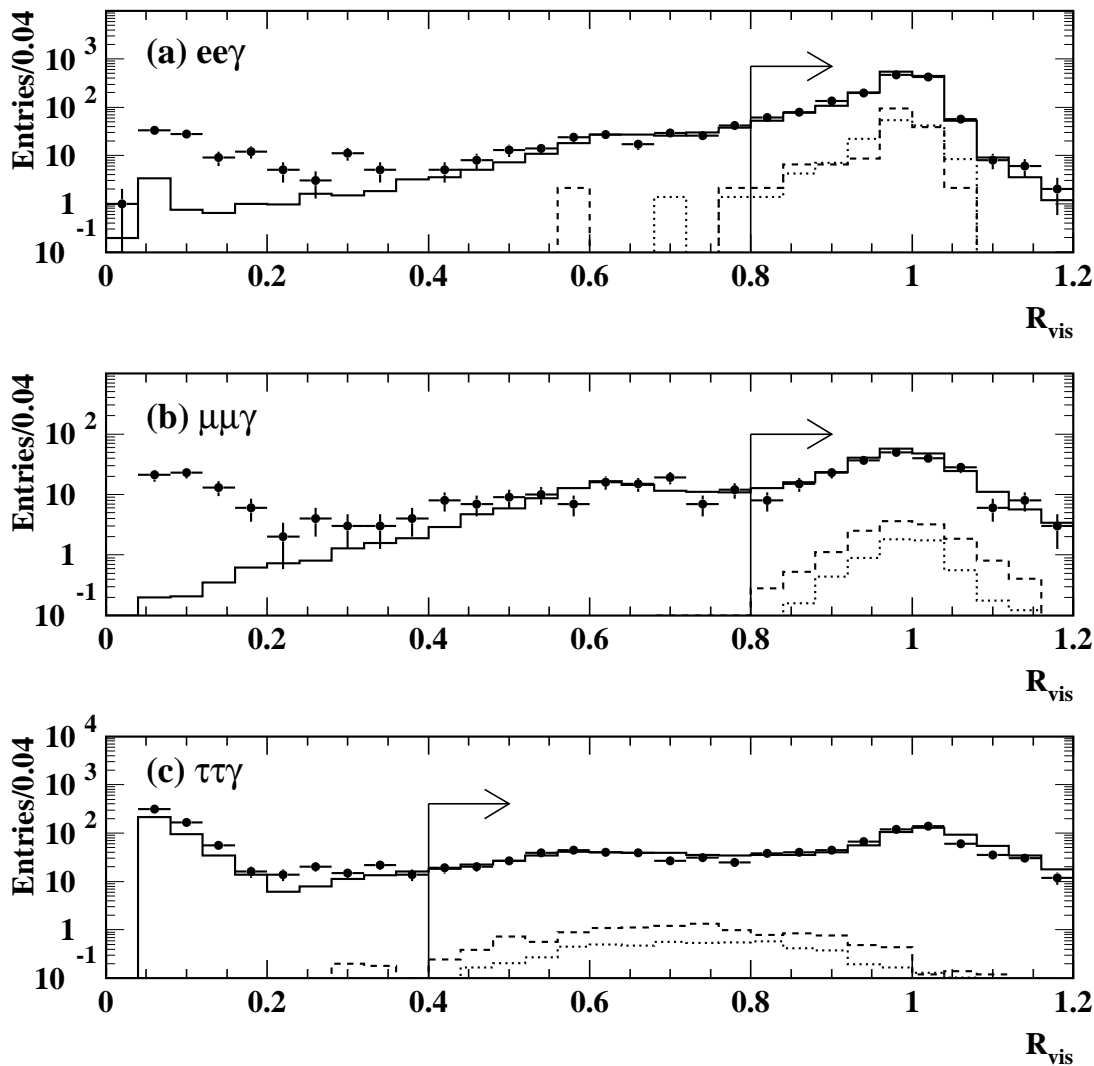


Figure 4.5: Distributions of the sum of the energies of the two leptons and one photon divided by the centre-of-mass energy (R_{vis}) for $ll\gamma$ candidate events before applying selection cuts. The points represent the data from all centre-of-mass energies combined while the solid lines show the total expected background from Standard Model processes. The dashed and dotted lines represent an example of excited lepton events with arbitrarily chosen masses of 90 GeV and 180 GeV, respectively, and with an electromagnetic branching fraction calculated assuming a coupling over compositeness scale of $f/\Lambda = 5 \text{ TeV}^{-1}$. The arrows indicate the position of each cut.

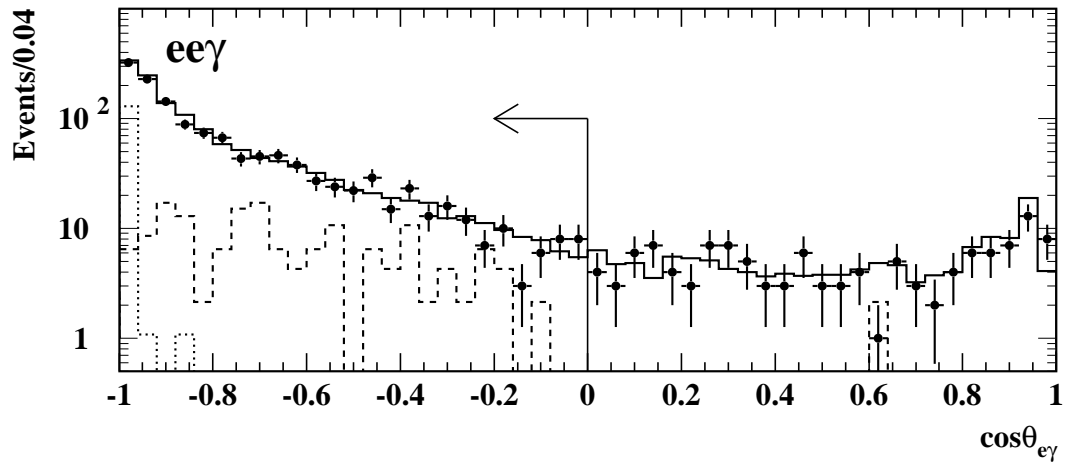


Figure 4.6: Distributions of the angle between the photon and most energetic electron for $ee\gamma$ events. Selection criteria have been applied in the order they are described in the text, up to the requirement on the quantity $\cos\theta_{e\gamma}$. The points represent data from all centre-of-mass energies combined and the solid line shows the background expected from Standard Model processes. The dashed and dotted lines represent an example of excited lepton events with an arbitrarily chosen mass of 90 GeV and 180 GeV, respectively, and with an electromagnetic branching fraction calculated assuming a coupling over compositeness scale of $f/\Lambda = 5 \text{ TeV}^{-1}$. The arrow indicates the position of the cut.

erage an amount of electromagnetic energy equivalent to about 50% of the centre-of-mass energy. Figure 4.7(a) shows the total amount of energy deposited in the electromagnetic calorimeter scaled by the centre-of-mass energy ($E_{\text{total}}^{\text{EM}}/\sqrt{s}$). The background from both e^+e^- and $\mu^+\mu^-$ events in the $\tau\tau\gamma$ sample is reduced by requiring that the total energy deposited in the electromagnetic calorimeter be between 20% and 80% of the centre-of-mass energy.

The total momentum of $\tau\tau\gamma$ candidates often does not appear to be conserved due to the presence of neutrinos produced in tau decays. The missing momentum vector of an event is defined as the vector pointing in the opposite direction to the total momentum component from all the visible particles in an event. The $\tau\tau\gamma$ events can have a missing momentum vector pointing in any direction. At LEP2 energies, events from Standard Model processes producing two fermions in the final states often contain an initial state

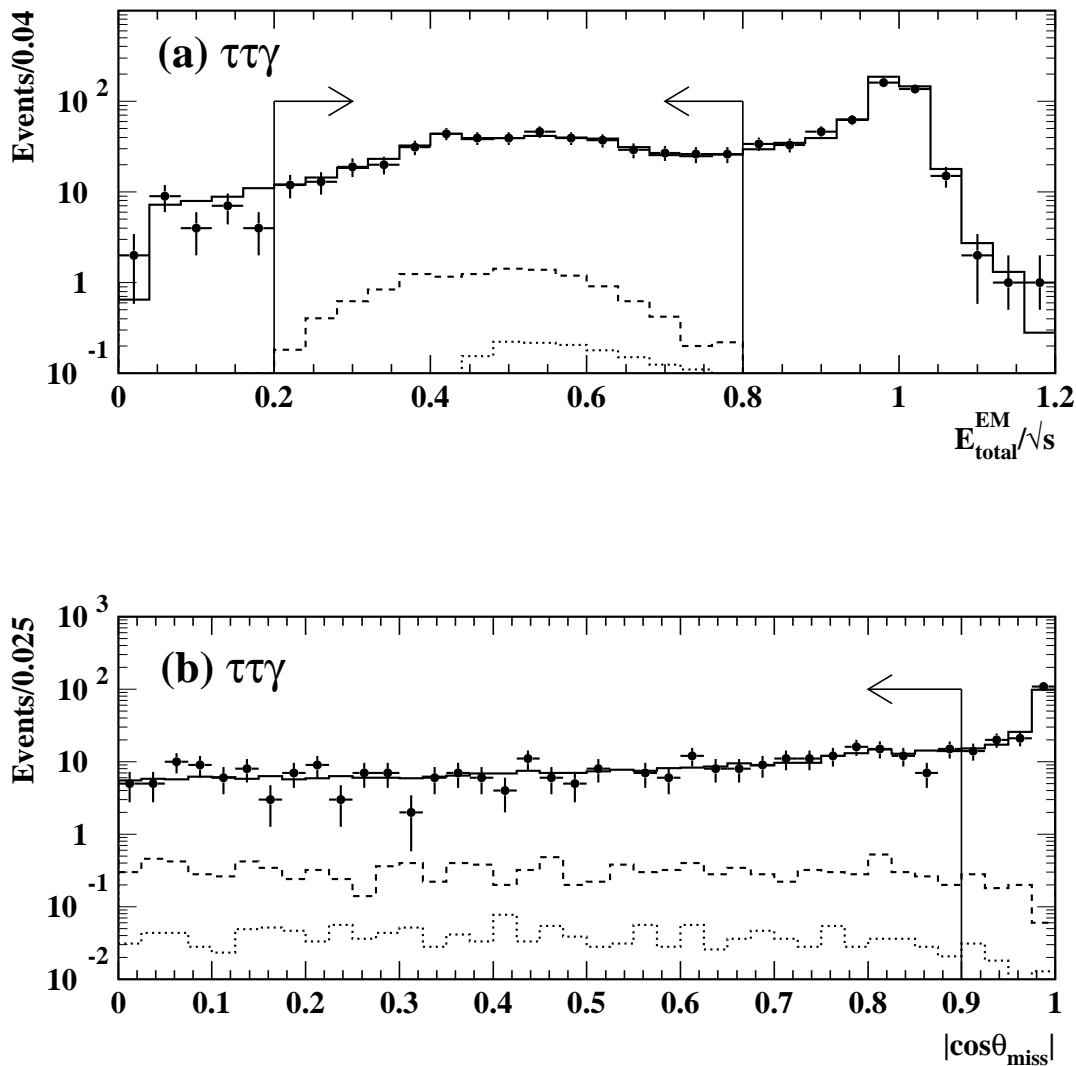


Figure 4.7: Plots of the total energy deposited in the electromagnetic calorimeter and the polar angle of the missing momentum vector for $\tau\tau\gamma$ events. Selection criteria are applied in the order they are described in the text, up to the requirement on the variable plotted. The points show the distribution obtained from data combining all centre-of-mass energies and the solid lines represent the corresponding background expectation from Standard Model processes. The dashed and dotted lines show an example of excited lepton events with an arbitrarily chosen mass of 90 GeV and 180 GeV, respectively, and with an electromagnetic branching fraction calculated assuming a coupling over compositeness scale of $f/\Lambda = 5 \text{ TeV}^{-1}$. The arrows indicate the position of the cuts.

Cut	Data	Background				
		Total	$e^+e^-(\gamma)$	$\mu^+\mu^-(\gamma)$	$\tau^+\tau^-(\gamma)$	other
<i>eeγ</i>						
2 electrons + ≥ 1 photon	1752	1715 ± 13	1671	0	18	26
R_{vis}	1440	1507 ± 12	1497	0	1	10
$\theta_{e\gamma}$	1317	1374 ± 11	1364	0	1	9
<i>$\mu\mu\gamma$</i>						
2 muons + ≥ 1 photon	424	363 ± 2	0	339	12	12
R_{vis}	235	256 ± 2	0	252	1	3
<i>$\tau\tau\gamma$</i>						
2 leptons + ≥ 1 photon	1600	1417 ± 19	596	68	309	445
R_{vis}	963	1006 ± 8	595	67	267	77
$E_{\text{total}}^{\text{EM}}/\sqrt{s}$	447	449 ± 4	93	47	250	60
$ \cos \theta_{\text{miss}} $	283	292 ± 2	17	33	209	33

Table 4.1: Numbers of selected events in the data and expected background from Standard Model processes in the $ee\gamma$, $\mu\mu\gamma$ and $\tau\tau\gamma$ samples combining data from all the centre-of-mass energies and after applying each cut. The statistical error on the total background expectation is shown.

photon emitted along the beam pipe. The missing momentum vector of these types of events thus points in the forward region of the detector. In order to reduce the background in the $\tau\tau\gamma$ sample from such events, the polar angle of the missing momentum vector is required to lie within $|\cos \theta_{\text{miss}}| < 0.9$. Figure 4.7(b) shows the $|\cos \theta_{\text{miss}}|$ distribution of $\tau\tau\gamma$ events with all other cuts applied.

Table 4.1 shows the number of selected events in the data and expected background from Standard Model processes in the $ee\gamma$, $\mu\mu\gamma$ and $\tau\tau\gamma$ samples after applying each cut described above. The remaining background in the $ee\gamma$ and $\mu\mu\gamma$ samples consists almost exclusively of radiative e^+e^- and $\mu^+\mu^-$ events while the background in the $\tau\tau\gamma$ sample consists mostly of radiative $\tau^+\tau^-$ events and a small fraction of e^+e^- , $\mu^+\mu^-$ and $q\bar{q}$ events.

4.3.3 Selection of $e\gamma$ Final State

Excited electrons are predominantly singly produced via a t -channel diagram. This production mechanism results in a large fraction of excited electrons being produced in the

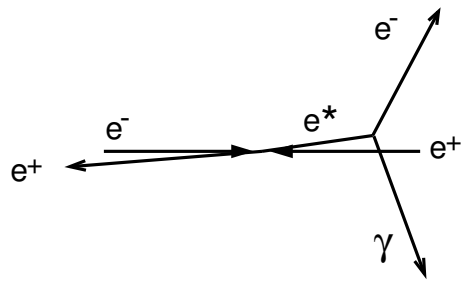


Figure 4.8: Schematic diagram illustrating the single production of excited electrons at a small angle where the associated electron is undetected. The expected prompt decay of excited electrons results in events observed in the detector containing only one electron and one photon.

forward region of the detector with the associated Standard Model electron often outside the detector acceptance. Figure 4.8 shows a schematic diagram of this type of interaction. A separate selection for events with only one electron and one photon in the final state ($e\gamma$) was thus developed to increase the efficiency for the search of singly produced excited electrons.

Candidate events are required to contain at least one photon and at least one electron. Additional jets in an event, if present, are ignored. All events selected by the set of general requirements discussed in Section 4.1 but that fail the $ee\gamma$ selection are considered as possible $e\gamma$ candidates. This requirement is necessary to avoid double-counting of events when combining results from the $ee\gamma$ and $e\gamma$ selections in order to calculate a limit on the production rate of excited electrons.

The amount of visible energy in the detector is expected to be sufficiently large to distinguish candidate events from the two-photon background. A plot of the sum of the energies of the electron and photon divided by the centre-of-mass energy (R_{vis}) is shown in Figure 4.9(a). Candidate events are required to satisfy $R_{\text{vis}} > 0.4$.

The dominant source of background in the $e\gamma$ sample is from Standard Model e^+e^- events. A requirement on the angle between the electron and the photon ($\theta_{e\gamma}$), identical to that described in Section 4.3.2, reduces the number of e^+e^- events selected with minimal loss in signal efficiency. Figure 4.9(b) shows the distribution of the angle between the electron and photon for data from all the centre-of-mass energies combined. Candidate $e\gamma$ events must satisfy $\cos \theta_{e\gamma} < 0$.

In e^+e^- events produced at small angle, it is possible for one of the electrons to be misidentified as a photon, resulting in the event being selected as an $e\gamma$ candidate. Part of this background contamination is reduced by rejecting events where the identified photon lies in the forward region of the detector ($|\cos \theta_\gamma| < 0.8$). A plot of the photon polar angle of $e\gamma$ candidate events is shown in Figure 4.9(c). In addition, events are rejected if the photon is identified as a conversion.

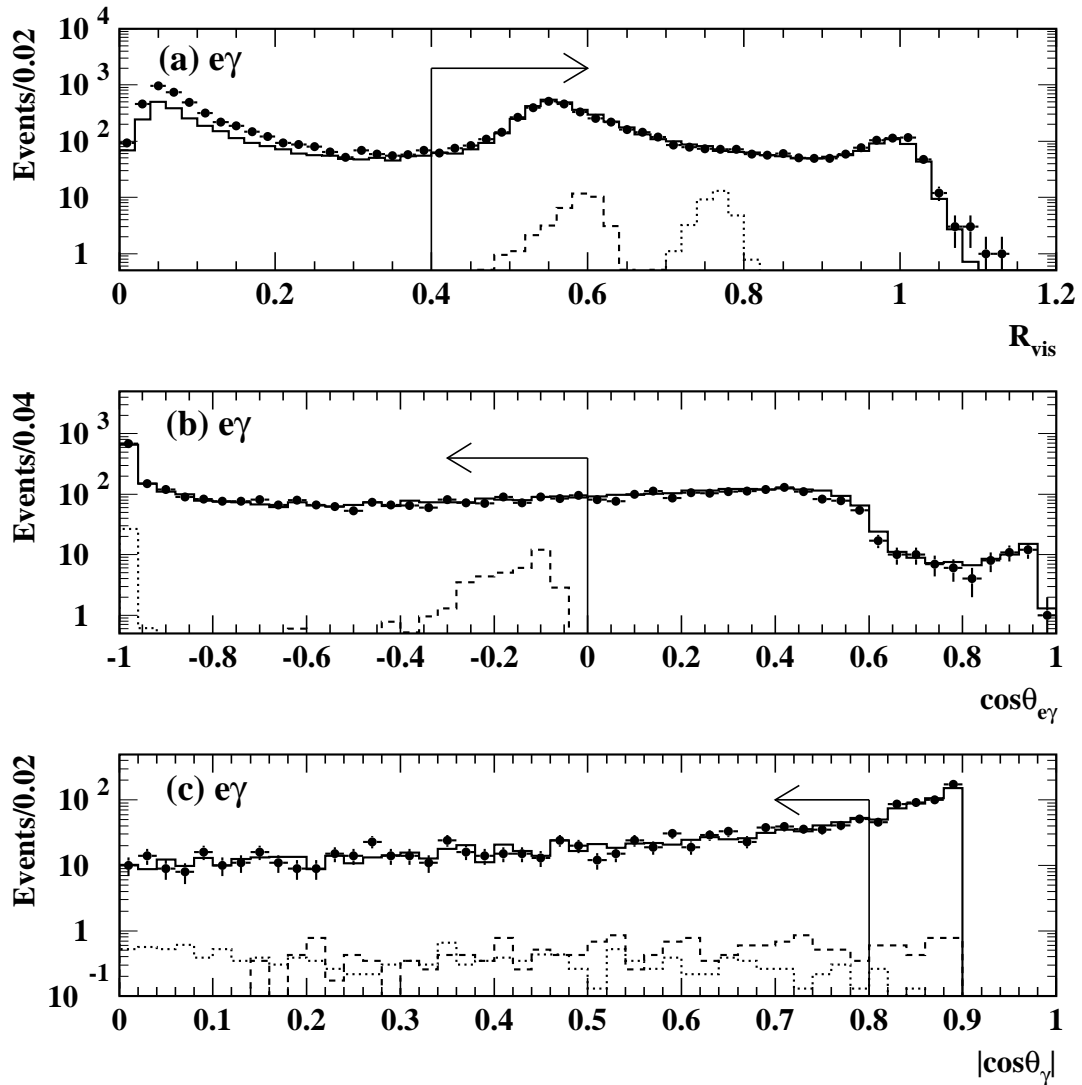


Figure 4.9: Distributions for $e\gamma$ events of (a) the sum of the energies of the electron and photon divided by the centre-of-mass energy, (b) the cosine of the angle between the electron and photon and (c) the absolute value of the cosine of the photon polar angle. Selection criteria are applied in the order they are described in the text, up to the requirement on the variable plotted. The points with error bars show the distributions of data obtained by combining all the centre-of-mass energies and the solid lines represent the expected background from Standard Model processes. The dashed and dotted lines show an example of excited lepton events with an arbitrarily chosen mass of 90 GeV and 180 GeV, respectively, and with an electromagnetic branching fraction calculated assuming a coupling over compositeness scale of $f/\Lambda = 1 \text{ TeV}^{-1}$. The arrows indicate the position of each cut.

Cut	Data	Background				
		Total	$e^+e^-(\gamma)$	$\mu^+\mu^-(\gamma)$	$\tau^+\tau^-(\gamma)$	other
≥ 1 electron + ≥ 1 photon	8970	7227 ± 35	6422	4	147	654
R_{vis}	4560	4614 ± 26	4423	2	72	118
$\theta_{e\gamma}$	2971	2880 ± 20	2698	2	67	113
$ \cos \theta_\gamma $	1795	1779 ± 16	1653	1	51	75
conversion veto	1601	1608 ± 15	1492	1	48	68

Table 4.2: Number of selected events in the data and expected background in the $e\gamma$ sample for all centre-of-mass energies combined after applying each cut. The statistical error on the total background expectation is shown.

Table 4.2 shows the number of data and expected background events, from all centre-of-mass energies combined, selected after applying each cut described above. The remaining irreducible background in the $e\gamma$ sample consists almost entirely of e^+e^- events.

Kinematic Fits

This chapter explains the kinematic fit technique used to improve the sensitivity of the search for excited leptons. A general description of this technique is first presented, followed by details of the particular implementation used in this analysis. This is the first time kinematic fits are used in the context of a search for excited leptons. The development and implementation of the fits used in this analysis are the original work of the author.

5.1 Motivation

The existence of excited leptons would reveal itself as an excess of events with identical $\ell\gamma$ reconstructed invariant mass. A kinematic fit technique is used in this analysis to improve the estimates of the energy and direction of the particles in an event. This information is then used to calculate precisely the invariant mass of each possible $\ell\gamma$ pair in an event. The improvements in the mass resolution result in an increase in the search sensitivity and discriminating power between background and excited lepton events.

5.2 General Principles

A kinematic fit is a technique used to improve the values of measured parameters and provide estimates of unknown quantities by exploiting the known physical properties of the observed process. The technique consists of finding the optimal solution to a set of equations satisfying external constraints.

Given a set of measured parameters $\hat{\alpha}$ with an associated covariance matrix \mathbf{V} , the

problem consists of finding a new set of parameters α that minimises

$$\chi^2 = (\hat{\alpha} - \alpha)^T \mathbf{V}^{-1} (\hat{\alpha} - \alpha) \quad (5.1)$$

but also satisfies the set of constraint equations given by $\mathbf{g}(\alpha, \mathbf{p})$ where \mathbf{p} is a vector of unmeasured parameters. The superscript T represents a transposed vector. The constraint equations can be incorporated in the problem using Lagrange multipliers [41], λ , and the function to minimise becomes

$$L = (\hat{\alpha} - \alpha)^T \mathbf{V}^{-1} (\hat{\alpha} - \alpha) + 2\lambda^T \mathbf{g}(\alpha, \mathbf{p}) \quad (5.2)$$

The new parameters α , \mathbf{p} and λ that minimise this function are in general found using an iterative procedure. The initial estimates of both measured and unmeasured parameters are updated, at each iteration, by small corrections until some criteria of convergence are achieved. The criteria of convergence should ensure that a minimum in the function L is reached and that the constraints equations are satisfied. In this analysis, a kinematic fit is chosen to converge when $\Delta\chi^2/\chi^2 < 10^{-4}$, $\Delta(2\lambda^T \mathbf{g}) < 10^{-3}$ and $(2\lambda^T \mathbf{g})/\chi^2 < 10^{-2}$ where Δ represents the change in a given quantity between two iterations. The solution to this minimisation problem is described in Appendix B.

When the convergence criteria are satisfied, the function L reduces to the χ^2 value of the measured parameters. This χ^2 value is often used to test the goodness of the fit by quoting the probability that the physical process studied would lead to a χ^2 value worse (i.e. greater) than the one obtained. This probability is defined as

$$P = \int_{\chi^2}^{\infty} f(z, n) dz \quad (5.3)$$

where the function $f(z, n)$ is the χ^2 distribution with n degrees of freedom. The number of degrees of freedom in the type of problem studied here is given by the number of constraint equations minus the number of unmeasured parameters. The probabilistic interpretation of the χ^2 value is only valid if, as it is usually the case, the distribution of the residuals $(\hat{\alpha} - \alpha)$ does not deviate strongly from a Gaussian distribution. The data are usually deemed consistent with the fit assumptions when the probability is greater than approximately 6×10^{-5} or 6×10^{-7} (or equivalently 4 to 5 standard deviations for a Gaussian distribution).

The value of the cut on the probability distribution should be carefully chosen as to not bias the sample of selected events by preferentially rejecting events with a particular

kinematic configuration such as, for example, low momentum tracks. A linear plot of the probability distribution of a kinematic fit should be flat with a peak near zero corresponding to background physics processes. The uniformity of the probability distribution is an indicator that the input parameters of the fit are not biased and that their errors are correctly estimated. Reliable estimates of parameters are obtained using a kinematic fit only if the errors on the input quantities are realistic.

5.3 Inputs

In the context of particle interactions, the measured parameters taken as input to a kinematic fit generally consist of the energy and direction of each particle in the event. In addition, an estimate of the error on each measured parameter is needed to calculate the covariance matrix used in the fit. In this analysis, the correlations between the different measured quantities are small and hence neglected. As a consequence, the covariant matrix V is diagonal. The following sections describe in detail the specific input quantities used in the kinematic fits for each type of jet.

The measured centre-of-mass energy of each event is also treated as an input parameter of the fit. This is a unique feature of the fits performed in this analysis. The uncertainty on the centre-of-mass energy is taken to be the LEP centre-of-mass energy spread which is approximately 250 MeV [9]. The expected mass resolution of excited leptons is of the same order of magnitude as the spread in centre-of-mass energy. Thus this method ensures that results from a kinematic fit do not lead to mass resolutions better than what is experimentally achievable.

5.3.1 Photon Candidates

The energy of photon candidates is taken to be the energy contained in the jet deposited in the electromagnetic calorimeter. Since photons do not leave tracks in the central detector, the direction, expressed in terms of the polar (θ) and azimuthal (ϕ) angles, is given by the position of the observed electromagnetic energy cluster.

The resolutions and uncertainties of the energy and position of an electromagnetic cluster are measured using electron pair events, as described in Appendix C. Photons are expected to have similar properties to electrons. The energy resolution is typically 2 GeV for a 45 GeV photon and the angular resolution is approximately 4 mrad in θ and 3.5 mrad

in ϕ .

5.3.2 Electron Candidates

Electrons are similar to photons in that they deposit all their energy in the electromagnetic calorimeter. Therefore, the measured electromagnetic energy associated with an electron candidate provides a good estimate of the energy of that electron. As for photons, the uncertainty on the measured energy is about 2 GeV for a 45 GeV electron.

The direction of electron candidates is given by the polar and azimuthal angles of the reconstructed track in the central detector contained in the jet. Appendix C describes in detail a parameterisation of the angular resolution performed using events containing two back-to-back tracks. The uncertainties on the measured polar and azimuthal angles of a track are obtained from this parameterisation of the tracking detector resolution and are found to be approximately 2 mrad and 0.4 mrad respectively.

5.3.3 Muon Candidates

The parameters used as input to the kinematic fit are the momentum, polar and azimuthal angles of the track contained in jets identified as muons. The error on the track momentum as obtained by the OPAL track reconstruction fitting algorithm was found to be a good estimate of the tracking detector momentum resolution and is therefore used as input to the kinematic fit. For muon candidates selected in this analysis, the uncertainty on the track momentum is approximately 5 GeV for a 45 GeV muon. The uncertainties on the polar and azimuthal angles of tracks identified as muons are identical to the ones obtained for electron candidates.

5.3.4 Tau Candidates

The kinematic fit input parameters for tau jets do not depend on the specific type of tau decay. Input parameters for leptonically and hadronically decaying taus are calculated from the same kinematic variables.

The energy deposited in the detector is not representative of the actual tau energy due to the presence of undetected neutrinos produced when a tau particle decays. Thus, for kinematic fits performed on $\tau\tau\gamma$ and $\tau\tau\gamma\gamma$ events, the energy of the two jets assumed to

originate from tau leptons is treated as an unknown parameter. The jet energy is only used as an initial estimate of the tau energy.

Despite the production of neutrinos in tau decays, the axis of the observed decay products is in general a good estimate of the tau direction. This is especially true for high energy taus where the decay products are strongly boosted in the tau flight direction. The polar and azimuthal angles of a jet main axis are used as input to the kinematic fits. An estimate of the uncertainties on the polar and azimuthal angles due to the presence of additional undetected neutrinos as well as from the finite detector resolution are obtained from studies of tau pair events as described in Appendix C. It was determined that the direction of a tau is known to approximately 7 mrad in both polar and azimuthal angles.

5.4 General Constraints

Events selected by the criteria described in the previous chapter are required to satisfy energy and momentum conservation.

The three constraint equations requiring the total momentum of each event to be conserved can be mathematically written in terms of the kinematic fit input variables as

$$g_1 = \sum_{i=1}^n p_i \sin \theta_i \cos \phi_i = 0 \quad (5.4)$$

$$g_2 = \sum_{i=1}^n p_i \sin \theta_i \sin \phi_i = 0 \quad (5.5)$$

$$g_3 = \sum_{i=1}^n p_i \cos \theta_i = 0 \quad (5.6)$$

where the scalar momentum of a particle is related to its mass and energy through the relation $p = \sqrt{E^2 - m^2}$. The sum runs over the number of particles n considered in the event.

Conservation of energy is enforced by requiring events to satisfy the constraint equation

$$g_4 = \sum_{i=1}^n E_i - \sqrt{s} = 0 \quad (5.7)$$

where E_i are the energy of each particle in the event and \sqrt{s} represents the centre-of-mass energy of the e^+e^- collision which is treated as a fit parameter and thus allowed to vary within the measured spread in beam energy.

5.5 Kinematic Fits for Each Event Final States

The following sections describe the different kinematic fits applied to each type of event final state. Since the direction of the particles is in general more precisely known than their energy, the angles of the particles in an event usually determine whether a kinematic fit will or will not converge under a given set of constraints. In this analysis, events are judged consistent with an the physics process considered if the fit probability is greater than 0.001. The value 0.001 is chosen to retain a maximum number of events while rejecting the ones that are obviously incompatible with the final states of interest. Distributions of various fit probabilities are presented later.

5.5.1 Kinematic Fits for $\ell\ell\gamma\gamma$ Events

For pair produced excited lepton events, the reconstructed invariant mass of the two $\ell\gamma$ pairs originating from the decay of each excited lepton should be equal within the precision of the detector's measurements. Thus, in addition to the general constraints described above, $\ell\ell\gamma\gamma$ events are also required to satisfy

$$\begin{aligned}
 g_5 &= m_{\ell_1\gamma_1} - m_{\ell_2\gamma_2} \\
 &= \sqrt{(E_{\ell_1} + E_{\gamma_1})^2 - (\mathbf{p}_{\ell_1} + \mathbf{p}_{\gamma_1})^2} - \sqrt{(E_{\ell_2} + E_{\gamma_2})^2 - (\mathbf{p}_{\ell_2} + \mathbf{p}_{\gamma_2})^2} \quad (5.8) \\
 &= 0
 \end{aligned}$$

where the subscripts are used to identify each lepton and photon in the event. For each event, two kinematic fits are performed corresponding to the two possible $\ell\gamma$ pairings used to calculate the invariant masses. The constraint equation g_5 in the second fit performed is obtained by simply interchanging changing $\ell_1 \leftrightarrow \ell_2$.

In high energy e^+e^- collisions, initial state photon radiation is often produced, reducing the effective centre-of-mass energy of the collision. These photons are generally emitted nearly collinear to one of the beams, escaping detection. In order to account for this physical phenomenon, an additional kinematic fit, for each $\ell\gamma$ pairing, is performed assuming the presence of an undetected initial state photon along the beam axis. The momentum of the photon in the x and y direction is assumed to be zero while the z component (p_z) is treated as an unknown parameter of the fit. An initial estimate of p_z is calculated by enforcing conservation of momentum in the z direction. The angular region allowed for initial state photon is expressed in terms of the parameters δx and δy which represent small

distances away from the beam axis in the x and y direction as measured at the entrance of the endcap electromagnetic calorimeter. In the kinematic fit, the quantities δx and δy are treated as measured parameters with initial values of zero and variances given by the radius of the beam pipe.

For each selected $ll\gamma\gamma$ event, a total of four kinematic fits are therefore performed: one fit with and without assuming the presence of an initial state photon radiation for each two possible $l\gamma$ pairings. Only one fit per event is chosen. If every kinematic fit attempted fails to have a probability greater than 0.001, then the event is rejected. When more than one successful kinematic fit is obtained for an event, then the fits performed without the presence of an initial state photon radiation are first considered. The $l\gamma$ pairing giving the highest successful fit probability without the presence of an initial state photon is chosen regardless of the probability of the other fits. Otherwise, the $l\gamma$ pairing giving the highest probability assuming the presence of an initial state photon is chosen.

This algorithm for choosing the most appropriate kinematic fit is constructed to minimise distortions of the invariant mass distribution of signal events from a pure Gaussian. By construction, events for which a fit without an initial state photon converges, also successfully pass the corresponding fit assuming the presence of an additional photon down the beam pipe. In the second case, the initial state photon is simply assigned a small amount of energy. These types of events, however, do not contain a genuine initial state photon and the reconstructed invariant mass would be smaller than the actual invariant mass since some energy is assigned to the initial state photon. This effect is clearly shown in Figure 5.1. To obtain the best estimate of the actual invariant mass of each $l\gamma$ pairing, the fit without assuming the presence of an initial state photon is therefore favoured. Results from the fit with an additional photon along the beam axis are only chosen when other fits fail. This indicates that the event most likely contains a genuine initial state photon and that the reconstructed invariant mass represents the actual mass of the $l\gamma$ system.

Figure 5.2 shows the probability distributions of the chosen fit for $ee\gamma\gamma$, $\mu\mu\gamma\gamma$ and $\tau\tau\gamma\gamma$ events. Since no Standard Model processes consistently produce events with two identical $l\gamma$ invariant masses, only a very small fraction of $ll\gamma\gamma$ events have at least one successful fit. The requirement on the kinematic fit probability ($P > 0.001$) reduces the number of selected events by more than 70%. The expected mass resolution of excited lepton events depends on the mass of the excited lepton and on the centre-of-mass energy. Typical mass resolutions of 0.2 GeV, 0.2 GeV and 0.8 GeV are obtained for excited electrons, muons and taus, respectively. The use of kinematic fits improves the expected mass

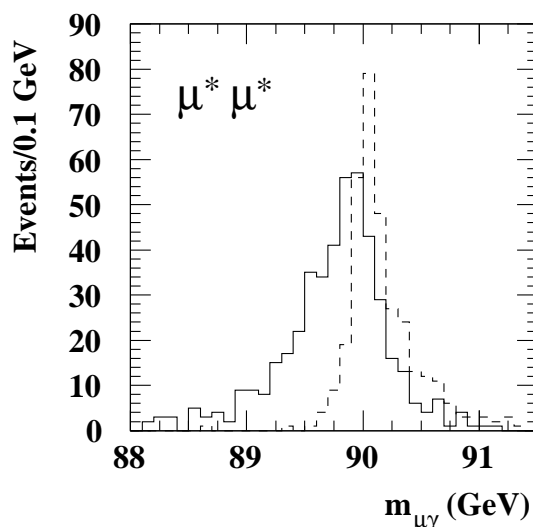


Figure 5.1: Example of reconstructed $\ell\gamma$ invariant mass of pair produced excited muons simulated with an arbitrarily chosen mass of 90 GeV. The solid (dashed) line shows the invariant mass obtained using results from the fit with (without) the presence of an initial state photon radiation. Only events for which both types of fit converge are shown here.

resolution of pair produced excited leptons by more than an order of magnitude.

5.5.2 Kinematic Fits for $\ell\ell\gamma$ Events

Events selected as candidates for the single production of excited leptons are only required to satisfy the general constraints of energy and momentum conservation. Following the same approach as outlined in the previous section, a total of two kinematic fits are performed for each $\ell\ell\gamma$ event. In the first case, only the two leptons and one photon are included in the fit. In the second case, the fit is performed assuming the presence of an initial state photon radiation along the beam axis. If both fits attempted fail to have a probability greater than 0.001, the event is rejected. If more than one fit successfully converges, the fit performed without the presence of an initial state photon is chosen given that the fit probability is greater than 0.001. Otherwise, results from the fit performed assuming the presence of an additional photon along the beam axis is used. The kinematic fit performed without assuming the presence of an initial state photon is favoured in order to reduce bias in the $\ell\gamma$ reconstructed invariant mass as shown in Figure 5.3.

Figure 5.4 shows the probability distributions of selected $\ell\ell\gamma$ events where the probability is taken to be that of the chosen fit on an event by event basis. The requirement on the fit probability reduces the number of selected events by about 10%. Approximately 30% of these events are selected assuming the presence of an initial state photon. Using results from the chosen fit, mass resolutions of approximately 0.35 GeV, 0.4 GeV and 1.8 GeV are obtained for excited electrons, muons and taus respectively, which amounts

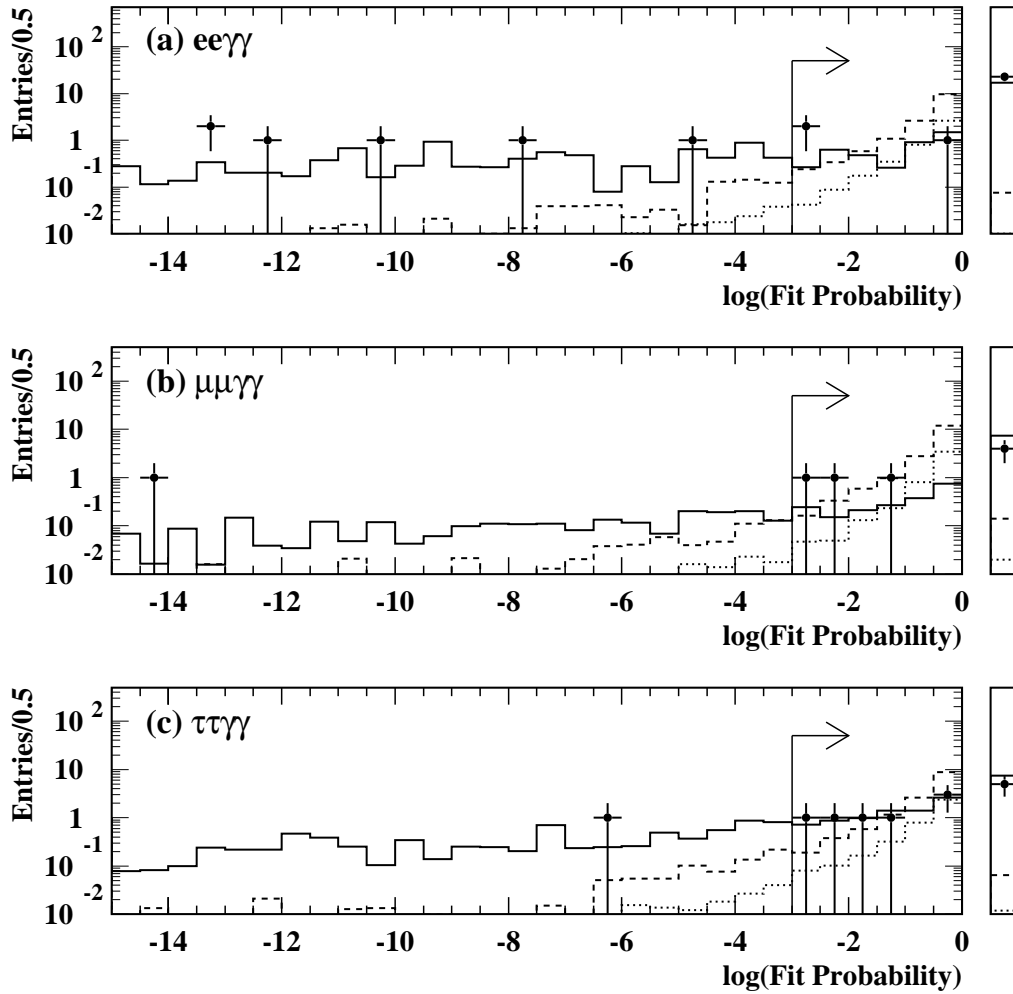


Figure 5.2: Probability distributions of the chosen kinematic fit for (a) $ee\gamma\gamma$, (b) $\mu\mu\gamma\gamma$ and (c) $\tau\tau\gamma\gamma$ events. The points are data and the solid lines show the total expected background from Standard Model processes. The right most bin of each histogram represents events for which all the fits attempted failed. The dashed and dotted lines are the distributions expected from pair produced excited leptons with masses of 40 GeV and 90 GeV respectively. The normalisations of the signal histograms are reduced by a factor of 0.01 in order to fit on the plots. The arrows indicate the accepted regions. The following distributions plotted as a linear function of the probability are flat with a sharp peak near zero as expected.

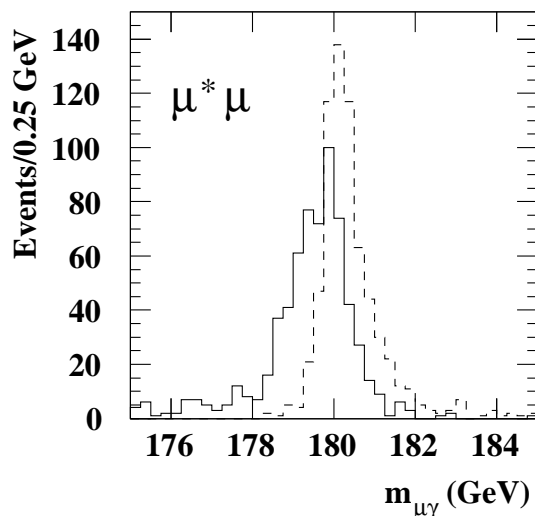


Figure 5.3: Example of reconstructed $\ell\gamma$ invariant mass of singly produced excited muons simulated with an arbitrarily chosen mass of 180 GeV. The solid (dashed) line shows the invariant mass obtained using results from the fit with (without) the presence of an initial state photon radiation. Only events for which both fits converge are shown.

to an improvement of more than an order of magnitude with respect to values obtained without a kinematic fit.

5.5.3 Kinematic Fit for $e\gamma$ Events

A single kinematic fit is performed on selected $e\gamma$ candidate events. In addition to energy and momentum conservation, the kinematic fit also requires the presence of an undetected electron along the beam axis. This electron is described in the fit by the parameters p_z , δx and δy , identical to the ones used to simulate the presence of an initial state photon radiation as described above. The only difference is that this additional particle, instead of being treated as massless, is given the mass of an electron. The fit probability distribution for $e\gamma$ candidates is shown in Figure 5.5. Events that fail to obtain a probability greater than 0.001 are rejected. The number of selected candidate events is reduced by approximately 10% as a result of the fit probability requirement. Mass resolutions between approximately 0.5 and 0.9 GeV are achieved using results from the fit. This constitutes an approximately five-fold improvement on the mass resolution obtained without the help of a kinematic fit.

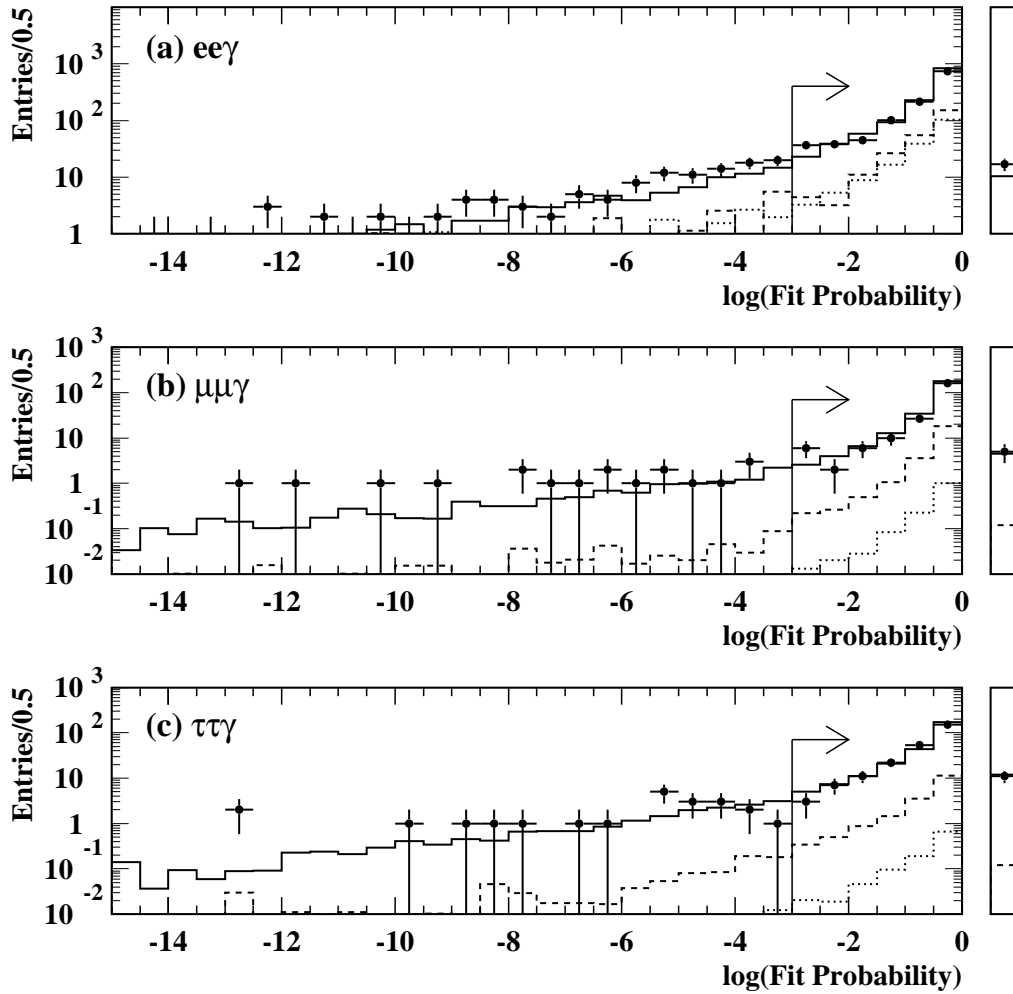


Figure 5.4: Probability distributions of the chosen kinematic fit for (a) $ee\gamma$, (b) $\mu\mu\gamma$ and (c) $\tau\tau\gamma$ events. The points are data and the solid lines show the total expected background from Standard Model processes. The last bin of each histogram on the right represents events for which all the fit attempted failed. The dashed and dotted lines are the distributions expected from singly produced excited leptons with masses of 90 GeV and 180 GeV respectively. The signal histograms are normalised to a ratio of the coupling constant to the compositeness scale (f/Λ) of 1 TeV^{-1} . The arrows indicate the accepted regions. The following distributions plotted as a linear function of probability are flat with a sharp peak near zero as expected.

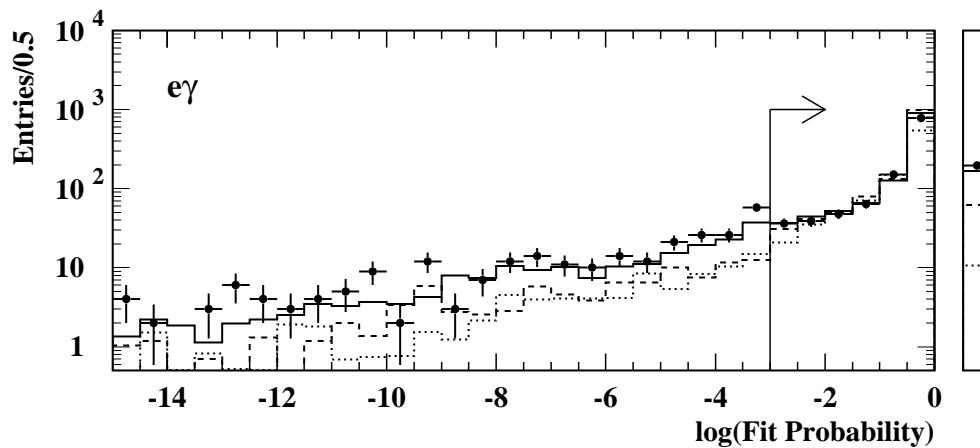


Figure 5.5: Probability distribution of the kinematic fit for $e\gamma$ events. The points are data and the solid line shows the total expected background from Standard Model processes. The last bin on the right represents events for which the fit did not converge. The dashed and dotted lines are the distributions expected from singly produced excited electrons with masses of 40 GeV and 90 GeV, respectively. The signal histograms are normalised to a ratio of the coupling constant over compositeness scale (f/Λ) of 1 TeV^{-1} . The following distribution plotted as a linear function of probability is flat with a sharp peak near zero as expected.

Results

The first section of this chapter summarises results obtained after applying the event selections and kinematic fits described in Chapter 4 and Chapter 5. The procedure used to interpret the results and calculate constraints on parameters of the excited lepton model are then described in detail. The last part of the chapter is devoted to a comparison of the limits calculated in this thesis to existing bounds obtained by other experiments.

6.1 Results

After applying the event selections and kinematic fits described in Chapter 4 and Chapter 5, the numbers of events observed in the data and the corresponding numbers of background events expected from Standard Model processes are presented in Tables 6.2 and 6.1. Both the statistical and systematic uncertainties on the background estimates are shown in those tables. A description of the various sources of systematic uncertainties investigated is presented in Section 6.3.3. The number of candidate events selected for each type of final state is compatible with expectations from the Standard Model.

Figures 6.1, 6.2 and 6.3 show the invariant mass distributions of selected $ll\gamma\gamma$, $ll\gamma$, and $e\gamma$ events obtained using results from the kinematic fits. In Figure 6.2, there are two entries per event corresponding to the two possible $l\gamma$ pairings. The presence of excited leptons would appear as an excess of events forming a peak in the reconstructed invariant mass distributions.

No evidence for excited leptons is found in either the single or pair production search. The results are therefore used to calculate constraints on parameters of the excited lepton model introduced in Chapter 2. Details pertinent to the limit calculation procedure are presented in the next sections.

$\langle\sqrt{s}\rangle$ (GeV)	$ee\gamma\gamma$		$\mu\mu\gamma\gamma$		$\tau\tau\gamma\gamma$	
	data	bkg	data	bkg	data	bkg
182.66	0	$0.2 \pm 0.1 \pm 0.1$	0	$0.3 \pm 0.0 \pm 0.1$	0	$1.0 \pm 0.2 \pm 0.8$
188.63	1	$1.8 \pm 0.4 \pm 0.6$	1	$0.5 \pm 0.1 \pm 0.2$	2	$2.2 \pm 0.3 \pm 1.7$
191.59	0	$0.4 \pm 0.1 \pm 0.1$	0	$0.1 \pm 0.0 \pm 0.0$	0	$0.3 \pm 0.1 \pm 0.3$
195.53	0	$0.2 \pm 0.1 \pm 0.1$	0	$0.1 \pm 0.0 \pm 0.1$	0	$0.9 \pm 0.1 \pm 0.7$
199.52	1	$0.6 \pm 0.2 \pm 0.2$	0	$0.2 \pm 0.1 \pm 0.1$	2	$0.9 \pm 0.2 \pm 0.7$
201.89	1	$0.2 \pm 0.2 \pm 0.1$	0	$0.1 \pm 0.0 \pm 0.1$	0	$0.4 \pm 0.1 \pm 0.4$
203.89	0	$0.0 \pm 0.0 \pm 0.0$	0	$0.0 \pm 0.0 \pm 0.0$	0	$0.0 \pm 0.0 \pm 0.0$
204.64	0	$0.1 \pm 0.0 \pm 0.0$	0	$0.0 \pm 0.0 \pm 0.0$	1	$0.1 \pm 0.0 \pm 0.1$
205.08	0	$0.4 \pm 0.2 \pm 0.1$	1	$0.1 \pm 0.0 \pm 0.0$	2	$0.6 \pm 0.1 \pm 0.5$
205.37	0	$0.0 \pm 0.0 \pm 0.0$	0	$0.0 \pm 0.0 \pm 0.0$	0	$0.0 \pm 0.0 \pm 0.0$
206.10	0	$0.0 \pm 0.0 \pm 0.0$	1	$0.1 \pm 0.0 \pm 0.0$	0	$0.2 \pm 0.0 \pm 0.1$
206.50	0	$0.1 \pm 0.1 \pm 0.0$	0	$0.4 \pm 0.1 \pm 0.2$	0	$1.2 \pm 0.3 \pm 0.9$
206.86	0	$0.0 \pm 0.0 \pm 0.0$	0	$0.0 \pm 0.0 \pm 0.0$	0	$0.1 \pm 0.0 \pm 0.0$
207.51	0	$0.0 \pm 0.0 \pm 0.0$	0	$0.0 \pm 0.0 \pm 0.0$	0	$0.0 \pm 0.0 \pm 0.0$
208.00	0	$0.1 \pm 0.0 \pm 0.0$	0	$0.0 \pm 0.0 \pm 0.0$	0	$0.1 \pm 0.0 \pm 0.1$
208.34	0	$0.0 \pm 0.0 \pm 0.0$	0	$0.0 \pm 0.0 \pm 0.0$	0	$0.0 \pm 0.0 \pm 0.0$
Total	3	$4.0 \pm 0.6 \pm 1.3$	3	$2.0 \pm 0.2 \pm 0.7$	7	$8.0 \pm 0.6 \pm 6.2$

Table 6.1: Observed numbers of events in the data and expected numbers of background (bkg) events in the different centre-of-mass energy bins considered for $ll\gamma\gamma$ event final states. The first column of the table indicates the luminosity weighted centre-of-mass energy of each bin. The first and second uncertainties on the expected numbers of background events represent the statistical and systematic contributions, respectively. The systematic uncertainties at each centre-of-mass energy are fully correlated. The statistical uncertainties are uncorrelated except for centre-of-mass energies greater than 202 GeV for which the same samples of simulated events are used for each two consecutive centre-of-mass energy bins. The background estimates and uncertainties are rounded off to the nearest decimal place.

$\langle\sqrt{s}\rangle$ (GeV)	$e\bar{e}\gamma$		$e\gamma$		$\mu\bar{\mu}\gamma$		$\tau\bar{\tau}\gamma$	
	data	bkg	data	bkg	data	bkg	data	bkg
182.66	127	$134 \pm 3 \pm 22$	149	$134 \pm 3 \pm 22$	32	$26 \pm 0 \pm 4$	27	$28 \pm 1 \pm 4$
188.63	368	$376 \pm 6 \pm 61$	322	$336 \pm 7 \pm 55$	66	$68 \pm 1 \pm 10$	72	$75 \pm 1 \pm 10$
191.59	47	$58 \pm 1 \pm 9$	48	$51 \pm 3 \pm 8$	15	$11 \pm 0 \pm 2$	5	$12 \pm 0 \pm 2$
195.53	116	$141 \pm 3 \pm 23$	104	$142 \pm 6 \pm 23$	20	$28 \pm 1 \pm 4$	26	$29 \pm 1 \pm 4$
199.52	140	$144 \pm 3 \pm 23$	128	$136 \pm 4 \pm 22$	19	$27 \pm 1 \pm 4$	28	$28 \pm 1 \pm 4$
201.89	66	$80 \pm 3 \pm 13$	64	$75 \pm 3 \pm 12$	8	$15 \pm 0 \pm 2$	16	$16 \pm 1 \pm 2$
203.89	5	$3 \pm 0 \pm 0$	1	$2 \pm 0 \pm 0$	0	$0 \pm 0 \pm 0$	1	$0 \pm 0 \pm 0$
204.64	12	$18 \pm 0 \pm 3$	13	$16 \pm 1 \pm 3$	0	$3 \pm 0 \pm 0$	5	$3 \pm 0 \pm 0$
205.08	92	$97 \pm 3 \pm 16$	84	$105 \pm 4 \pm 17$	18	$19 \pm 0 \pm 3$	24	$20 \pm 0 \pm 3$
205.37	5	$6 \pm 0 \pm 1$	4	$6 \pm 0 \pm 1$	0	$1 \pm 0 \pm 0$	3	$1 \pm 0 \pm 0$
206.10	22	$24 \pm 1 \pm 4$	24	$24 \pm 1 \pm 4$	3	$4 \pm 0 \pm 1$	3	$5 \pm 0 \pm 1$
206.50	153	$181 \pm 5 \pm 29$	162	$178 \pm 7 \pm 29$	25	$33 \pm 1 \pm 5$	32	$38 \pm 1 \pm 5$
206.86	5	$9 \pm 0 \pm 2$	8	$10 \pm 0 \pm 2$	0	$2 \pm 0 \pm 0$	2	$2 \pm 0 \pm 0$
207.51	0	$1 \pm 0 \pm 0$	0	$1 \pm 0 \pm 0$	0	$0 \pm 0 \pm 0$	0	$0 \pm 0 \pm 0$
208.00	13	$12 \pm 0 \pm 2$	11	$12 \pm 0 \pm 2$	5	$2 \pm 0 \pm 0$	4	$2 \pm 0 \pm 0$
208.34	1	$1 \pm 0 \pm 0$	1	$1 \pm 0 \pm 0$	1	$0 \pm 0 \pm 0$	0	$0 \pm 0 \pm 0$
Total	1172	$1283 \pm 11 \pm 208$	1123	$1229 \pm 14 \pm 203$	212	$239 \pm 2 \pm 35$	248	$260 \pm 2 \pm 35$

Table 6.2: Observed numbers of events in the data and expected numbers of background (bkg) events at different luminosity weighted centre-of-mass energies ($\langle\sqrt{s}\rangle$) for $l\bar{l}\gamma$ and $e\gamma$ event final states. The first and second uncertainties on the expected numbers of background events represent the statistical and systematic contributions, respectively. The systematic uncertainties at each centre-of-mass energy are fully correlated. The statistical uncertainties are uncorrelated except for centre-of-mass energies greater than 202 GeV for which the same samples of simulated events are used for each two consecutive centre-of-mass energy bins. The background estimates and uncertainties are rounded off to the nearest integer value.

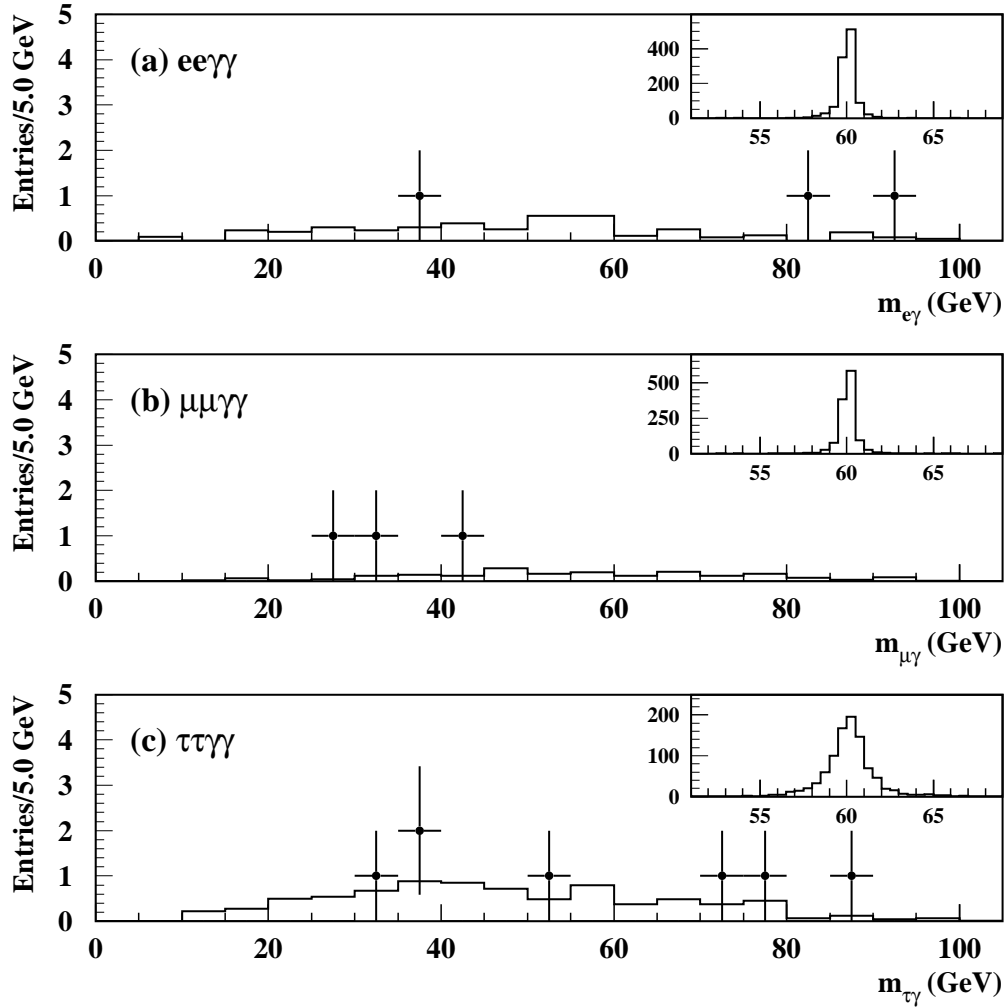


Figure 6.1: Reconstructed $l\gamma$ invariant mass distributions for selected (a) $ee\gamma\gamma$, (b) $\mu\mu\gamma\gamma$ and (c) $\tau\tau\gamma\gamma$ events. The points are data and the solid lines show the total expected background from Standard Model processes. Example distributions of excited lepton events with arbitrarily chosen mass of 60 GeV are shown in the insets. The signal histograms are normalised to the data luminosity and plotted in bins of 0.5 GeV.

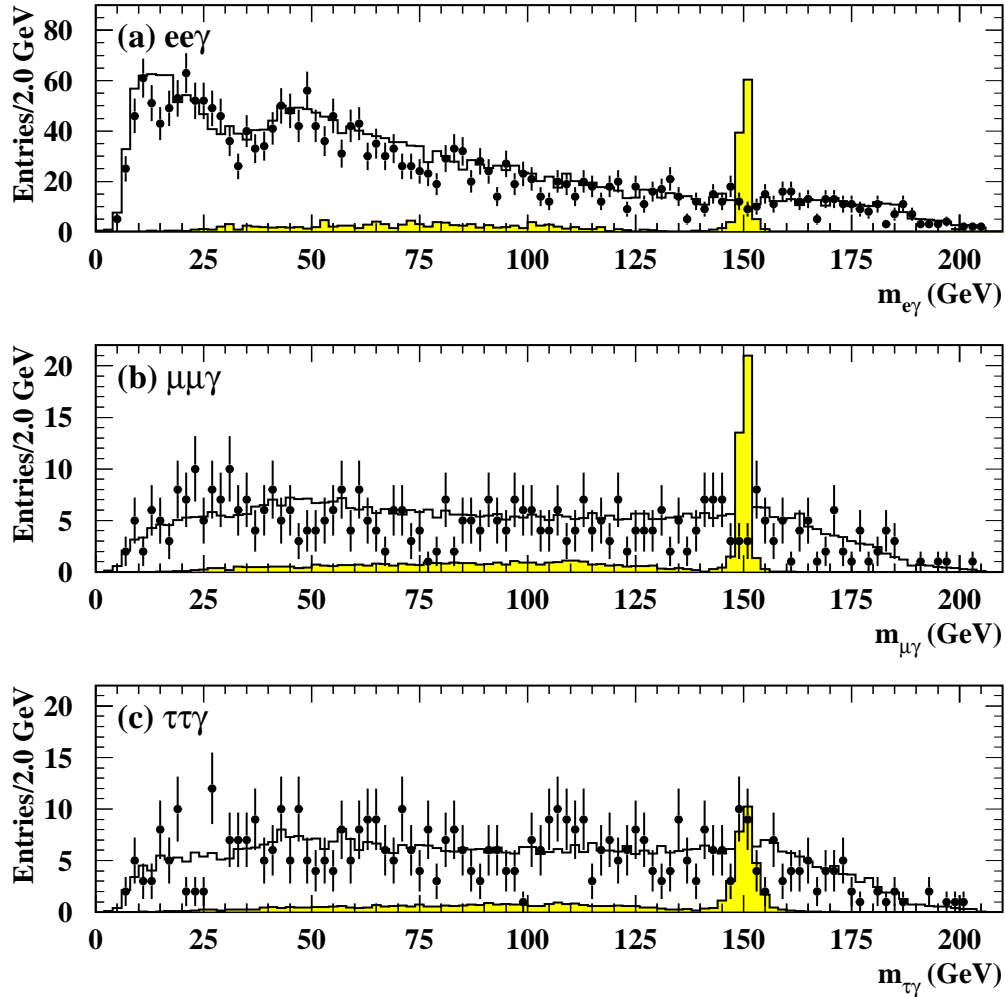


Figure 6.2: Reconstructed $l\gamma$ invariant mass distributions for selected (a) $ee\gamma$, (b) $\mu\mu\gamma$ and (c) $\tau\tau\gamma$ events. The points are data and the solid lines show the total expected background from Standard Model processes. The shaded histograms represent excited lepton signal events with arbitrarily chosen mass of 150 GeV and normalised to a coupling over compositeness scale of (a) 0.7 TeV^{-1} and (b,c) 2 TeV^{-1} . There are two entries per event corresponding to the two possible $l\gamma$ pairings.

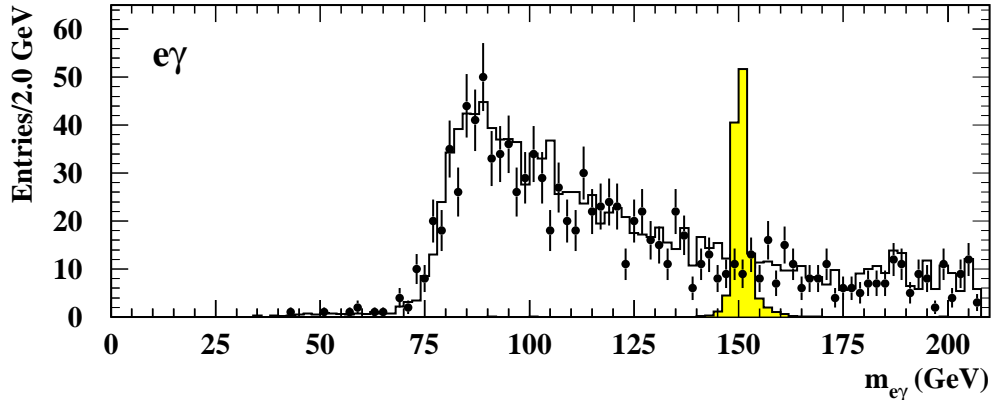


Figure 6.3: Reconstructed $l\gamma$ invariant mass distribution for selected $e\gamma$ events. The points are data and the solid line shows the total expected background from Standard Model processes. The shaded histogram represents excited electron signal events with arbitrarily chosen mass of 150 GeV and normalised to a coupling over compositeness scale of 0.3 TeV^{-1} .

6.2 Hypothesis Testing

The general goal of a search is either to discover or exclude the existence of a signal with as high a level of certainty as possible. This is usually achieved by testing the degree to which the observed data are compatible with the existence of both signal and background as compared to only background. The general procedure of hypotheses testing can be summarised as follow. The first step consists of choosing observables in the experiment sensitive to both hypotheses. A test statistic (or estimator) is then constructed, using these observables, to discriminate between the two hypotheses. Finally, a criterion of acceptance or rejection of the signal must be defined in order to make a statement about the compatibility of the data with respect to the two different hypotheses. Results are usually expressed in terms of the significance of the observed discovery or exclusion.

6.2.1 The Likelihood Ratio

The goal of a search is to distinguish, given a set of data, between two hypotheses: the ‘background-only’ hypothesis (H_0) and the ‘signal plus background’ hypothesis (H_1). A good test statistic is called the likelihood ratio [42–45]. This fact is a consequence of

the Neyman-Pearson lemma originally presented in [46] but also described in various textbooks such as [43–45]. The likelihood ratio simultaneously maximises the probability of rejecting a false hypothesis and maximises the probability of choosing a true hypothesis. For a given experimental result \mathbf{x} , the likelihood ratio ($Q(\mathbf{x})$) is defined as the ratio of the probability density functions of the two hypotheses being tested,

$$Q(\mathbf{x}) = \frac{\mathcal{L}(\mathbf{x}; H_0)}{\mathcal{L}(\mathbf{x}; H_1)} . \quad (6.1)$$

The simplest experimental observable is the number of events n satisfying a certain set of criteria. Given an estimated number of background events, b , and signal events, s , the likelihood ratio is simply a ratio of Poisson probability density functions,

$$Q(n) = \frac{e^{-(s+b)} (s+b)^n}{n!} \bigg/ \frac{e^{-b} b^n}{n!} . \quad (6.2)$$

For the purpose of calculating confidence levels, this test statistic has the desirable property of being monotonically increasing with the number of observed candidates n .

The likelihood ratio can also be calculated in terms of other discriminating observables. In general, it however results in a more complicated expression for which both the signal and background probability distribution functions of the discriminating variable must be known. The task of calculating a likelihood ratio using one or more discriminating observables measured for each event is equivalent to combining the likelihood ratios obtained in each bin of a histogram of these observables. Each bin is treated as a separate search channel for which the likelihood ratio is calculated according to Equation 6.2. The estimator of a set of N independent channels is simply the product of the individual likelihood ratio ($Q_i(n_i)$) for each search channel,

$$Q(\mathbf{n}) = \prod_{i=1}^N Q_i(n_i) = \prod_{i=1}^N \frac{e^{-(s_i+b_i)} (s_i+b_i)^{n_i}}{n_i!} \bigg/ \frac{e^{-b_i} b_i^{n_i}}{n_i!} \quad (6.3)$$

or equivalently,

$$\ln Q(\mathbf{n}) = -s_{\text{tot}} + \sum_{i=1}^N n_i \left\{ \ln \left(1 + \frac{s_i}{b_i} \right) \right\} \quad (6.4)$$

where s_{tot} is the sum of the number of signal events, $s_{\text{tot}} = \sum_{i=1}^N s_i$. The combination of different experiments, event final states or centre-of-mass energies therefore reduces to a sum of event weights and is thus simple and unambiguous.

The likelihood ratio based on the number of observed and expected events is the test statistic chosen in this thesis to discriminate between the signal plus background and background-only hypotheses. In order to maximise the sensitivity of the search, events are binned as a function of reconstructed invariant mass. The existence of excited leptons is expected to distort the invariant mass distribution of observed events in a unique way. To calculate the total likelihood ratio using Equation 6.4, three essential ingredients are required in each bin of reconstructed invariant mass: the number of observed data, expected background and expected signal events.

6.3 Background and Signal Expectations

This section describes the methods used to obtain an estimate of the background and signal invariant mass distributions. The systematic uncertainties associated with the background expectations and signal efficiencies are also presented.

6.3.1 Background Expectation

Although relatively large samples of simulated events are used to estimate the background for each event final state, once finely binned in terms of the reconstructed $\ell\gamma$ invariant mass, the number of background events in each individual channel is small and is therefore sensitive to statistical fluctuations. This is particularly true for $\ell\ell\gamma\gamma$ final states where only a very small number of events are selected. Some channels are found to contain no background events when in fact the probability of obtaining background events is non-zero. This is a problematic situation that needs to be addressed since the likelihood ratio of Equation 6.2, although a powerful estimator, is undefined for channels where the background expectation is zero. To reduce the sensitivity of the results to statistical fluctuations in the background expectations, background distributions of the reconstructed $\ell\gamma$ mass are ‘smoothed’ using an algorithm [47] that parameterises the shape of a distribution. Figures 6.4 and 6.5 show an example of the expected $\ell\gamma$ mass distribution at a centre-of-mass energy of 189 GeV for each final state considered along with results from the shape parameterisation. The functions obtained using this smoothing algorithm are a good approximation of the background expectation. Sharp changes in a distribution are difficult to parameterise, as seen in Figure 6.5. The discrepancy in the small region at the kinematic limit will result in slightly more conservative constraints than the given confidence level

stated, as background in that region is underestimated. The expected number of background events in each individual channel is taken from the shape parameterisation of the background distributions.

6.3.2 Signal Expectation

Different methods exist for obtaining $\ell\gamma$ mass distributions of signal events for arbitrary excited lepton mass. The ‘brute force’ scenario consists of generating Monte Carlo signal event samples at every mass for which one wishes to calculate limits. However, the large number of possible excited lepton masses and centre-of-mass energies for which event samples would have to be generated makes it impossible in practice to use this approach. Another solution consists of generating events at a few distinct excited lepton masses and centre-of-mass energies, and then interpolating the mass distributions between these points to obtain an approximation of the distributions at any arbitrary excited lepton mass and centre-of-mass energies. Although done in practice to calculate limits from some searches [48], the interpolation of histograms is in general very complicated and not entirely reliable, especially if only a limited number of event samples are available.

Instead, the invariant mass distribution of excited leptons is approximated by a Gaussian distribution centered at the excited lepton mass and with a variance equal to the expected mass resolution. The Gaussian distribution is normalised to the number of signal events expected at a given centre-of-mass energy.

Both the expected signal efficiency (ϵ) and mass resolution vary as function of the mass of the excited leptons and the centre-of-mass energy of the e^+e^- collisions. In order to test the compatibility of the data with the existence of excited leptons of different masses, the selection efficiencies and mass resolution must be calculable for arbitrary values of mass and centre-of-mass energy. For each event final state considered, the selection efficiency and mass resolution are parameterised as a function of the excited lepton mass scaled by the centre-of-mass energy (m_{ℓ^*}/\sqrt{s}). The results of this parameterisation can be found in Appendix D.

Typical mass resolutions for each final state were given in Chapter 5. Selection efficiencies for the pair production of excited leptons vary from about 35% to 55%. The efficiency for the single production of excited muons is 70% and approximately constant over the entire kinematically allowed range of masses. Near the kinematic limit for the single production of excited taus, the efficiency rapidly drops from 53% down to approx-

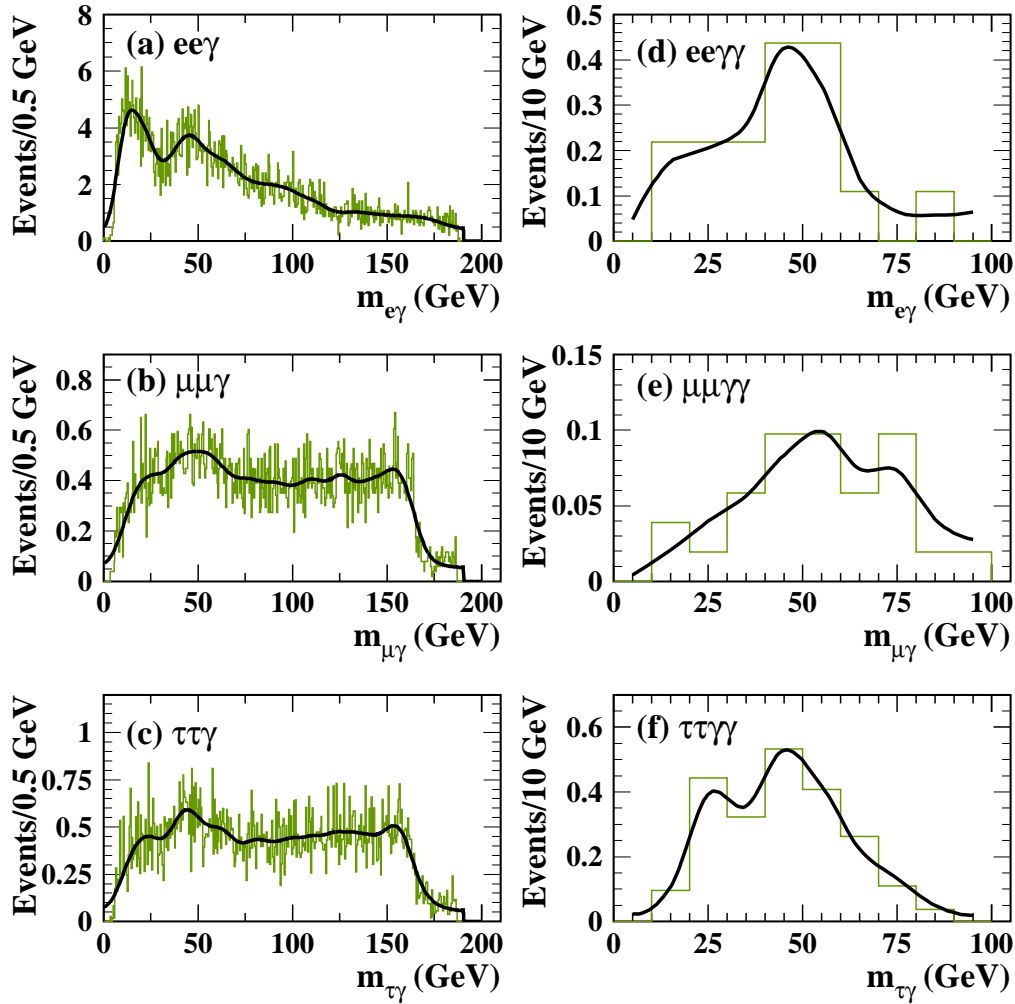


Figure 6.4: Reconstructed $l\gamma$ mass distributions of Standard Model background events obtained at a centre-of-mass energy of 189 GeV for (a-c) $ll\gamma$ and (d-f) $ll\gamma\gamma$ event final states. The solid lines show the shape parameterisation used in the limit calculations. Distributions are normalised to the data luminosity.

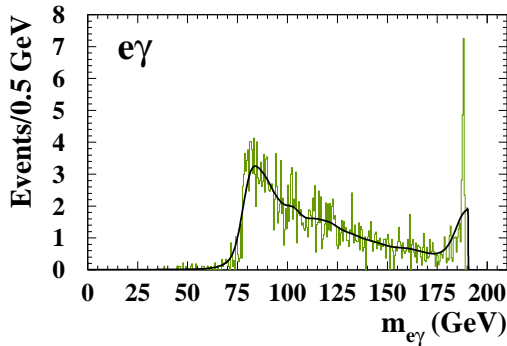


Figure 6.5: Reconstructed $l\gamma$ mass distribution of Standard Model background events obtained at a centre-of-mass energy of 189 GeV for $e\gamma$ event final state. The solid line shows the shape parameterisation used in the limit calculation. The distribution is normalised to the data luminosity.

imately 20% since the recoiling tau has low energy and thus often fails the initial set of selection criteria. For singly produced excited electrons, the efficiencies of the $ee\gamma$ and $e\gamma$ selections depend strongly on the mixture of s -channel and t -channel components. The sum of the $ee\gamma$ and $e\gamma$ efficiencies lies in general between 50% and 70%.

Efficiency correction factors (f_c) were also calculated to take into account deviations of the signal invariant mass from a purely Gaussian shape. These correction factors are defined as the ratio of the area under the best Gaussian fit, expressed in number of events, to the total number of selected signal events. As shown in Appendix D, these correction factors were found to be independent of the excited lepton mass and centre-of-mass energy, and vary between approximately 0.7 and 0.85 depending on the event final state.

6.3.3 Systematic Uncertainties

The credibility of the results relies on a proper estimate of possible systematic effects affecting the analysis. These effects are incorporated in the limit calculation procedure using a Monte Carlo method described in the next section. This section contains details of the various sources of systematic effects on the signal efficiencies and background estimates that were investigated. These are described in order of importance.

Radiative Corrections Modelling

Uncertainties in the modelling of initial and final state photon radiation in di-lepton events affect the background estimates. These uncertainties are assessed by comparing background expectations obtained using the KORALZ and KK2F event generators for the processes $e^+e^- \rightarrow \mu^+\mu^-$ and $e^+e^- \rightarrow \tau^+\tau^-$. The Monte Carlo program KK2F, used in this

analysis to estimate the background contributions from $\mu^+\mu^-$ and $\tau^+\tau^-$ events, has the most complete description of photon radiation, including second-order subleading corrections and the exact matrix elements for the emission of two hard photons [49]. The relative variations in background expectations between the two event generators are assigned as systematic uncertainties representing the effect of missing higher orders. These are found to be 11% for final states compatible with the single production of excited muons and taus, and 7% for $\mu\mu\gamma\gamma$ and $\tau\tau\gamma\gamma$ events. The BHWIDE and TEEGG event generators, used to simulate the background from radiative e^+e^- events, have a precision for radiative corrections similar to the KORALZ program. The background estimates for events expected from the production of excited electrons are thus assigned an uncertainty of 7% for the $ee\gamma\gamma$ final state and 11% for both $ee\gamma$ and $e\gamma$ events.

Efficiency and resolution interpolation

The systematic uncertainties associated with the interpolation of the signal efficiencies and mass resolutions were estimated by calculating the root-mean-square spread between simulated signal event samples and the parameterisation functions. These relative uncertainties range between 3% and 23%.

Error Estimates of Kinematic Fit Input Variables

Uncertainties on the error estimates of the kinematic fit input variables are evaluated by varying the error on each variable independently and performing the kinematic fits again. The errors are varied by an amount representing one standard deviation as calculated from the uncertainties on the error parameterisations described in Appendix C. Background estimates for final states containing two leptons and two photons are particularly sensitive to changes in the errors due to the additional constraint in the kinematic fit requiring events to have equal reconstructed $\ell\gamma$ invariant masses. Also, the smaller sample of tau pair events used to parameterise the errors on the tau direction results in larger statistical uncertainties on the error parameterisation which in turn dictate the larger variations used to estimate the systematic error contributions. Relative changes in the background estimates and signal efficiencies obtained from each error variation are added in quadrature. The total systematic uncertainties associated with the error parameterisation and assigned to each final state are summarised in Tables 6.4 and 6.3.

Jet Classification

Systematic effects associated with the jet classification were investigated by studying the modelling of the lepton and photon identification efficiencies. Using di-lepton and di-photon events recorded at centre-of-mass energies equal to and greater than the Z^0 mass, the systematic uncertainty associated with each set of lepton and photon requirements was evaluated by comparing the identification efficiencies obtained from data and simulated events. Relative errors of 1% for electron and muon, and 2% for the tau and photon classifications were assigned. Systematic uncertainties associated with each final state were determined by adding linearly contributions from identical jet classifications and adding in quadrature contributions from different types of leptons and photons. The resulting uncertainties on the signal efficiencies, shown in Table 6.3, are fully correlated with the corresponding errors on the background estimates presented in Table 6.4.

Energy and angular resolution

The systematic uncertainty associated with the energy scale, energy resolution and angular resolution of the leptons and photons was evaluated by modifying each parameter independently in Monte Carlo simulated events. Given the well defined kinematic characteristics of non-radiative di-lepton events, comparisons between data and simulated distributions of di-lepton events recorded at different centre-of-mass energies were used to determine the size of these variations.

An estimate of the shifts in the energy (momentum) scale of each particle type was obtained by plotting the difference between the measured energy (momentum) and the beam energy. Variations in the background estimates and signal efficiencies associated with a shift of 0.3% in the energy (momentum) of electron and photon (muon) candidates were assigned as systematic uncertainties. These were found to be negligible.

For different smearing values, a maximum likelihood technique was used to calculate the degree to which distributions of the energy and measured angles of each type of particle were compatible with data. The energy and angular resolutions of jets were smeared by the maximum values for which simulated events were compatible with the distributions of data within one standard deviation. The measured energy of electrons and photons was smeared by 0.15 GeV while the momentum of muons was smeared by 1 GeV. The measured polar and azimuthal angles was smeared by an amount varying between 1 mrad and 10 mrad depending on the particle type. Systematic uncertainties were assigned to be

Source	Uncertainty (%)						
	$ee\gamma$	$e\gamma$	$\mu\mu\gamma$	$\tau\tau\gamma$	$ee\gamma\gamma$	$\mu\mu\gamma\gamma$	$\tau\tau\gamma\gamma$
Resolution interpolation	14.8	12.0	20.6	6.5	22.1	22.5	13.4
Efficiency interpolation	8.5	3.0	2.4	7.6	4.6	3.5	3.0
Error estimate of fit variables	5.0	5.0	3.0	5.0	3.0	2.0	6.0
Jet classification	2.8	2.2	1.4	4.5	4.5	4.5	5.7
Energy and angular resolution	0.9	1.1	0.8	1.1	1.8	0.6	0.9
Modelling of selection variables	0.0	1.5	0.1	1.6	0.4	0.4	0.8
Total	18.0	13.6	21.0	12.2	23.3	23.3	16.1

Table 6.3: Relative systematic uncertainties on the signal efficiencies for each final state considered.

the relative changes in background estimates and signal efficiencies.

Contributions to the systematic uncertainty of each final state from individual changes in the energy scale, energy resolution and angular resolution are added in quadrature.

Selection Variable modelling

The systematic uncertainty due to modelling of the event selection variables was estimated by varying each selection cut independently and measuring the corresponding changes in the overall signal efficiencies and background estimates. The difference between the mean value of the data and background expectation for each selection variable determined the range of variation of each cut. Systematic uncertainties varying between 0.5% and 6.3% are assigned to the different background estimates. Contributions to the systematic error on the signal efficiencies are shown in Table 6.3.

Summaries of the systematic effects on the background expectations and signal efficiencies are presented in Tables 6.4 and 6.3, respectively. The uncertainty on the integrated luminosity measurements (0.2%) is considerably smaller than the systematic effects already described and is therefore neglected.

6.4 Limit Calculations

Given that no evidence for excited states of leptons was found, constraints on the production rate of excited charged leptons as function of mass are calculated. Selected candidate events from each final state and at each centre-of-mass energy are binned in terms of their

Source	Uncertainty (Number of events)						
	$ee\gamma$	$e\gamma$	$\mu\mu\gamma$	$\tau\tau\gamma$	$ee\gamma\gamma$	$\mu\mu\gamma\gamma$	$\tau\tau\gamma\gamma$
Radiative corrections	141	135	26	29	0.3	0.1	0.6
Error estimate of fit variables	68	57	10	24	1.1	0.6	6.2
Jet classification	36	27	3	12	0.2	0.1	0.5
Energy and angular resolution	9	16	2	2	0.0	0.3	0.6
Modelling of selection variables	6	54	2	8	0.3	0.1	0.3
Total	161	159	28	40	1.2	0.7	6.3

Table 6.4: Systematic uncertainties on the background estimates for each event final state, expressed in number of events.

reconstructed $\ell\gamma$ invariant mass with each bin being treated as an individual search channel. Invariant mass distributions of background and signal events are obtained using the methods described in the previous section. Given the number of observed data, expected background and signal events in each search channel, a value of the likelihood ratio can be calculated. This value of the likelihood ratio is then used to exclude the existence of a signal at a chosen confidence level using the Modified Frequentist approach described in Appendix E. The degree of compatibility of the data with the signal hypothesis is expressed in terms of the maximum number of signal events produced in the entire data set at the 95% confidence level (N_{95}).

Details pertinent to the limit calculation procedure are given in the next paragraph. The method employed to account for the systematic uncertainties presented in the previous section is then described. Values of N_{95} obtained as function of excited lepton masses are interpreted as limits on the product of the cross-section and branching fraction of excited charged leptons. These limits are in turn used to set constraints on parameters of the phenomenological model described in Chapter 2.

As candidate events are binned according to their value of reconstructed invariant mass, the size of each bin should ideally be at least of the same order as the mass resolution. Unfortunately, the computer time required to performed the limit calculations grows approximately exponentially with the number of search channels. Thus, as a compromise between the mass resolution achieved in this analysis and the large amount of time required to perform the calculations, a bin width of 500 MeV was chosen for each final state considered. The number of individual search channels doubles for limits on the single production of excited electron where two different final states ($ee\gamma$ and $e\gamma$) are combined.

6.4.1 Treatment of Systematic Uncertainties

Statistical and systematic uncertainties on the signal efficiencies and background expectations described in Section 6.3.3 are incorporated in the limit calculation by fluctuating, over many iterations, the background expectation and signal efficiency according to their respective uncertainties. The final limits are determined from the average of all the N_{95} values obtained at each iteration.

In calculating the expected signal distributions at each iteration, the mass resolution defining the widths of the Gaussian distributions is fluctuated by an amount corresponding to the interpolation uncertainty, independently of the other sources of errors associated directly with the signal efficiency. Uncertainties on the signal efficiency, mass resolution and background estimates are treated as being fully correlated between centre-of-mass energy. The systematic uncertainties on the signal efficiencies due to the jet classification are also fully correlated with the corresponding errors on the background estimates and are treated as such in the limit calculations. The effects of systematic uncertainties on exclusion limits have been shown to be small even for uncertainties of the order of 20% [50].

6.4.2 Limits on Excited Lepton Production Rate

Values of N_{95} obtained as function of excited lepton mass are used to calculate limits on the product of the excited lepton cross-section at $\sqrt{s} = 208.3$ GeV and electromagnetic branching fraction ($\sigma \times \text{BR}^{(2)}$) assuming the cross-section evolution as a function of centre-of-mass energy expected for excited leptons¹. The upper limits on the number of signal events produced in the data summed over all centre-of-mass energy can be expressed as

$$\begin{aligned} N_{95} &= \sum_{i=1}^{16} \sigma_i \cdot \text{BR}^{(2)} \cdot \mathcal{L}_i \cdot \epsilon_i \cdot f_c \\ &= \sigma_{16} \times \text{BR}^{(2)} \sum_{i=1}^{16} \frac{\sigma_i}{\sigma_{16}} \cdot \mathcal{L}_i \cdot \epsilon_i \cdot f_c \end{aligned} \quad (6.5)$$

where the sum runs over all the centre-of-mass energies considered and the symbols \mathcal{L} , ϵ , f_c , σ and BR represent the integrated luminosity, efficiency, efficiency correction factor, cross-section and electromagnetic branching fraction of excited leptons, respectively. The symbol σ_{16} represents the excited lepton cross-section expected at $\sqrt{s} = 208.3$ GeV. Limits

¹For final states consistent with the pair production of excited leptons, limits are calculated for the quantity $\sigma \times \text{BR}^2$ while for single production searches, constraints are obtained for the quantity $\sigma \times \text{BR}$.

on the product of the excited lepton cross-section at $\sqrt{s} = 208.3$ GeV and electromagnetic branching fraction ($\sigma \times \text{BR}^{(2)}$) are therefore obtained using

$$\sigma \times \text{BR}^{(2)} = \frac{N_{95}}{\sum_{i=1}^{16} \frac{\sigma_i}{\sigma} \cdot \mathcal{L}_i \cdot \epsilon_i \cdot f_c} \quad (6.6)$$

where the subscript on the cross-section at $\sqrt{s} = 208.3$ GeV is dropped for simplicity.

The upper limits on the single production of excited muons and tau leptons do not depend on the model dependent coupling parameters f and f' . The excited electron selection efficiencies for $ee\gamma$ and $e\gamma$ event final states, however, depend on the relative magnitude of the s -channel and t -channel production diagrams and therefore depend on the value of the parameters f and f' . For comparison with previously published results, the limits on excited electrons presented here assume $f = f'$. Figures 6.6(a,b) show the 95% confidence level upper limits on the product of the cross-section at $\sqrt{s} = 208.3$ GeV and the electromagnetic branching fraction obtained from the search for singly and pair produced excited leptons.

6.4.3 Mass Limits

Limits on the product of the cross-section and branching fraction are used to set constraints on parameters of the phenomenological model described in Chapter 2. Lower mass limits on excited leptons are calculated using results from the pair production searches. The theoretical calculation [6] of the product of the pair production cross-section at $\sqrt{s} = 208.3$ GeV and the branching fraction squared is overlaid on Figure 6.6(b). As part of this calculation, the electromagnetic branching fraction is calculated assuming $f = f'$. The 95% confidence level lower mass limits on excited leptons correspond to the mass at which the cross-section times branching fraction limit curves cross the theoretical expectation. Lower mass limits of $m_{e^*} > 103.2$ GeV, $m_{\mu^*} > 103.2$ GeV and $m_{\tau^*} > 103.2$ GeV are obtained at the 95% confidence level. Although systematic errors are incorporated into the limit calculations, an additional uncertainty on the mass limits arises from the finite width of the centre-of-mass energy bins considered. The 0.5 GeV centre-of-mass energy bin width near the kinematic limit corresponds to an uncertainty of 0.1 GeV on the mass limits.

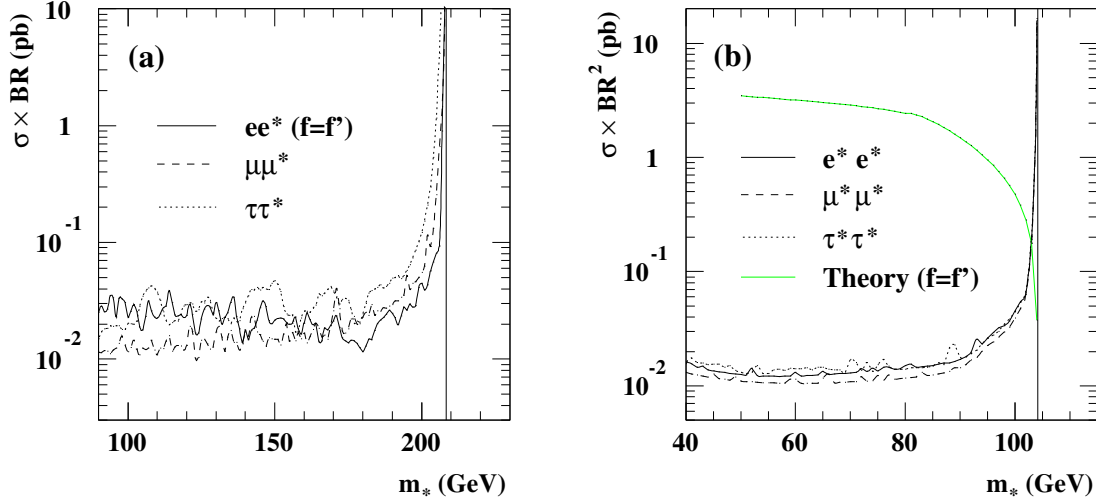


Figure 6.6: The 95% confidence level upper limits on the product of the cross-section at $\sqrt{s} = 208.3$ GeV and the branching fraction for (a) single and (b) pair production of excited leptons as a function of mass (m_*). The limit obtained for the single production of excited electrons is calculated assuming $f = f'$. The regions above the curves are excluded. The product of the theoretical cross-section at $\sqrt{s} = 208.3$ GeV and the electromagnetic branching fraction squared assuming $f = f'$ is also shown in (b).

6.4.4 Limits on f/Λ

Limits on the product of the cross-section and the branching fraction of singly produced excited leptons are used to constrain values of the ratio of the coupling to the compositeness scale, f/Λ . Since the cross-section for the single production of excited leptons is proportional to $(f/\Lambda)^2$, limits on the ratio of the coupling to the compositeness scale as a function of excited lepton mass are calculated using

$$\left[\frac{(f/\Lambda)}{(1 \text{ TeV}^{-1})} \right]_{95\% \text{CL}} = \sqrt{\frac{N_{95}}{N_{\text{exp}}}} \quad , \quad (6.7)$$

where N_{exp} is the number of expected signal events assuming $f/\Lambda = 1 \text{ TeV}^{-1}$ and obtained using

$$N_{\text{exp}} = \sum_{i=1}^{16} \sigma_i \cdot \text{BR} \cdot \mathcal{L}_i \cdot \epsilon_i \cdot f_c \quad . \quad (6.8)$$

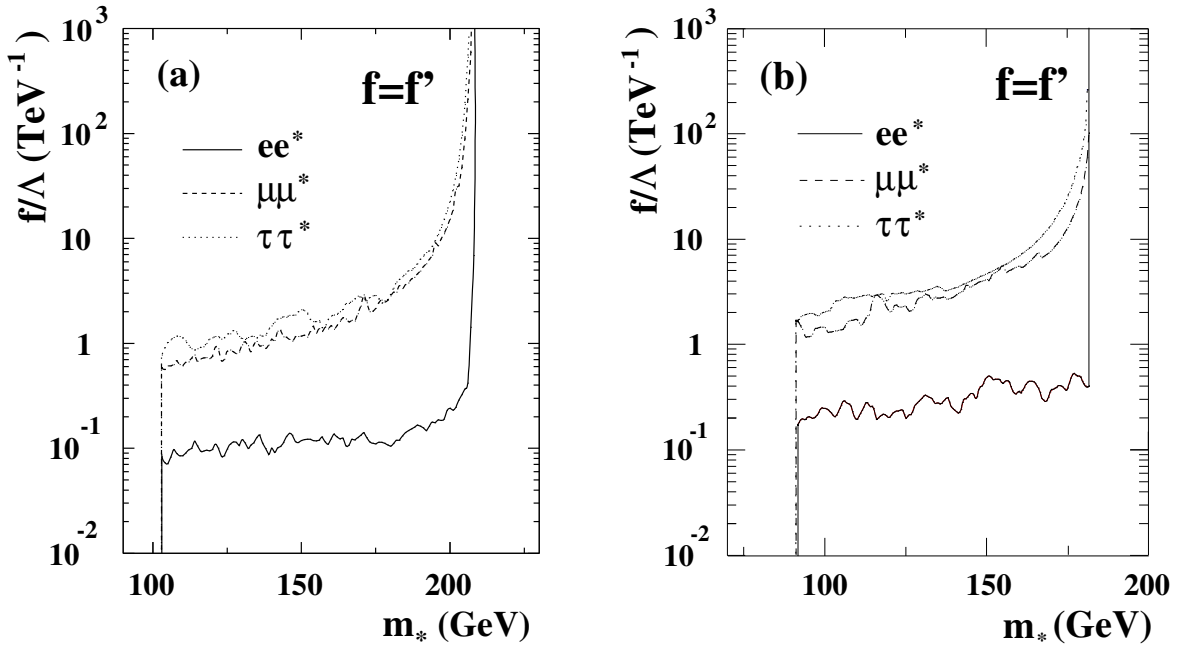


Figure 6.7: The 95% confidence level upper limits on the ratio of the excited lepton coupling constant to the compositeness scale, f/Λ , as a function of the excited lepton mass and assuming $f = f'$. Figure (a) shows the limits obtained as part of the work presented in this thesis and Figure (b), the previous OPAL limits [51]. The regions above the curves are excluded by single production searches. In Figure (a), pair production searches exclude masses below 103.2 GeV for excited electrons, muons and taus. In Figure (b), masses below 91.3 GeV for excited electrons and muons, and 91.2 GeV for excited taus are excluded.

Upper limits on f/Λ are calculated for the coupling assignment $f = f'$. Figure 6.7(a) shows these limits for each type of excited lepton. The f/Λ limit for excited electrons is approximately an order of magnitude better than for muons and taus due to the enhancement of the cross-section coming from the t -channel contribution.

6.5 Comparisons with Existing Constraints

The limits obtained in this thesis are currently the most stringent constraints on parameters of the phenomenological model introduced in Chapter 2. Constraints on f/Λ obtained using a similar technique as the one described in this thesis as well as limits obtained via different reactions are reviewed in this section.

Searches similar to the one presented in this thesis have been performed by the OPAL collaboration [51, 52] and by the other LEP experiments [53–55] using only a subset of

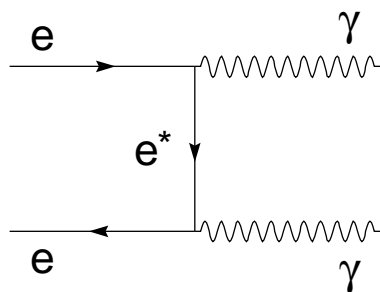


Figure 6.8: Diagram of the excited electron contribution to the process $e^+e^- \rightarrow \gamma\gamma$.

the data analysed in the present work. Limits were also obtained using data collected at a centre-of-mass energy equal to the Z^0 mass [56]. All four LEP collaborations have reported lower limits on the mass of excited charged leptons of the order of 95 to 100 GeV and limits on the strength of the coupling f/Λ of order 0.1 TeV^{-1} for excited electrons and 1 TeV^{-1} for excited muons and taus assuming $f = f'$.

The existence of excited electrons could also be inferred from deviations in the differential cross-section of the process $e^+e^- \rightarrow \gamma\gamma$. Excited electrons would contribute to the reaction via the diagram shown in Figure 6.8. The expected differential cross-section in the context of the model presented in Chapter 2 has been calculated as part of the work presented in this thesis. Details of the calculation can be found in Appendix F. Using results of this calculation, limits on the excited electron coupling strength from studies of the process $e^+e^- \rightarrow \gamma\gamma$ have recently been reported by all four LEP experiments [20, 57]. These constraints are complementary to the searches for singly and pair produced excited electrons. This reaction is comparatively suppressed compared to the single production due to the double interaction of excited electrons with a photon and an electron. However it extends limits to masses beyond the kinematically allowed region of single production. This is a consequence of quantum mechanical effects whereby the excited electron mediating the production of two photons is a virtual² particle. Upper bounds on the quantity f/Λ for the coupling assignment $f = f'$ were calculated at the 95% confidence level to be of order 5 TeV^{-1} for excited electron masses greater than the centre-of-mass energy.

Searches for the existence of excited leptons have also been performed in electron-proton collisions at the HERA collider in Germany. Figure 6.9 shows the excited electron production mechanism in electron-proton collisions. Both the H1 [58] and ZEUS [59] experiments at the HERA collider have reported upper limits on the excited electron coupling strength, f/Λ , of order 1 TeV^{-1} for masses below 200 GeV and assuming $f = f'$.

²Virtual particles are particles that cannot be observed and for which $E^2 + |\mathbf{p}|^2 \neq m^2$. They can have any mass. The existence of virtual particles is a consequence of Heisenberg's uncertainty principle, $\Delta E \Delta t \geq \hbar$.

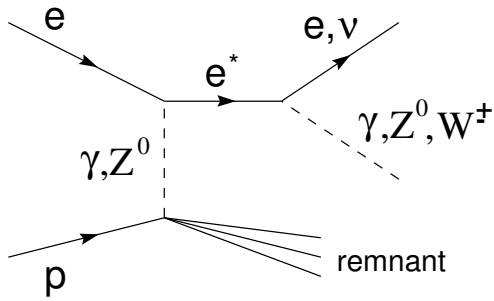


Figure 6.9: Diagram of excited electron production in electron-proton collisions.

Strong bounds on the existence of excited states also exist from the precise measurements of the electron and muon anomalous magnetic moments ($g-2$). Excited leptons could contribute to the anomalous magnetic moment of leptons via diagrams similar to the one shown in Figure 6.10. The possible contributions to the anomalous magnetic moment of lepton have been calculated in [60]. Using results from these theoretical calculations and the most recent measurements of the electron [61] and muon [62] anomalous magnetic moments, upper bounds on the coupling f of order 0.1(1) for excited electrons (muons) can be inferred under the assumptions $f = f'$ and $\Lambda = m_*$. These are strong bounds, comparable to the ones obtained from searches for singly produced excited leptons in e^+e^- collisions. Limits from $g-2$ experiments however rely on theoretical calculations that are very complex and at this point in time only approximate. They are presented here for completeness and should be interpreted only as an indication of the sensitivity of $g-2$ experiments to the existence of excited states.

Figure 6.11 shows a summary of the constraints on the strength of the $e^*e\gamma$ coupling described above and the corresponding limits obtained in this thesis.

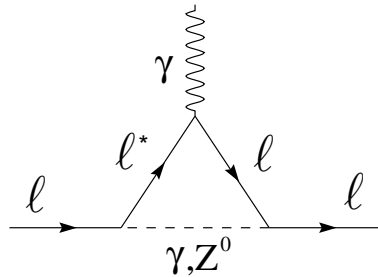


Figure 6.10: Example of one possible excited leptons contribution to the anomalous magnetic moment of leptons.

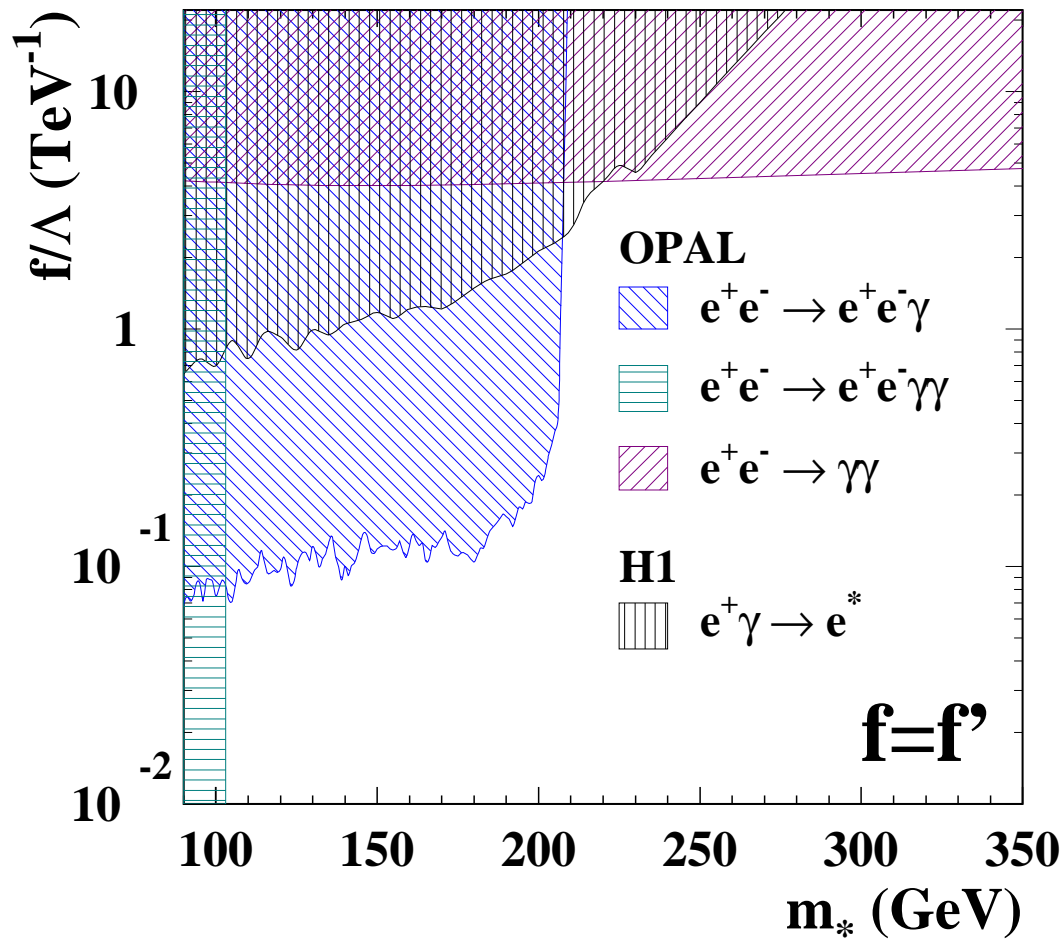


Figure 6.11: Summary of existing constraints on the $e^*e\gamma$ coupling strength expressed in terms of 95% confidence level upper limits on the quantity f/Λ as function of excited electron mass and assuming $f = f'$. The hatched regions represent values of the parameters excluded by the OPAL and H1 experiments.

Conclusions

A search for the production of excited charged leptons in e^+e^- collisions was performed using data collected by the OPAL detector at LEP. The data analysed were recorded at the highest centre-of-mass energy ever achieved in e^+e^- collisions. Selection criteria were developed to identify experimental signatures compatible with the single and pair production of excited charged leptons decaying electromagnetically. The search sensitivity was substantially improved by the use of a kinematic fit technique. No evidence for the existence of excited charged leptons was found. Upper bounds on the product of the cross-section and branching fraction for singly and pair produced excited charge leptons were calculated. From pair production searches, 95% confidence level lower limits on the mass of excited electrons, muons and taus were determined to be 103.2 GeV. From the search for singly produced excited leptons, limits were calculated on the ratio of the coupling constant to the compositeness scale (f/Λ) as a function of excited lepton mass. The results are currently the most stringent constraints on the existence of excited charged leptons.

New experiments that will study matter at a much smaller distance scale are being designed and built. These experiments will provide a unique environment to search for the existence of excited states of leptons in an energy regime that has never been probed before.

The Large Hadron Collider (LHC) [64] under construction in the old LEP tunnel is expected to start colliding protons in the year 2007 at a centre-of-mass energy of 14 TeV. Although experimental signatures expected from the production of excited leptons in proton-proton collisions are harder to disentangle from the large background of strong interaction processes, experiments at the LHC should nevertheless be able to extend the current constraints on f/Λ from single production searches up to masses of order 1 TeV [63].

Research and development work is also being carried out toward the design of a machine called the Next Linear Collider (NLC). This machine would provide in different

mode of operation e^+e^- , $e\gamma$ and $\gamma\gamma$ collisions at a centre-of-mass energy of up to 500 GeV. Lower mass limits of approximately 250 GeV could be obtained from searches for pair produced excited charged leptons in e^+e^- collisions. Given the foreseen luminosity delivered by such a machine, the upper bounds on the quantity f/Λ could be improved by more than an order of magnitude. In addition to production mechanisms identical to the ones studied in this thesis, excited electrons could also be singly produced in $e\gamma$ collisions. Of particular interest is the use of the photon beam polarisation that could be tuned to enhance the excited electron production cross-section for different values of the coupling parameters f and f' [65].

The next generation of high energy experiments will open up a new window of opportunity to look for answers to some of the shortcomings of the Standard Model. The next decade promises to be an exciting time.

Tracks and Clusters Requirements

The following is a summary of the quality requirements applied to reconstructed tracks and energy clusters used in the analysis.

Tracks

- The transverse momentum must be greater than 0.15 GeV.
- Tracks must be reconstructed from at least 50% of the hits expected in the central jet chamber at the given polar angle, and always more than 20 hits.
- The distance of closest approach to the interaction point in the $r - \phi$ plane must be less than 2 cm.
- The distance of closest approach to the interaction point in the z -direction must be less than 25 cm.

Clusters in the electromagnetic calorimeters

- Clusters are formed from the energy deposited in at least one lead glass block of the calorimeter.
- The raw energy of clusters must be greater than 0.1 GeV and 0.25 GeV for clusters in the barrel and endcap electromagnetic calorimeters, respectively.
- The corrected measured energy of clusters in either calorimeter must be greater than 0.001 GeV.

Clusters in the hadronic calorimeter

- The energy in the calorimeter towers must be greater than 0.6 GeV.

General Solution to Kinematic Fit

The solution to a kinematic fit, as outlined in Section 5.2, consists of finding a set of parameters α which minimises the function

$$L = (\hat{\alpha} - \alpha)^T \mathbf{V}^{-1} (\hat{\alpha} - \alpha) + 2\lambda^T \mathbf{g}(\alpha, \mathbf{p})$$

where $\hat{\alpha}$ represents the vector of measured parameters, \mathbf{p} is the set of unmeasured parameters and λ are Lagrange multipliers used to incorporate the set of constraint equations $\mathbf{g}(\alpha, \mathbf{p}) = 0$. If the constraint equations are linear in the parameters α and \mathbf{p} , the solution of the problem can be found in one step. Otherwise, an iterative method based on the linearization of the constraint equations is generally used. The solution presented here closely follows that shown in [66]. At each iteration, initial values of the parameters α_0 and \mathbf{p}_0 are updated by the addition of corrections $\Delta\alpha$ and $\Delta\mathbf{p}$ such that

$$\begin{array}{ll} \alpha_1 = \alpha_0 & \mathbf{p}_1 = \mathbf{p}_0 \\ \alpha_2 = \alpha_0 + \Delta\alpha_2 & \mathbf{p}_2 = \mathbf{p}_0 + \Delta\mathbf{p}_2 \\ \alpha_3 = \alpha_0 + \Delta\alpha_3 & \mathbf{p}_3 = \mathbf{p}_0 + \Delta\mathbf{p}_3 \\ \vdots & \vdots \\ \alpha_k = \alpha_0 + \Delta\alpha_k & \mathbf{p}_k = \mathbf{p}_0 + \Delta\mathbf{p}_k \\ \vdots & \vdots \end{array}$$

The initial estimates of the parameters α are taken to be the measured values themselves ($\alpha_0 = \hat{\alpha}$). Initial values of the unmeasured parameters are determined using different methods, depending on the details of the specific problem. Constraint equations are often used to help calculate these starting values.

On the k^{th} iteration, the Taylor expansion of the constraint equations, assuming

changes in α and \mathbf{p} are small, is given by

$$\mathbf{g}(\alpha_k, \mathbf{p}_k) \approx \mathbf{g}(\alpha_{k-1}, \mathbf{p}_{k-1}) + \left. \frac{\partial \mathbf{g}}{\partial \alpha} \right|_{\alpha_{k-1}, \mathbf{p}_{k-1}} (\Delta \alpha_k - \Delta \alpha_{k-1}) + \left. \frac{\partial \mathbf{g}}{\partial \mathbf{p}} \right|_{\alpha_{k-1}, \mathbf{p}_{k-1}} (\Delta \mathbf{p}_k - \Delta \mathbf{p}_{k-1}) = 0$$

or more simply as

$$\mathbf{g}_{k-1} + \mathbf{A} (\Delta \alpha_k - \Delta \alpha_{k-1}) + \mathbf{B} (\Delta \mathbf{p}_k - \Delta \mathbf{p}_{k-1}) = 0$$

where \mathbf{A} and \mathbf{B} are the matrices of the first derivatives of the constraints with respect to the measured and unmeasured parameters,

$$\mathbf{A} = \left. \frac{\partial \mathbf{g}}{\partial \alpha} \right|_{\alpha_{k-1}, \mathbf{p}_{k-1}}$$

$$\mathbf{B} = \left. \frac{\partial \mathbf{g}}{\partial \mathbf{p}} \right|_{\alpha_{k-1}, \mathbf{p}_{k-1}} .$$

Defining $\mathbf{c} = \mathbf{A} \Delta \alpha_{k-1} + \mathbf{B} \Delta \mathbf{p}_{k-1} - \mathbf{g}_{k-1}$, the function to minimize can be written as

$$L = \Delta \alpha_k^T \mathbf{V}^{-1} \Delta \alpha_k + 2\lambda^T (\mathbf{A} \Delta \alpha_k + \mathbf{B} \Delta \mathbf{p}_k - \mathbf{c}) .$$

The necessary conditions for an extremum are

$$\frac{\partial L}{\partial \alpha} = 0$$

$$\frac{\partial L}{\partial \mathbf{p}} = 0$$

$$\frac{\partial L}{\partial \lambda} = 0$$

leading to the following system of coupled matrix equations

$$\mathbf{V}^{-1} \Delta \alpha_k + \mathbf{A}^T \lambda = 0$$

$$\mathbf{B}^T \lambda = 0$$

$$\mathbf{A} \Delta \alpha_k + \mathbf{B} \Delta \mathbf{p} = \mathbf{c} .$$

This system of equations has to be solved for $\Delta \alpha_k$, $\Delta \mathbf{p}$ and λ . This can be achieved by

rewriting these three equations as

$$\begin{pmatrix} \mathbf{V}^{-1} & 0 & \mathbf{A}^T \\ 0 & 0 & \mathbf{B}^T \\ \mathbf{A} & \mathbf{B} & 0 \end{pmatrix} \begin{pmatrix} \Delta\boldsymbol{\alpha}_k \\ \Delta\mathbf{p}_k \\ \lambda \end{pmatrix} = \begin{pmatrix} 0 \\ 0 \\ \mathbf{c} \end{pmatrix} .$$

Assuming the inverse of the partitioned matrix is

$$\begin{pmatrix} \mathbf{V}^{-1} & 0 & \mathbf{A}^T \\ 0 & 0 & \mathbf{B}^T \\ \mathbf{A} & \mathbf{B} & 0 \end{pmatrix}^{-1} = \begin{pmatrix} \mathbf{C}_{11} & \mathbf{C}_{21}^T & \mathbf{C}_{31}^T \\ \mathbf{C}_{21} & \mathbf{C}_{22} & \mathbf{C}_{32}^T \\ \mathbf{C}_{31} & \mathbf{C}_{32} & \mathbf{C}_{33} \end{pmatrix}$$

then the solution to the system of equations is simply

$$\begin{pmatrix} \Delta\boldsymbol{\alpha}_k \\ \Delta\mathbf{p}_k \\ \lambda \end{pmatrix} = \begin{pmatrix} \mathbf{V}^{-1} & 0 & \mathbf{A}^T \\ 0 & 0 & \mathbf{B}^T \\ \mathbf{A} & \mathbf{B} & 0 \end{pmatrix}^{-1} \begin{pmatrix} 0 \\ 0 \\ \mathbf{c} \end{pmatrix} = \begin{pmatrix} \mathbf{C}_{11} & \mathbf{C}_{21}^T & \mathbf{C}_{31}^T \\ \mathbf{C}_{21} & \mathbf{C}_{22} & \mathbf{C}_{32}^T \\ \mathbf{C}_{31} & \mathbf{C}_{32} & \mathbf{C}_{33} \end{pmatrix} \begin{pmatrix} 0 \\ 0 \\ \mathbf{c} \end{pmatrix} = \begin{pmatrix} \mathbf{C}_{31}^T \mathbf{c} \\ \mathbf{C}_{32}^T \mathbf{c} \\ \mathbf{C}_{33} \mathbf{c} \end{pmatrix} .$$

The matrix elements \mathbf{C}_{ij} can be found by requiring

$$\begin{pmatrix} \mathbf{V}^{-1} & 0 & \mathbf{A}^T \\ 0 & 0 & \mathbf{B}^T \\ \mathbf{A} & \mathbf{B} & 0 \end{pmatrix} \begin{pmatrix} \mathbf{C}_{11} & \mathbf{C}_{21}^T & \mathbf{C}_{31}^T \\ \mathbf{C}_{21} & \mathbf{C}_{22} & \mathbf{C}_{32}^T \\ \mathbf{C}_{31} & \mathbf{C}_{32} & \mathbf{C}_{33} \end{pmatrix} = \begin{pmatrix} \mathbf{1} & 0 & 0 \\ 0 & \mathbf{1} & 0 \\ 0 & 0 & \mathbf{1} \end{pmatrix}$$

such that

$$\begin{aligned} \mathbf{C}_{11} &= \mathbf{V} - \mathbf{V}\mathbf{A}^T\mathbf{W}\mathbf{A}\mathbf{V} + \mathbf{V}\mathbf{A}^T\mathbf{W}\mathbf{B}(\mathbf{B}^T\mathbf{W}\mathbf{B})^{-1}\mathbf{B}^T\mathbf{W}\mathbf{A}\mathbf{V} \\ \mathbf{C}_{21} &= -(\mathbf{B}^T\mathbf{W}\mathbf{B})^{-1}\mathbf{B}^T\mathbf{W}\mathbf{A}\mathbf{V} \\ \mathbf{C}_{22} &= (\mathbf{B}^T\mathbf{W}\mathbf{B})^{-1} \\ \mathbf{C}_{31} &= \mathbf{W}\mathbf{A}\mathbf{V} - \mathbf{W}\mathbf{B}(\mathbf{B}^T\mathbf{W}\mathbf{B})^{-1}\mathbf{B}^T\mathbf{W}\mathbf{A}\mathbf{V} \\ \mathbf{C}_{32} &= \mathbf{W}\mathbf{B}(\mathbf{B}^T\mathbf{W}\mathbf{B})^{-1} \\ \mathbf{C}_{33} &= -\mathbf{W} + \mathbf{W}\mathbf{B}(\mathbf{B}^T\mathbf{W}\mathbf{B})^{-1}\mathbf{B}^T\mathbf{W} . \end{aligned}$$

where $\mathbf{W} = (\mathbf{A}\mathbf{V}\mathbf{A}^T)^{-1}$ is used to simplify the algebra. Finally, the corrections used to update the initial values of the measured and unmeasured parameters, as well as the Lagrange

multipliers are

$$\begin{aligned}\Delta\alpha_k &= \mathbf{C}_{31}^T \mathbf{c} = \mathbf{V}\mathbf{A}^T\mathbf{W} - (\mathbf{V}\mathbf{A}^T\mathbf{W}\mathbf{B}(\mathbf{B}^T\mathbf{W}\mathbf{B})^{-1}\mathbf{B}^T\mathbf{W})(\mathbf{A}\Delta\alpha_{k-1} + \mathbf{B}\Delta\mathbf{p}_{k-1} - \mathbf{g}_{k-1}) \\ \Delta\mathbf{p}_k &= \mathbf{C}_{32}^T \mathbf{c} = (\mathbf{B}^T\mathbf{W}\mathbf{B})^{-1}\mathbf{B}^T\mathbf{W}(\mathbf{A}\Delta\alpha_{k-1} + \mathbf{B}\Delta\mathbf{p}_{k-1} - \mathbf{g}_{k-1}) \\ \lambda &= \mathbf{C}_{33} \mathbf{c} = (-\mathbf{W} + \mathbf{W}\mathbf{B}(\mathbf{B}^T\mathbf{W}\mathbf{B})^{-1}\mathbf{B}^T\mathbf{W})(\mathbf{A}\Delta\alpha_{k-1} + \mathbf{B}\Delta\mathbf{p}_{k-1} - \mathbf{g}_{k-1}) .\end{aligned}$$

Thus, at each iteration, updated values of the parameters and Lagrange multipliers are given by

$$\begin{pmatrix} \alpha_k \\ \mathbf{p}_k \\ \lambda \end{pmatrix} = \begin{pmatrix} \alpha_0 \\ \mathbf{p}_0 \\ 0 \end{pmatrix} + \begin{pmatrix} \Delta\alpha_k \\ \Delta\mathbf{p}_k \\ \lambda \end{pmatrix} .$$

The updated covariance matrix is found by error propagation

$$\begin{aligned}\text{cov} \begin{pmatrix} \alpha_k \\ \mathbf{p}_k \\ \lambda \end{pmatrix} &= \begin{pmatrix} \partial\alpha_k/\partial\alpha_0 & \partial\alpha_k/\partial\mathbf{p}_0 & \partial\alpha_k/\partial\lambda \\ \partial\mathbf{p}_k/\partial\alpha_0 & \partial\mathbf{p}_k/\partial\mathbf{p}_0 & \partial\mathbf{p}_k/\partial\lambda \\ \partial\lambda/\partial\alpha_0 & \partial\lambda/\partial\mathbf{p}_0 & \partial\lambda/\partial\lambda \end{pmatrix} \begin{pmatrix} \mathbf{V} & 0 & 0 \\ 0 & 0 & 0 \\ 0 & 0 & 0 \end{pmatrix} \begin{pmatrix} \partial\alpha_k/\partial\alpha_0 & \partial\alpha_k/\partial\mathbf{p}_0 & \partial\alpha_k/\partial\lambda \\ \partial\mathbf{p}_k/\partial\alpha_0 & \partial\mathbf{p}_k/\partial\mathbf{p}_0 & \partial\mathbf{p}_k/\partial\lambda \\ \partial\lambda/\partial\alpha_0 & \partial\lambda/\partial\mathbf{p}_0 & \partial\lambda/\partial\lambda \end{pmatrix}^T \\ &= \begin{pmatrix} (\partial\alpha_k/\partial\alpha_0)\mathbf{V}(\partial\alpha_k/\partial\alpha_0)^T & (\partial\alpha_k/\partial\alpha_0)\mathbf{V}(\partial\mathbf{p}_k/\partial\alpha_0)^T & (\partial\alpha_k/\partial\alpha_0)\mathbf{V}(\partial\lambda/\partial\alpha_0)^T \\ (\partial\mathbf{p}_k/\partial\alpha_0)\mathbf{V}(\partial\alpha_k/\partial\alpha_0)^T & (\partial\mathbf{p}_k/\partial\alpha_0)\mathbf{V}(\partial\mathbf{p}_k/\partial\alpha_0)^T & (\partial\mathbf{p}_k/\partial\alpha_0)\mathbf{V}(\partial\lambda/\partial\alpha_0)^T \\ (\partial\lambda/\partial\alpha_0)\mathbf{V}(\partial\alpha_k/\partial\alpha_0)^T & (\partial\lambda/\partial\alpha_0)\mathbf{V}(\partial\mathbf{p}_k/\partial\alpha_0)^T & (\partial\lambda/\partial\alpha_0)\mathbf{V}(\partial\lambda/\partial\alpha_0)^T \end{pmatrix} \\ &= \begin{pmatrix} \mathbf{C}_{11} & \mathbf{C}_{21}^T & 0 \\ \mathbf{C}_{21} & \mathbf{C}_{22} & 0 \\ 0 & 0 & -\mathbf{C}_{33} \end{pmatrix} .\end{aligned}$$

where $(\partial\mathbf{c}/\partial\alpha_0) = -\mathbf{A}$ was used in the last step.

Error Estimates of Kinematic Fit Input Variables

Estimates of the energy and angular resolution of different components of the detector are obtained using events containing two leptons produced back-to-back. These parameterisations of the detector response are taken as an estimate of the uncertainty on individual energy and angular measurements and are used as input to the kinematic fits performed for each selected event.

Leptons produced from the decay of excited leptons have a wide range of energies which is a consequence of the excited lepton mass but also of the production mode (single or pair production of excited leptons). Pair produced excited leptons of masses close to the kinematic limit give leptons of about 50 GeV on average. Single production of excited leptons, for masses near the kinematic limit, result in one energetic and one low energy lepton. So the estimates of the uncertainty on the quantities used as input to the kinematic fits must be valid for a wide range of energies. The data sample used for this study includes approximately 10 pb^{-1} of calibration data recorded at a centre-of-mass energy equal to the Z^0 mass as well as the entire set of data recorded at $\sqrt{s} = 183\text{-}209 \text{ GeV}$.

In order to obtain error estimates independent of Monte Carlo modelling, an effort has been made to extract an estimate of the uncertainty on each kinematic variable from real data.

Given their well defined kinematic properties, non-radiative¹ di-lepton events are used in this study. The two leptons contained in these events are produced back-to-back and their energy is equal to the beam energy. Di-lepton events are selected by requiring events

¹Events that do not contain photon(s) radiated off initial or final state particles involved in a collision. At high energy, a photon is often radiated along the beam axis decreasing the effective centre-of-mass energy of a collision.

to contain exactly two coplanar² jets. Each jet is categorised using the same lepton and photon identification requirements described in Section 4.2. Events containing two electron or two muon candidates are required to satisfy $R_{\text{vis}} > 0.8$, where the quantity R_{vis} is defined in Section 4.3, in order to reject radiative lepton pair events and background from two-photon events. Following closely on the definition of Section 4.3, tau pair events are defined as events with two identified tau candidates, one tau and one electron or muon, or one identified muon and one electron. Tau pair events are also required to satisfy $R_{\text{vis}} < 0.85$ in order to reject muon and electron pair events where one jet was misidentified as well as background from two-photon events.

C.1 Electromagnetic Calorimeter Response

The electromagnetic calorimeter response is studied using the large sample of non-radiative electron pair events selected using the simple requirements listed above.

Since the energy of each electron is equal to the beam energy, the shape of the distribution $(E - E_{\text{beam}})/\sigma_E$, where E and σ_E are the energy and error on the measured energy of each electron, is an indicator of how well the errors truly represent the energy measurement uncertainties. Such distributions obtained using electron pair events recorded at a centre-of-mass energy equal to the Z^0 mass and at 189 GeV are shown in Figure C.1. These distributions were obtained using the errors calculated as part of the standard OPAL event reconstruction. Results of a fit to a Gaussian distribution appear as a solid line superimposed on each histogram. Although the fit agreement with data is poor, it nevertheless gives a sufficient approximation to each distribution. In analogy with pull³ distributions which exhibit a standard normal distribution if errors are correctly estimated, the distributions shown in Figure C.1 should also be Gaussian distributed with a variance equal to one. Both distributions do have a variance close to one which indicates that the errors are indeed a good estimate of the uncertainty on the measured energy in the electromagnetic calorimeter.

Since the two electrons in non-radiative electron pair events are produced back-to-back, the shape of the distributions $(\theta_1 + \theta_2 - \pi)/\sqrt{\sigma_{\theta_1}^2 + \sigma_{\theta_2}^2}$ and $(\phi_1 - \phi_2 - \pi)/\sqrt{\sigma_{\phi_1}^2 + \sigma_{\phi_2}^2}$

²Two particles are said to be coplanar if their momentum vectors projected onto the x - y plane are separated by exactly 180° .

³A pull value is usually defined in the context of least squares fitting and is defined as the difference between the direct measurement of a variable and its value as obtained from the least squares fit, normalised to the estimated error of this difference.

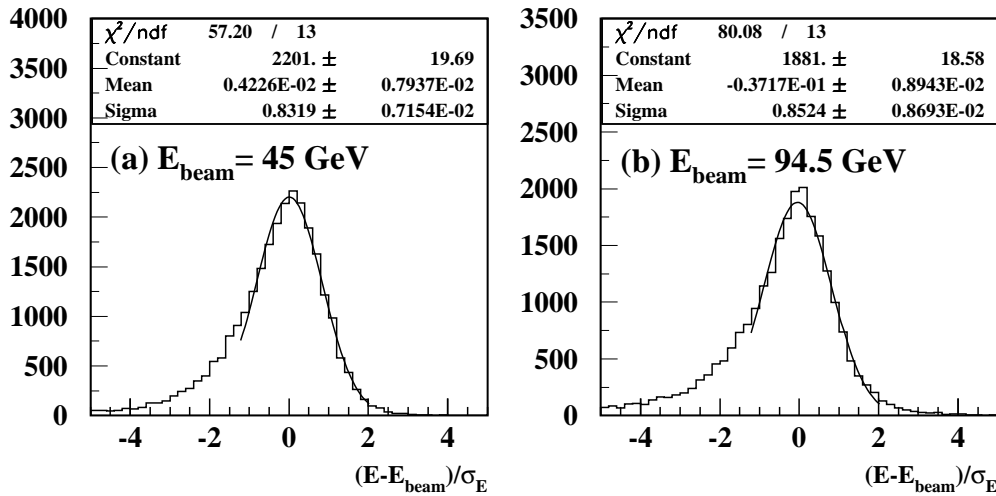


Figure C.1: Distributions of the difference between the electron and beam energy, divided by the error on the measured electron energy for electron pair events recorded at a centre-of-mass energy (a) equal to the Z^0 mass and (b) at 189 GeV. The solid lines show the results of fits to Gaussian functions.

where σ represents the errors on the measured polar (θ) and azimuthal (ϕ) angles of each electron, is an indicator of how accurately the errors obtained by the standard OPAL event reconstruction represent the actual uncertainties on the measurements of the angular and azimuthal angles of a cluster. Figure C.2 shows these two distributions obtained using data events recorded at centre-of-mass energy equal to the Z^0 mass and at 189 GeV. The solid lines superimposed on each histogram represent results of a fit to a Gaussian distribution. All four distributions have a variance different from unity suggesting that the errors obtained by the standard OPAL event reconstruction do not accurately represent the actual uncertainties on the measured polar and azimuthal angle of a cluster. Although the two electrons are genuinely produced back-to-back, by the time they enter the electromagnetic calorimeter, their flight path has been deflected by the magnetic field present in the inner part of the detector, resulting in a shift in the mean value of the distributions $(\phi_1 - \phi_2 - \pi) / \sqrt{\sigma_{\phi_1}^2 + \sigma_{\phi_2}^2}$.

An improved estimate of the uncertainties on the measure polar and azimuthal angles is obtained by parameterising the observed angular resolution of the calorimeter as func-

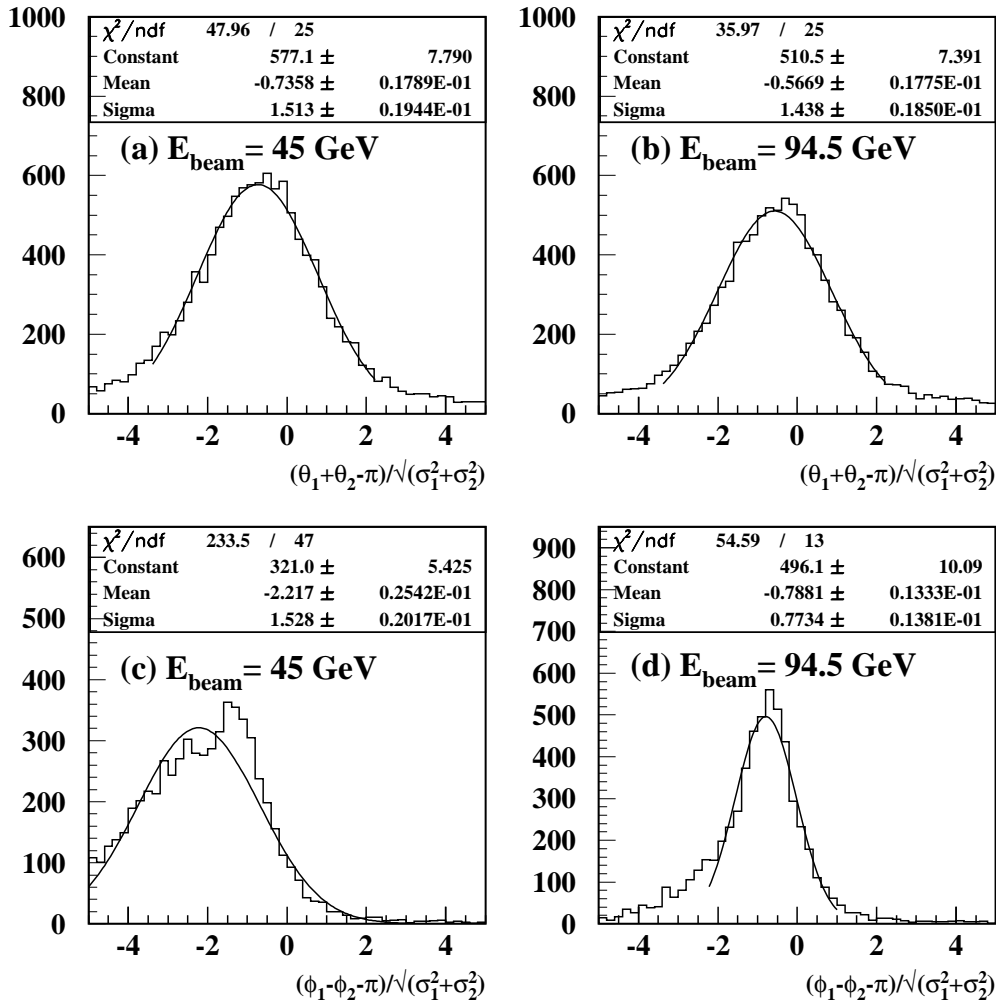


Figure C.2: Distributions of the quantities (a,b) $(\theta_1 + \theta_2 - \pi) / \sqrt{\sigma_{\theta_1}^2 + \sigma_{\theta_2}^2}$ and (c,d) $(\phi_1 - \phi_2 - \pi) / \sqrt{\sigma_{\phi_1}^2 + \sigma_{\phi_2}^2}$ obtained from non-radiative electron pair events collected at a centre-of-mass energy equal to the Z^0 mass and at 189 GeV. The uncertainties on the measured polar (σ_θ) and azimuthal (σ_ϕ) angles of a cluster calculated as part of the standard OPAL event reconstruction are used. Although the two electrons in an event are produced back-to-back, the distributions (c,d) are not centred at zero since the direction of the electrons entering the electromagnetic calorimeter has been altered by the magnetic field permeating the inner part of the detector. The solid lines show the results of fits to Gaussian functions.

tion of the polar angle and energy of a cluster. The spread in the distributions $(\theta_1 + \theta_2 - \pi)$ and $(\phi_1 - \phi_2 - \pi)$ obtained using back-to-back electron pair events is proportional to the calorimeter angular resolution. Figures C.3(a,b) show the variance of these distributions as function of the mean polar angle of the two electrons. The solid lines show the results of a fit to a first and zeroth order polynomials. Data points in the problematic overlap region between the barrel and endcap calorimeter ($0.72 < |\cos \theta| < 0.8$) are excluded from the fit in Figure C.3(b). In that region, the value of each individual $|\cos \theta|$ bin is used as an estimate of the azimuthal resolution of the calorimeter.

The remaining dependence of the angular resolution on the cluster energy, after taking into account the angular dependence parameterised above, is shown in Figures C.3(c,d) along with results of fits to the data.

The angular resolution of the calorimeter obtained from this study is used as an estimate of the uncertainty on the measured polar and azimuthal angles of a single cluster. Given that the electromagnetic calorimeter angular resolution was found using the information from both electrons in each event, the uncertainty (σ) on the measured position (θ or ϕ) of a cluster is in general given by

$$\sigma = \frac{f_1(\cos \theta) f_2(E)}{\sqrt{2}}$$

where the functions f_1 and f_2 represent the polar angle and energy dependence determined above and summarised in Table C.1.

To ensure that these new estimates of the uncertainties on the measured polar and azimuthal angle of a cluster describe reasonably well the measurements errors, the distributions $(\theta_1 + \theta_2 - \pi)/\sqrt{\sigma_{\theta_1}^2 + \sigma_{\theta_2}^2}$ and $(\phi_1 - \phi_2 - \pi)/\sqrt{\sigma_{\phi_1}^2 + \sigma_{\phi_2}^2}$ are plotted in Figure C.4 using these new error estimates. The variance of these distributions is equal to one indicating that the new uncertainty parameterisations are indeed a good estimate of the measurement errors on individual clusters of energy in the electromagnetic calorimeter.

C.2 Tracking Detectors Response

The combined tracking detectors response is studied using both electron and muon pair events.

Since the momentum of each electron or muon in an event is approximately equal to the beam energy, the variance of the quantity $(p - E_{\text{beam}})/\sigma_p$, where p and σ_p are the

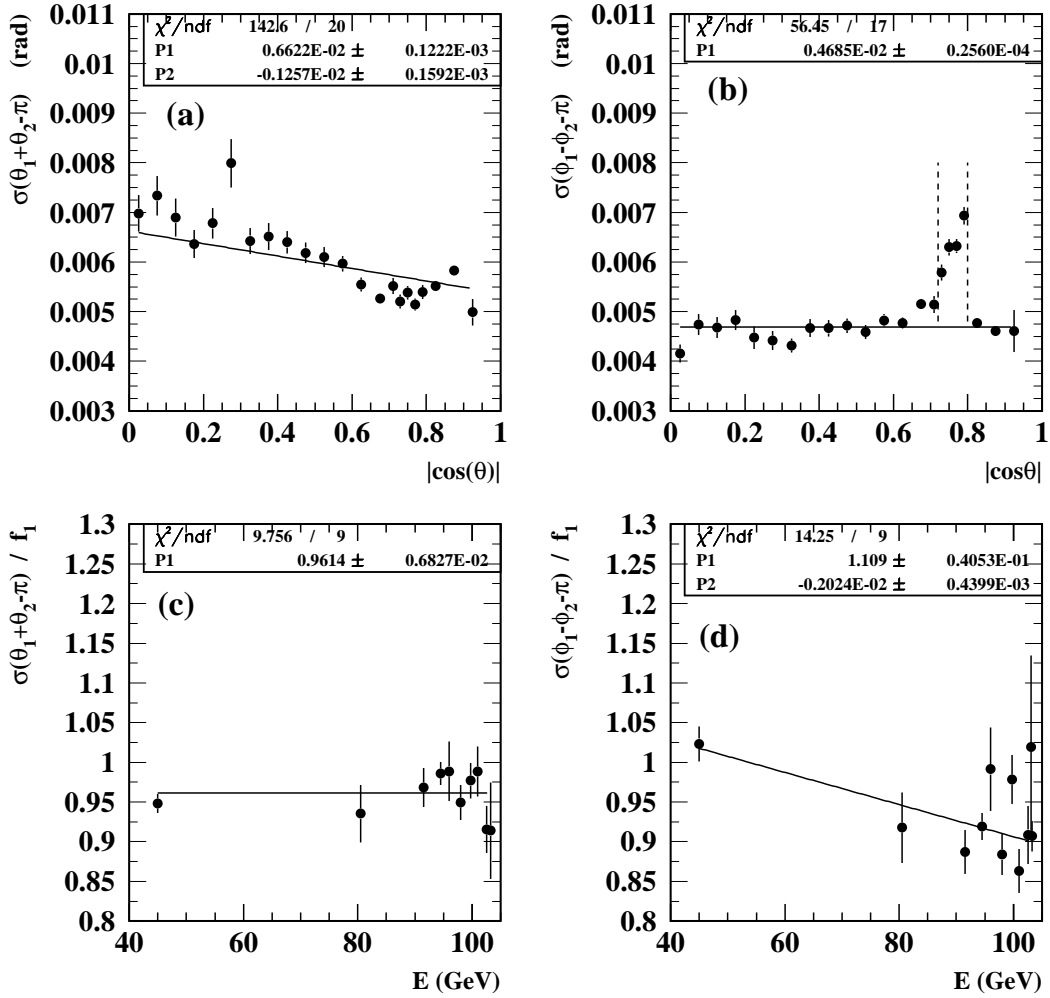


Figure C.3: Variances of the distributions (a) $(\theta_1 + \theta_2 - \pi)$ and (b) $(\phi_1 - \phi_2 - \pi)$ for electromagnetic energy clusters in electron pair events as function of the mean polar angle of the clusters. The bottom two plots show the variances of the distributions (c) $(\theta_1 + \theta_2 - \pi)$ and (d) $(\phi_1 - \phi_2 - \pi)$ as function of the energy of the clusters after removing the angular dependence obtained in (a) and (b) and given by the functions f_1 listed in Table C.1. The solid lines are the results of a fit to the data. Data points lying in the overlap region between the barrel and endcap electromagnetic calorimeter ($0.72 < \cos \theta < 0.8$) are excluded from the fit in (b).

Errors	Angular dependence (mrad)	Energy dependence
σ_{θ_γ}	$f_1 = (0.66 \times 10^{-2}) - (0.13 \times 10^{-2}) \cdot \cos \theta $	$f_2 = 0.96$
σ_{ϕ_γ}	$\left\{ \begin{array}{l} f_1 = 0.0047 \quad \cos \theta < 0.72, \cos \theta \geq 0.80 \\ f_1 = 0.0058 \quad 0.72 \geq \cos \theta < 0.74 \\ f_1 = 0.0063 \quad 0.74 \geq \cos \theta < 0.76 \\ f_1 = 0.0063 \quad 0.76 \geq \cos \theta < 0.78 \\ f_1 = 0.0069 \quad 0.78 \geq \cos \theta < 0.80 \end{array} \right.$	$f_2 = (1.11) - (0.20 \times 10^{-2}) \cdot E$
$\sigma_{\theta_{\text{trk}}}$	$\left\{ \begin{array}{l} f_1 = (0.22 \times 10^{-2}) - (0.12 \times 10^{-3}) \cdot \cos \theta \\ f_1 = (0.39 \times 10^{-2}) + (0.35 \times 10^{-2}) \cdot \cos \theta \\ f_1 = (0.48 \times 10^{-2}) - (0.15 \times 10^{-2}) \cdot \cos \theta \end{array} \right.$	$\left\{ \begin{array}{l} f_2 = (0.71) + (0.54 \times 10^{-2}) \cdot p \quad \cos \theta < 0.7 \text{ CZ hits} \\ f_2 = (1.42) - (0.57 \times 10^{-2}) \cdot p \quad \cos \theta < 0.7 \text{ no CZ hits} \\ f_2 = (1.07) + (0.17 \times 10^{-2}) \cdot p \quad \cos \theta \geq 0.7 \end{array} \right.$
$\sigma_{\phi_{\text{trk}}}$	$f_1 = (-0.27 \times 10^{-3}) + \frac{0.68 \times 10^{-3}}{\sqrt{1 - \cos \theta ^2}}$	$f_2 = 0.91$
σ_{θ_τ}	$f_1 = (0.034) - (0.015) \cdot \cos \theta $	$f_2 = (1.42) - (0.011) \cdot E_{\text{vis}}$
σ_{ϕ_τ}	$f_1 = (0.99 \times 10^{-2}) + (0.013) \cdot \cos \theta $	$f_2 = (0.14) + \frac{3.36}{\sqrt{E_{\text{vis}}}}$

Table C.1: Summary of the angular parameterisation functions (f_1) and energy corrections (f_2) of different angular measurement uncertainties. Since these functions were obtained using the information from both particles in each event, the uncertainty on a single measurement is given by $\sigma = (f_1 \cdot f_2) / \sqrt{2}$.

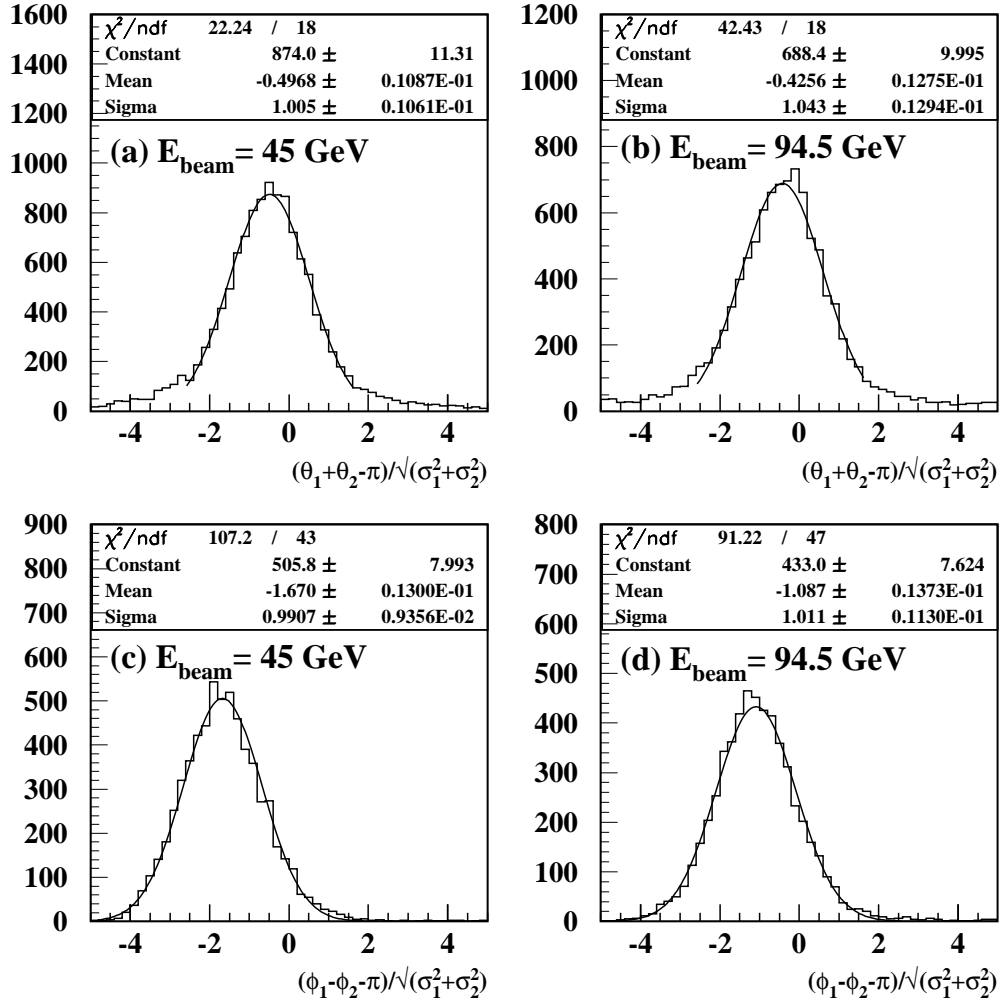


Figure C.4: Distributions of the quantities $(\theta_1 + \theta_2 - \pi) / \sqrt{\sigma_{\theta_1}^2 + \sigma_{\theta_2}^2}$ and $(\phi_1 - \phi_2 - \pi) / \sqrt{\sigma_{\phi_1}^2 + \sigma_{\phi_2}^2}$ obtained from non-radiative electron pair events collected at a centre-of-mass energy (a,c) equal to the Z^0 mass and (b,d) at 189 GeV. The uncertainties on the measured polar (σ_θ) and azimuthal (σ_ϕ) angles of a cluster are calculated using the new parameterisation of the electromagnetic calorimeter angular resolution. The solid lines show the results of fits to Gaussian functions.

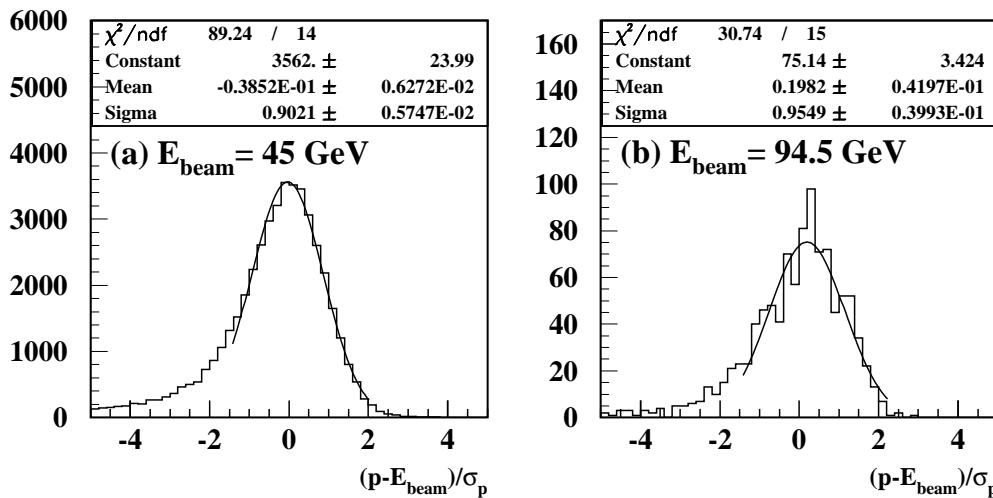


Figure C.5: Distributions of the difference between the measured track momentum and the beam energy, divided by the error on the track momentum as calculated by the OPAL tracking reconstruction algorithm. These distributions are obtained using electron and muon pair events collected at a centre-of-mass energy (a) equal to the Z^0 mass and (b) at 189 GeV. The solid lines show the results of fits to Gaussian functions.

measured track momentum and its associated error as calculated by the OPAL track reconstruction algorithm, is an indicator of how well the errors truly represent the uncertainty on the track momentum measurement. Figure C.5 shows distributions of this quantity obtained using tracks from electron and muon pair events collected at a centre-of-mass energy equal to the Z^0 mass and at 189 GeV. Results of a fit to a Gaussian distribution appear as a solid line superimposed on each histogram. Both distributions have a variance close to one which indicates that the errors obtained by the OPAL tracking reconstruction algorithm are indeed a good estimate of the uncertainty on the measured momentum of a track.

Error estimates on the measurement of the polar and azimuthal angles of a track are also obtained from the OPAL track reconstruction algorithm. Figure C.6 shows distributions of the quantities $(\theta_1 + \theta_2 - \pi)/\sqrt{\sigma_{\theta_1}^2 + \sigma_{\theta_2}^2}$ and $(\phi_1 - \phi_2 - \pi)/\sqrt{\sigma_{\phi_1}^2 + \sigma_{\phi_2}^2}$ for electron and muon pair events recorded at a centre-of-mass energy equal to the Z^0 mass and at 189 GeV. The variance of these distributions is larger than one suggesting that the

errors obtained from the OPAL track reconstruction algorithm underestimates the actual measurements uncertainties.

Following a similar approach as the one outlined in the previous section, the angular resolution of the tracking system, parameterised as function of polar angle and momentum of a track, is taken to be an estimate of the uncertainty on the measured direction of individual tracks. Both electron and muon pair events are used to extract an estimate of the angular resolution of tracks.

The angular dependence of the tracking system polar angle resolution was obtained for three different cases: tracks in the barrel region ($|\cos\theta| < 0.75$) with hits in the Z-chambers (CZ), tracks in the barrel region without hits in the Z-chambers and tracks pointing toward the detector endcap region ($|\cos\theta| \geq 0.75$). These three different parameterisation functions are necessary since the measurement of a track polar angle is obtained using a different technique in each case, resulting in a different angular resolution. The variances of $(\theta_1 + \theta_2 - \pi)$ distributions, obtained using both electron and muon pair events, are shown as function of polar angle and track momentum in Figure C.7. The momentum dependence is plotted after removing the angular dependence given by the function f_1 and assuming that the momentum of tracks in non-radiative electron and muon pair events is approximately equal to the beam energy. The solid lines shown in Figure C.7 represent results from various fits to the data also summarised in Table C.1. The azimuthal resolution is parameterised following a similar approach. Figure C.8 shows the variances of $(\phi_1 - \phi_2 - \pi)$ distributions as function of polar angle and track momentum. Results from the fits to the data appear in Table C.1 and are shown as solid lines.

Assuming both tracks in an event have a similar momentum and direction, an estimate of the uncertainty on the direction of a single track is given by

$$\sigma = \frac{f_1(\cos\theta)f_2(p)}{\sqrt{2}}$$

Figure C.9 shows distributions of the quantities $(\theta_1 + \theta_2 - \pi)/\sqrt{\sigma_{\theta_1}^2 + \sigma_{\theta_2}^2}$ and $(\phi_1 - \phi_2 - \pi)/\sqrt{\sigma_{\phi_1}^2 + \sigma_{\phi_2}^2}$ for electron and muon pair events obtained using the new uncertainty estimates on individual tracks. The variances of these distributions are close to one indicating that the new estimates of the uncertainties on the measured direction of a track are comparable to individual track measurements errors.

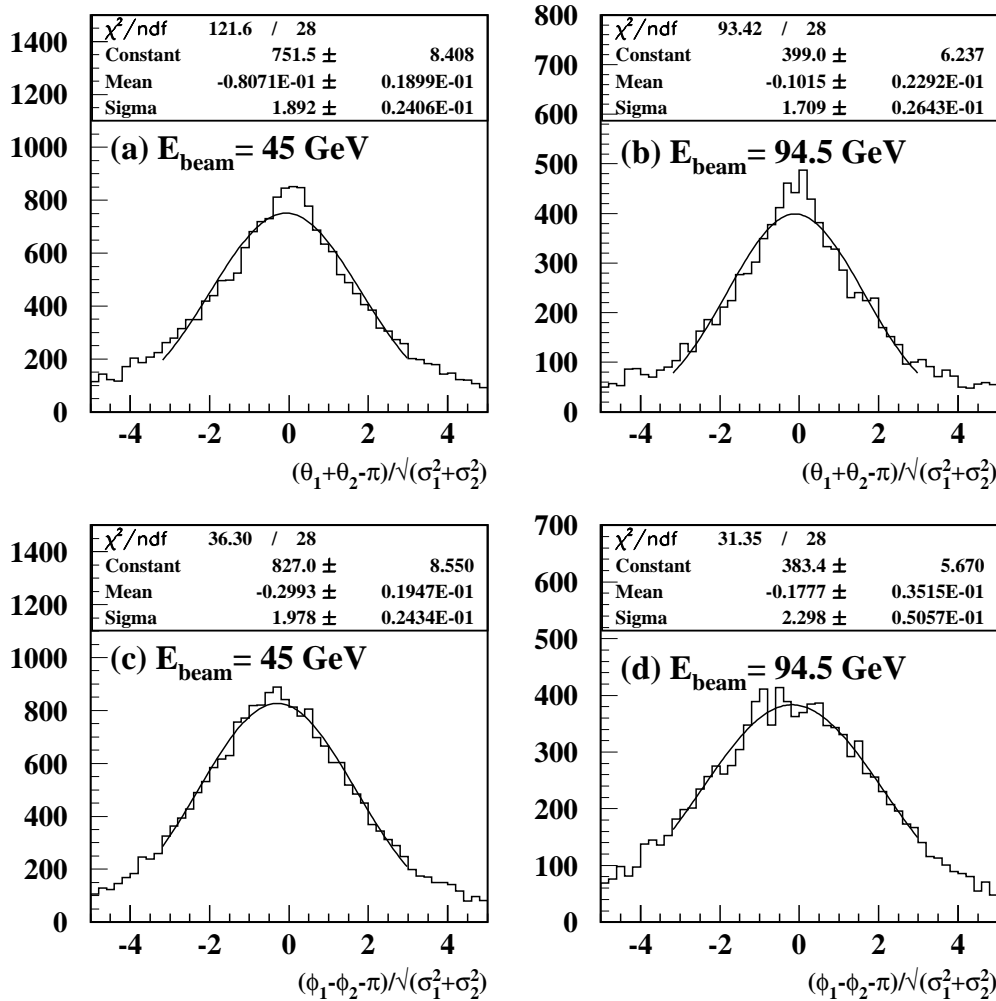


Figure C.6: Distributions of the quantities (a,b) $(\theta_1 + \theta_2 - \pi) / \sqrt{\sigma_{\theta_1}^2 + \sigma_{\theta_2}^2}$ and (c,d) $(\phi_1 - \phi_2 - \pi) / \sqrt{\sigma_{\phi_1}^2 + \sigma_{\phi_2}^2}$ obtained using non-radiative electron and muon pair events. Measurements of the angles are given by the direction of the tracks and the uncertainties are taken to be the errors calculated by the OPAL track reconstruction algorithm. The solid lines show the results of fits to Gaussian functions.

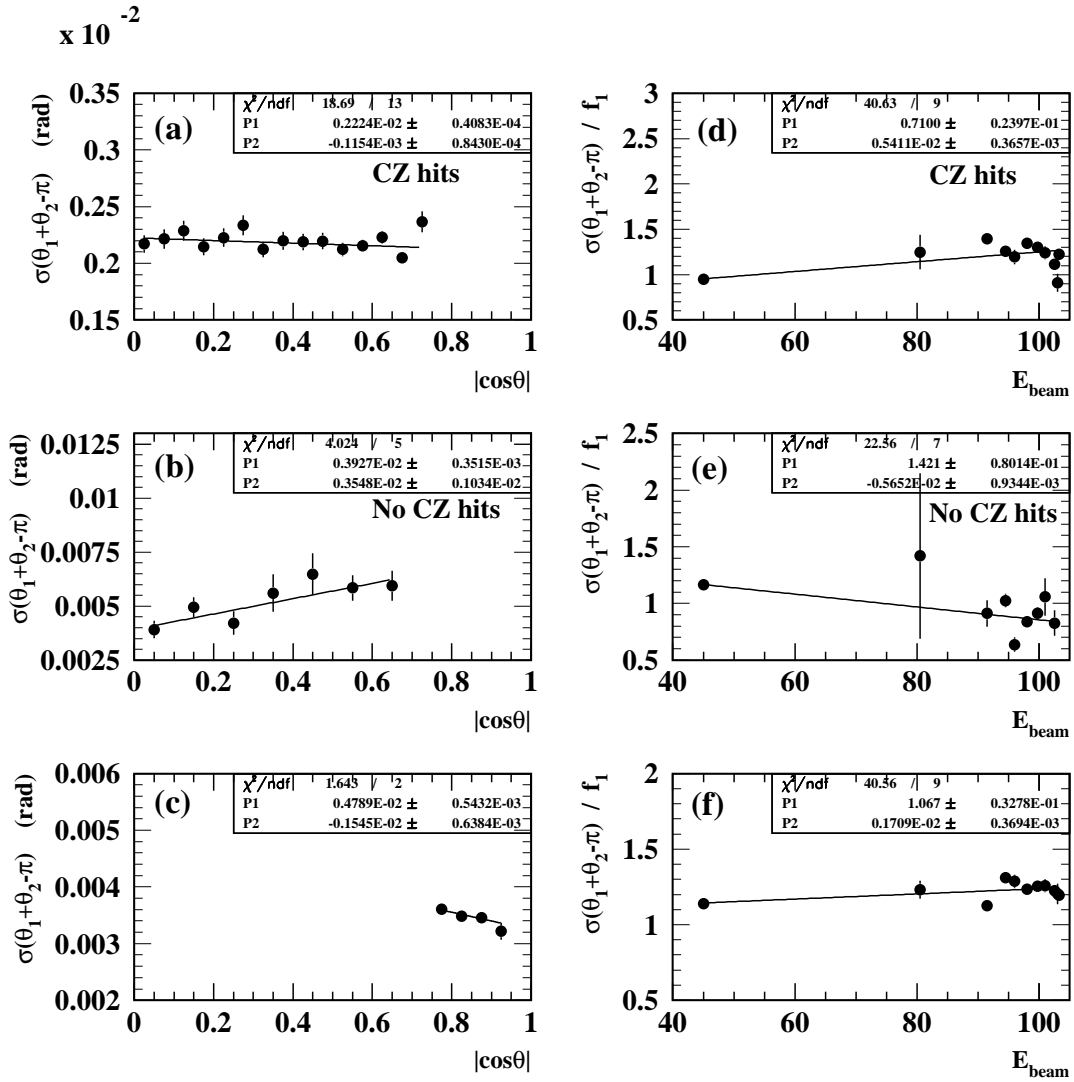


Figure C.7: Variance of the distributions $(\theta_1 + \theta_2 - \pi)$ for tracks in electron and muon pair events as function of (a-c) the mean polar angle and (d-f) track momentum. Plots (d-f) are obtained after taking into account the polar angle dependence obtained in (a-c) and parameterised by the functions f_1 listed in Table C.1. The solid lines are the results of a fit to the data. Different parameterisations are obtained for (a,d) tracks in the barrel region ($|\cos\theta| < 0.7$) with hits in the Z-chambers (CZ), (b,e) tracks in the barrel region without hits in the Z-chambers and (c,f) tracks in the endcap region of the detector ($|\cos\theta| \geq 0.7$).

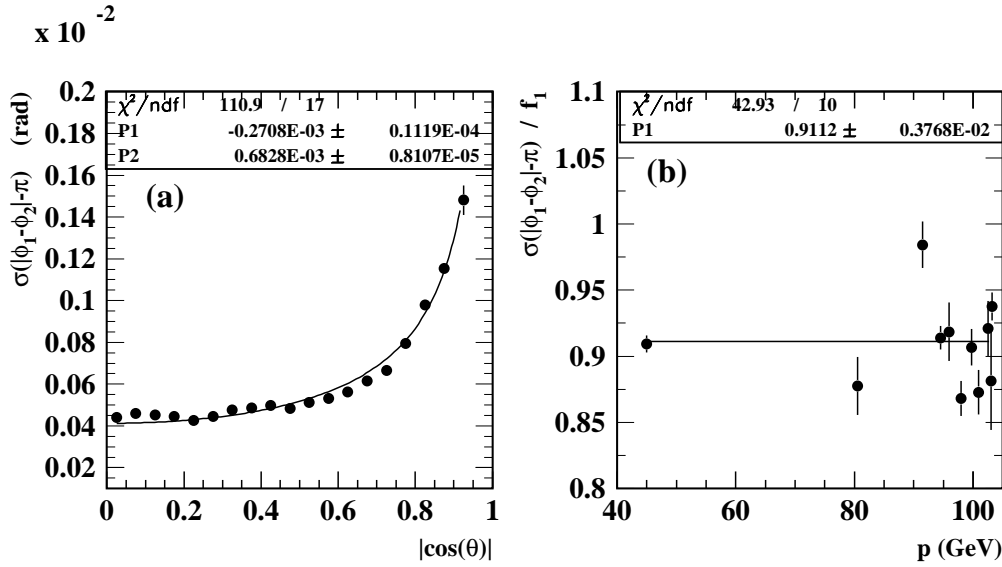


Figure C.8: Variance of the distributions $(\phi_1 - \phi_2 - \pi)$ for tracks in electron and muon pair events as function of (a) the mean polar angle and (b) track momentum. Plot (b) is obtained after taking into account the polar angle dependence found in (a) and parameterised by the function f_1 listed in Table C.1. The solid lines are the results of a fit to the data.

C.3 Taus

The direction of tau candidates is taken to be the axis of the jet. The uncertainty in the tau direction comes from the presence of undetected neutrinos from the tau decay and from the finite resolution of different subdetectors.

An estimate of the uncertainties on the measured polar and azimuthal angles of tau candidates is obtained using coplanar tau pair events where both taus have a similar amount of energy, corrected for double-counting of tracks and energy clusters, deposited in the detector. Distributions of the quantities $(\theta_1 + \theta_2 - \pi)$ and $(\phi_1 - \phi_2 - \pi)$ as function of the mean polar angle and visible energy of both taus are shown in Figure C.10. Results of the fits to the data are shown as solid lines and summarised in Table C.1. Distributions of the quantities $(\theta_1 + \theta_2 - \pi) / \sqrt{\sigma_{\theta_1}^2 + \sigma_{\theta_2}^2}$ and $(\phi_1 - \phi_2 - \pi) / \sqrt{\sigma_{\phi_1}^2 + \sigma_{\phi_2}^2}$ are Gaussian distributed with a variance of one indicating that the uncertainties on the measured direction of a tau candidate estimated from the parameterisation given above are a good estimate of the measurements uncertainties.

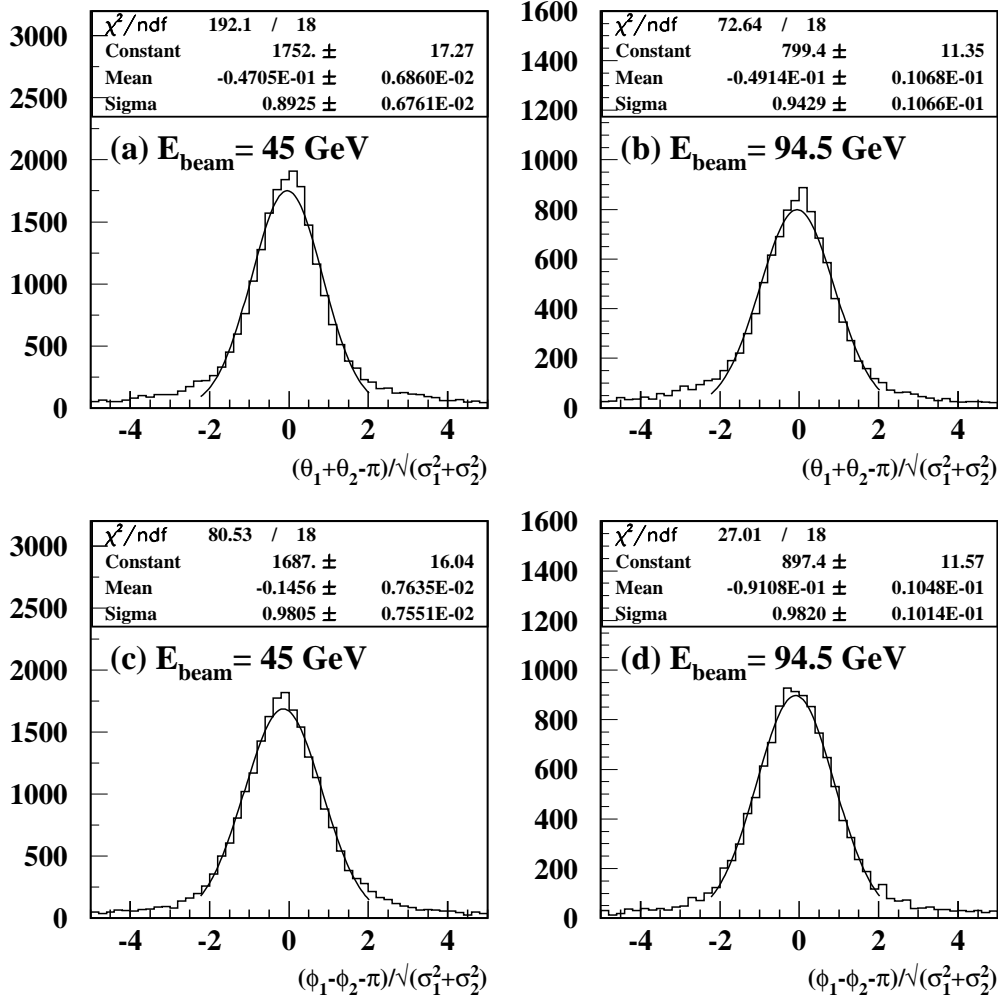


Figure C.9: Distributions of the quantities (a,b) $(\theta_1 + \theta_2 - \pi) / \sqrt{\sigma_{\theta_1}^2 + \sigma_{\theta_2}^2}$ and (c,d) $(\phi_1 - \phi_2 - \pi) / \sqrt{\sigma_{\phi_1}^2 + \sigma_{\phi_2}^2}$ obtained using non-radiative electron and muon pair events. Measurements of the angles are given by the direction of the tracks and the error on each measured angle is calculated using the new error parameterisation described in the text. The solid lines show the results of fits to Gaussian functions.

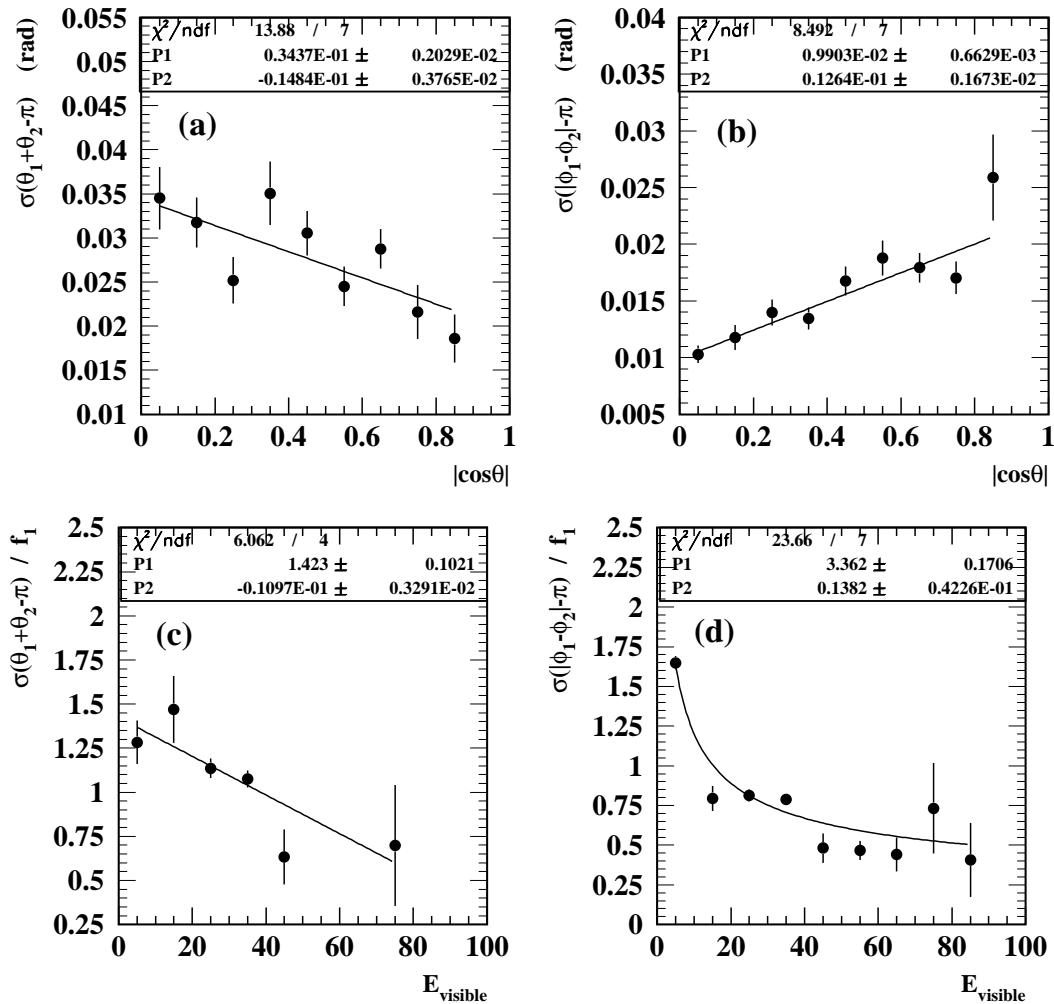


Figure C.10: Variance of the distributions $(\theta_1 + \theta_2 - \pi)$ and $(\phi_1 - \phi_2 - \pi)$ obtained using tau pair events as function of (a,b) the mean polar angle and (c,d) visible energy of the two taus. Plot (c,d) are obtained after taking into account the polar angle dependence found in (a,b) and parameterised by the functions f_1 listed in Table C.1. The solid lines are the results of a fit to the data.

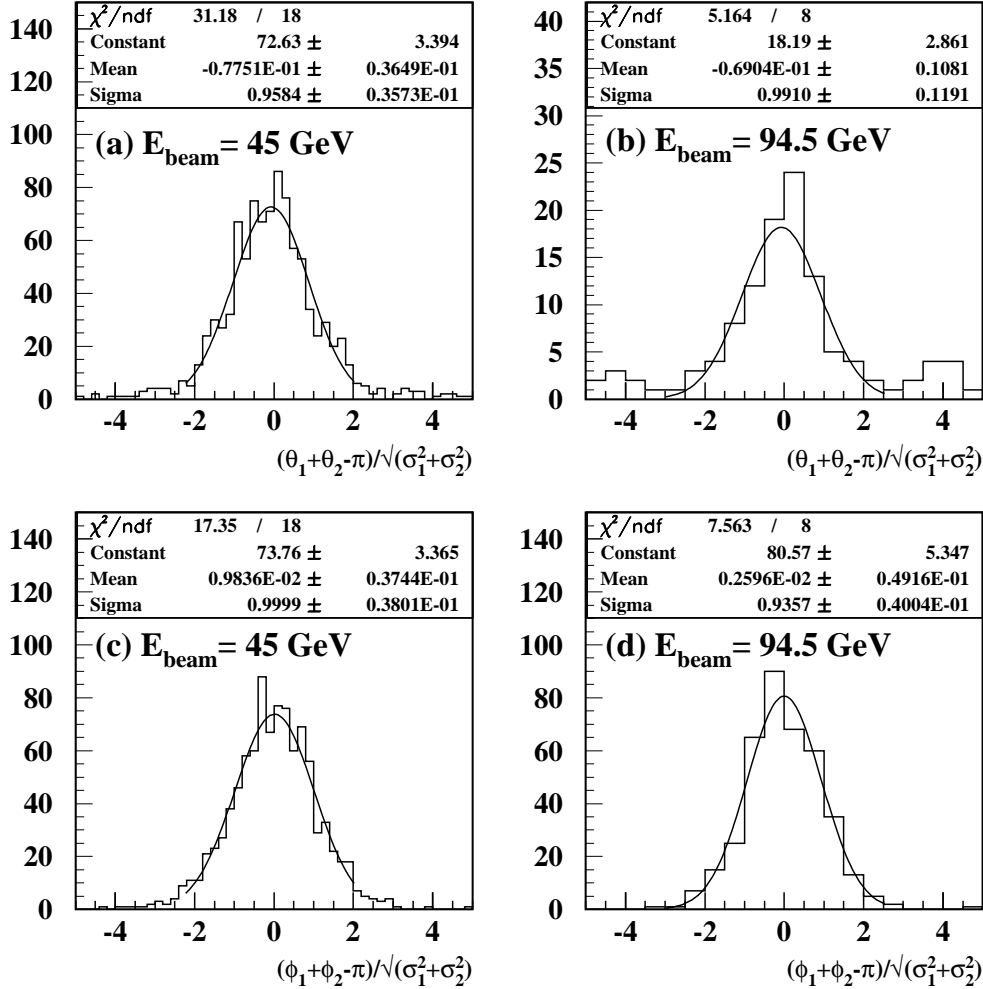


Figure C.11: Distributions of the quantities (a,b) $(\theta_1 + \theta_2 - \pi) / \sqrt{\sigma_{\theta_1}^2 + \sigma_{\theta_2}^2}$ and (c,d) $(\phi_1 - \phi_2 - \pi) / \sqrt{\sigma_{\phi_1}^2 + \sigma_{\phi_2}^2}$ obtained from tau pair events collected at a centre-of-mass energy equal to the Z^0 mass and at 189 GeV. The uncertainties on the measured polar (σ_θ) and azimuthal (σ_ϕ) angles are obtained from the angular resolution parameterisation presented in the text. The solid lines show the results of fits to Gaussian functions.

Efficiency, Mass Resolution and Correction Factor Interpolation

In order to calculate limits on the product of the cross-section and the branching fraction of excited leptons, the signal efficiencies, invariant mass resolutions and corrections to the efficiency due to a non-Gaussian component of the mass distributions must all be calculable for arbitrary values of excited lepton mass and collision centre-of-mass energy. To achieve this, these quantities were parameterised as function of the excited lepton mass scaled by the centre-of-mass energy (m_*/\sqrt{s}). Figures D.2-D.6 show results of the various parameterisations superimposed on the values obtained from simulated event samples at different excited lepton mass and centre-of-mass energy. The different functions are tabulated in Table D.1.

The signal efficiency is defined as the ratio of the number of events selected using the criteria described in Chapters 4 and 5 to the total number of events generated assuming a 100% electromagnetic branching fraction.

The mass resolution at a specific value of excited lepton mass and centre-of-mass energy is obtained by fitting the reconstructed invariant mass of selected events to a Gaussian distribution. The variance of the Gaussian fit is taken as an estimate of the mass resolution.

Correction factors to account for a non-Gaussian component of the mass distributions are calculated as the area under the Gaussian fit of the invariant mass distributions, expressed in number of events, divided by the number of events selected.

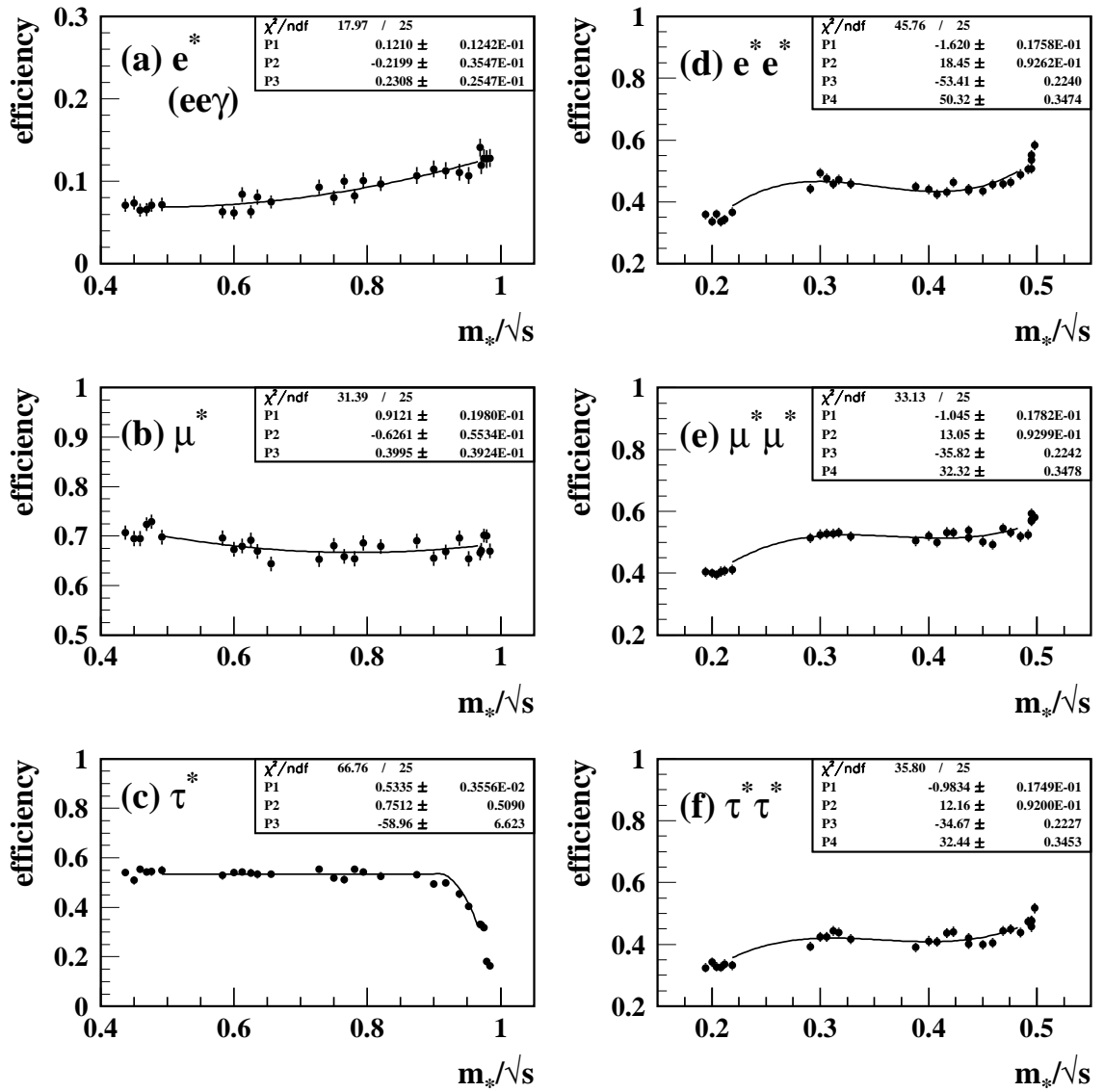


Figure D.1: Efficiencies for the single and pair production selection criteria as a function of excited lepton mass scaled by the centre-of-mass energy (m_*/\sqrt{s}) for the selections of (a-c) $ll\gamma$ and (d-f) $ll\gamma\gamma$ event. The points represent efficiencies obtained using simulated event samples at different mass and centre-of-mass energy. The solid lines show results of a fit to the data points.

$e^*(e\gamma)$	$\epsilon = 0.12 - 0.22 \cdot (m^*/\sqrt{s}) + 0.23 \cdot (m^*/\sqrt{s})^2$ $\sigma_m = 0.36 + 0.084 \cdot (m^*/\sqrt{s})$ $f_c = 0.74$
$e^*(e\gamma)$	$\epsilon = -0.26 + 1.89 \cdot (m^*/\sqrt{s}) - 1.09 \cdot (m^*/\sqrt{s})^2$ $\sigma_m = 2.02 - 8.27 \cdot (m^*/\sqrt{s}) + 15.62 \cdot (m^*/\sqrt{s})^2 - 8.80 \cdot (m^*/\sqrt{s})^3$ $f_c = 0.72$
μ^*	$\epsilon = 0.91 - 0.63 \cdot (m^*/\sqrt{s}) + 0.40 \cdot (m^*/\sqrt{s})^2$ $\sigma_m = -0.95 + 4.42 \cdot (m^*/\sqrt{s}) - 3.38 \cdot (m^*/\sqrt{s})^2$ $f_c = 0.85$
τ^*	$\epsilon = \begin{cases} 0.53 & (m^*/\sqrt{s}) < 0.9 \\ 0.53 + 0.75 \cdot (m^*/\sqrt{s} - 0.9) - 58.96 \cdot (m^*/\sqrt{s} - 0.9)^2 & (m^*/\sqrt{s}) \geq 0.9 \end{cases}$ $\sigma_m = 1.25 + 0.72 \cdot (m^*/\sqrt{s})$ $f_c = 0.70$
e^*e^*	$\epsilon = -1.62 + 18.45 \cdot (m^*/\sqrt{s}) - 53.41 \cdot (m^*/\sqrt{s})^2 + 50.32 \cdot (m^*/\sqrt{s})^3$ $\sigma_m = -0.025 + 2.10 \cdot (m^*/\sqrt{s}) - 3.89 \cdot (m^*/\sqrt{s})^2$ $f_c = 0.70$
$\mu^*\mu^*$	$\epsilon = -1.04 + 13.05 \cdot (m^*/\sqrt{s}) - 35.82 \cdot (m^*/\sqrt{s})^2 + 32.32 \cdot (m^*/\sqrt{s})^3$ $\sigma_m = 1.46 - 12.59 \cdot (m^*/\sqrt{s}) + 40.50 \cdot (m^*/\sqrt{s})^2 - 42.07 \cdot (m^*/\sqrt{s})^3$ $f_c = 0.72$
$\tau^*\tau^*$	$\epsilon = -0.98 + 12.16 \cdot (m^*/\sqrt{s}) - 34.67 \cdot (m^*/\sqrt{s})^2 + 32.44 \cdot (m^*/\sqrt{s})^3$ $\sigma_m = 4.93 - 42.55 \cdot (m^*/\sqrt{s}) + 139.50 \cdot (m^*/\sqrt{s})^2 - 147.5 \cdot (m^*/\sqrt{s})^3$ $f_c = 0.76$

Table D.1: Parameterisation of the signal efficiency (ϵ), mass resolution (σ_m) in GeV and efficiency correction factor (f_c) for each type of excited lepton production.

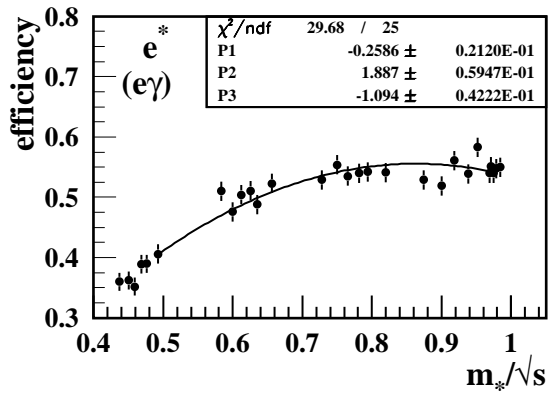


Figure D.2: Efficiency of the $e\gamma$ event selection as a function of excited lepton mass scaled by the centre-of-mass energy (m_*/\sqrt{s}). The points show the efficiency obtained using simulated event samples at different mass and centre-of-mass energy. The solid lines represent results of a fit to the data points

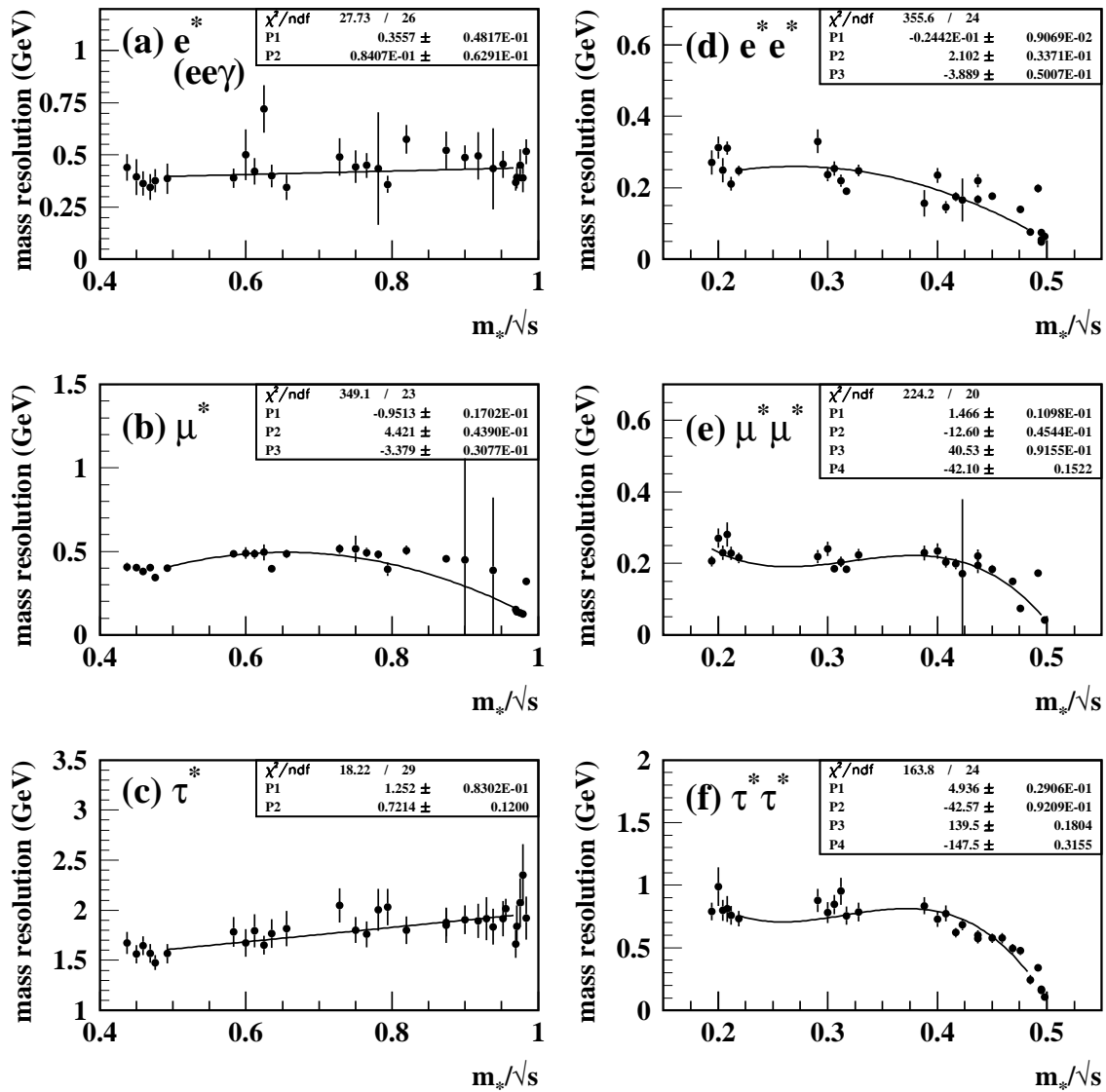


Figure D.3: Invariant mass resolution as a function of excited lepton mass scaled by the centre-of-mass energy (m_*/\sqrt{s}) for the selections of (a-c) $ll\gamma$ and (d-f) $ll\gamma\gamma$ events. The points show the mass resolutions obtained using simulated event samples at different masses and centre-of-mass energies. The solid lines represent $\tau \tau$ results of the parameterisations.

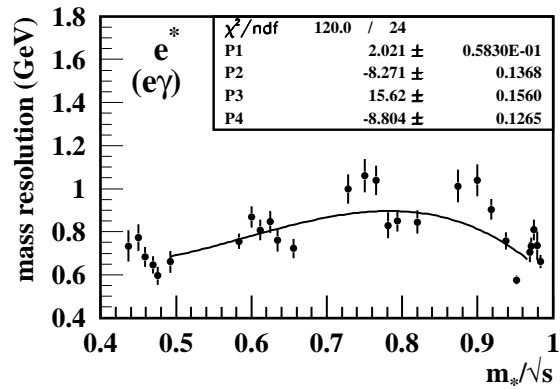


Figure D.4: Invariant mass resolution for $e\gamma$ events as a function of excited lepton mass scaled by the centre-of-mass energy (m_*/\sqrt{s}). The points show the mass resolution obtained using simulated event samples at different masses and centre-of-mass energies. The solid line represents results of the parameterisation.

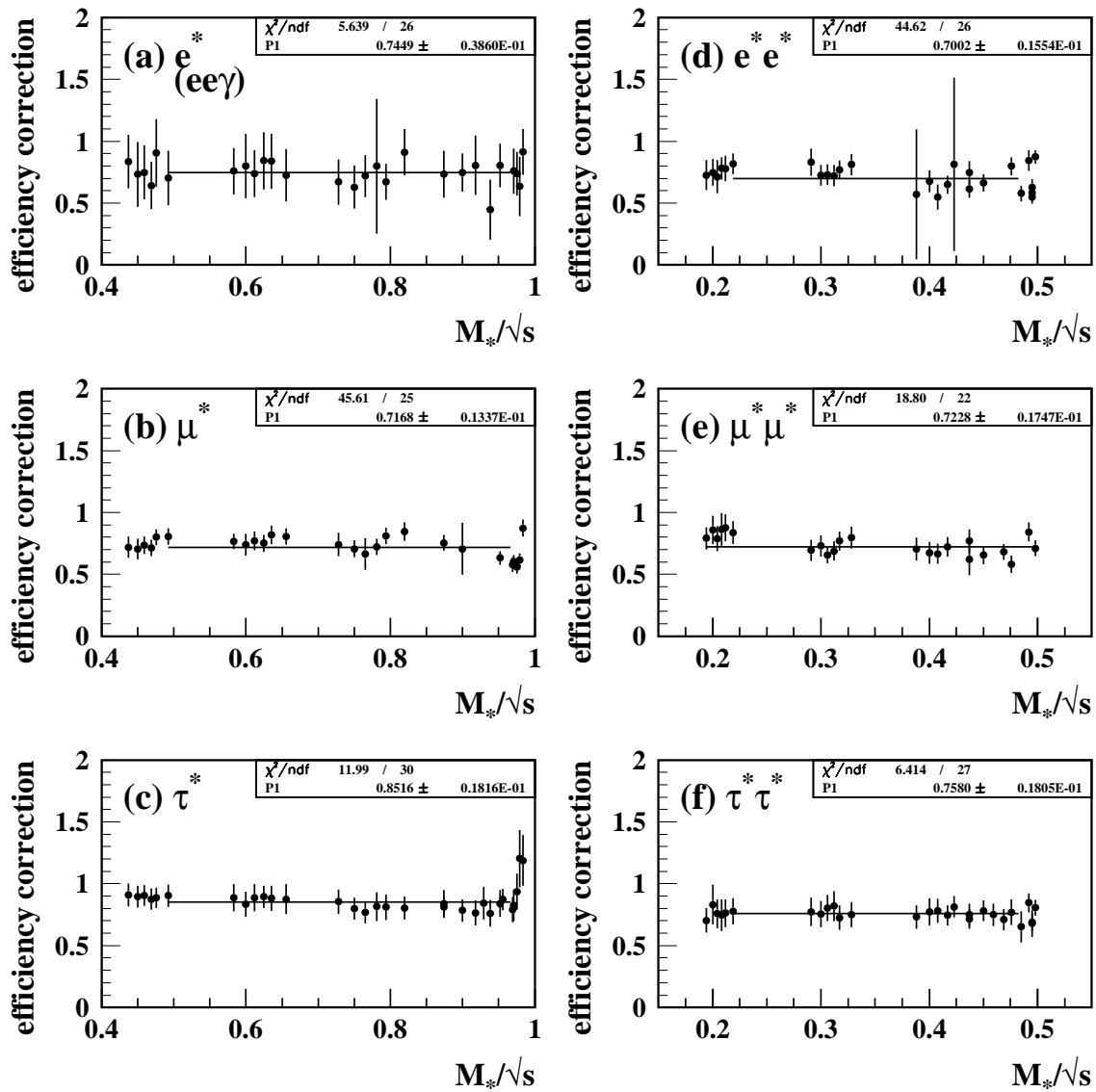


Figure D.5: Efficiency correction factor as a function of excited lepton mass scaled by the centre-of-mass energy (m_*/\sqrt{s}) for the selections of (a-c) $ll\gamma$ and (d-f) $ll\gamma\gamma$ events. The points show the correction factors calculated using simulated event samples at different masses and centre-of-mass energies. The solid lines represent results of the parameterisations.

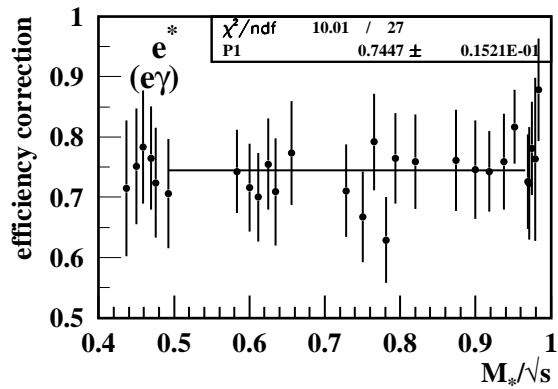


Figure D.6: Efficiency correction factor for $e\gamma$ events as a function of excited lepton mass scaled by the centre-of-mass energy (m_*/\sqrt{s}). The points show the correction factors calculated using simulated event samples at different masses and centre-of-mass energies. The solid line represent results of the parameterisation.

Confidence Level Calculation

Results from a search for new phenomena are usually expressed in terms of the discovery or exclusion of a signal at a specific confidence level. There exist different approaches in calculating the degree of compatibility of an experimental outcome with new physics processes. In the following, the method known as the Modified Frequentist approach [67, 68] is summarised.

For any monotonically increasing test statistic (X) with respect to more signal-like experiments, the confidence in the background plus signal hypothesis (CL_{s+b}) is given by the probability that the estimator be less than or equal to the value observed in the experiment (X_{obs}),

$$CL_{s+b} = P_{s+b}(X \leq X_{\text{obs}}), \quad (\text{E.1})$$

where

$$P_{s+b}(X \leq X_{\text{obs}}) = \int_{-\infty}^{X_{\text{obs}}} \frac{dP_{s+b}}{dX} dX \quad . \quad (\text{E.2})$$

The quantity dP_{s+b}/dX is the probability density function of the test statistic for experiments with signal and background events. Small values of CL_{s+b} indicate that the data are not compatible with the hypothesis for the presence of both signal and background events. In general, the probability density function of the test statistic is not necessarily analytically calculable in which case a Monte Carlo simulation of experiments satisfying the relevant hypothesis is often necessary to perform the integration. However, since the chosen estimator (Q) in this analysis is defined to depend only on the number of observed candidates in each individual channel, the probability density function dP_{s+b}/dQ is Poisson distributed such that

$$CL_{s+b} = \sum_{Q(\mathbf{n}') \leq Q(\mathbf{n}_{\text{obs}})} \prod_{i=1}^N \frac{e^{-(s_i+b_i)} (s_i + b_i)^{n'_i}}{n'_i!} \quad (\text{E.3})$$

where $Q(\mathbf{n}_{\text{obs}})$ is the likelihood ratio obtained from the observed number of candidate events n_i in each channel i . The sum runs over all the possible outcomes \mathbf{n}' for which the likelihood ratio is less than or equal to the observed one.

Following the same reasoning as above, the confidence in the background only hypothesis is in general given by

$$CL_b = P_b(X \leq X_{\text{obs}}), \quad (\text{E.4})$$

where

$$P_b(X \leq X_{\text{obs}}) = \int_{-\infty}^{X_{\text{obs}}} \frac{dP_b}{dX} dX. \quad (\text{E.5})$$

The quantity dP_b/dX is the probability density function of the test statistic for background only experiments. In analogy with Equation E.3, the confidence in the background only hypothesis for the specific choice of the test statistic used in this analysis is given by

$$CL_b = \sum_{Q(\mathbf{n}') \leq Q(\mathbf{n}_{\text{obs}})} \prod_{i=1}^N \frac{e^{-b_i} b_i^{n'_i}}{n'_i!} \quad (\text{E.6})$$

A value of CL_b close to one would indicate that the experimental data are incompatible with the background only hypothesis and that the signal plus background hypothesis is instead favored.

For most realistic situation, where a large number of channels are considered, the calculation of the quantity CL_{s+b} and CL_b quickly becomes computationally challenging. A method [68] whereby the estimators and probability densities of all possible experimental outcomes of channels are combined two at a time is used to speed up the limit calculations.

E.1 The Modified Frequentist Approach

The value $1 - CL_b$ may be used to quote the confidence in a potential discovery. Similarly, exclusion limits on the existence of signal may be calculated using the confidence level $1 - CL_{s+b}$. This quantity however has the property that for experiments with a number of observed events smaller than the expected background, strong limits can be calculated that not only exclude any signal events but also exclude the background hypothesis to a high level of confidence. Although these limits are valid from a strictly statistical point of view, they reflect the probability of obtaining similar or even stronger exclusion limits

in other experiments with the same expected number of signal and background events. These exclusion limits are not a direct statement about the absence of signal events. For experimental physicists carrying out searches for new phenomena, the quantity of interest given a set of experimental measurements, is the confidence in the signal hypothesis. Unfortunately, it is in general not possible to precisely correct the data for the presence of backgrounds or carry out a completely background-free experiment. Thus, in most searches, it is experimentally impossible to directly calculate the confidence in the signal-only hypothesis.

The technique used in this work, which deals in a more intuitive way with the special situation described above, is called the Modified Frequentist approach. The name of the procedure refers to the fact that it is a departure from a strict frequentist interpretation of limit setting. A quantity CL_s is defined to be the ratio of the confidence in the two hypotheses considered,

$$CL_s \equiv \frac{CL_{s+b}}{CL_b} \quad . \quad (\text{E.7})$$

This quantity, although not itself a confidence but rather a ratio of confidences, is used to exclude the existence of signal events at a fixed confidence level CL given that

$$CL \geq 1 - CL_s \quad . \quad (\text{E.8})$$

Going back to the example described above where an experiment observes less events than the expected background, the exclusion limits obtained using the Modified Frequentist approach would in this case result in more conservative limits. This is sensible since, intuitively, there is not enough information available to distinguish between the signal plus background and background-only hypotheses. The use of the Modified Frequentist approach is a method of obtaining conservative limits on the existence of signal events. The quantity CL_s can be interpreted as an approximation of the confidence in the signal hypothesis that would be obtained if an experiment was performed in the absence of background or equivalently, if the background was precisely known and subtracted from the observed data. The probability of falsely excluding a true signal (often called a type II error in statistics textbooks [43–45]) using the quantity CL_s is in general less than the nominal value $(1 - CL)$. For example, in calculating exclusion limits on the signal at the 95% confidence level (CL), the probability of excluding a true signal is in fact less than 5%. This is a consequence of the fact that the quantity CL_s is not itself a confidence but a ratio of confidences. In statistical terms, the use of CL_s increases the ‘coverage’ of an

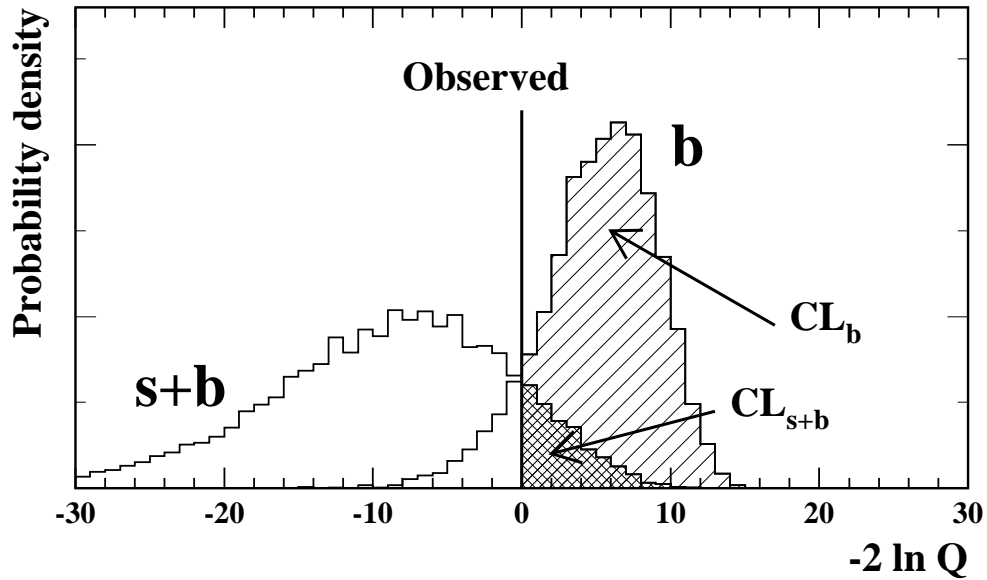


Figure E.1: Example of likelihood ratio (Q) probability density distributions.

analysis.

These concepts are clearly illustrated in Figure E.1 which shows an example of likelihood ratio distributions for the two hypotheses. The quantity CL_{s+b} and CL_b are obtained by integrating from right to left the appropriate normalised probability density distributions up to the observed value of the likelihood ratio. For well separated probability distributions, the most probable result of an experiment will either be the discovery or exclusion of the signal at a high confidence level. For experiments less sensitive to the possible presence of signal events, the probability distributions overlap. Results are more ambiguous. The use of the quantity CL_s can be interpreted as a way of taking this ambiguity into account.

Excited electron contribution to the $e^+e^- \rightarrow \gamma\gamma$ cross-section

In addition to the pair and single production discussed above, the existence of excited electrons could also manifest itself in the production of events containing two photons. Figure F.1 shows (a) the Standard Model interactions and (b) excited electron contributions to the process $e^+e^- \rightarrow \gamma\gamma$. The existence of excited electrons would therefore result in deviations from the Standard Model differential cross-section of events with two photons in the final state.

Limits on the strength of the $e^*e\gamma$ coupling extracted from the $e^+e^- \rightarrow \gamma\gamma$ differential cross-section [69] uses a different form of interaction than the one described in Equation 2.8 for which searches for singly produced excited states rely on. By using a common theoretical framework, the $e^+e^- \rightarrow \gamma\gamma$ process can be used to extend the limits on the $e^*e\gamma$ coupling strength for excited electron masses beyond the kinematically allowed region of single production. Small deviations from the Standard Model predictions are expected even for excited leptons with a mass larger than the centre-of-mass energy of the e^+e^- collisions.

Results from indirect searches, where the existence of e^* is inferred from deviations in the $e^+e^- \rightarrow \gamma\gamma$ differential cross-section, are usually expressed in terms of limits on the $e^*e\gamma$ coupling strength assuming a general extension of the Standard Model. The interaction between an excited lepton, a lepton and a gauge boson (L^*LV) is described by the simplest gauge invariant form of the interaction Lagrangian [70]

$$\mathcal{L}_{L^*LV} = \frac{e}{2} \frac{\kappa}{m_*} \bar{L}^* \sigma_{\mu\nu} L F^{\mu\nu} + \text{hermitian conjugate} \quad (\text{F.1})$$

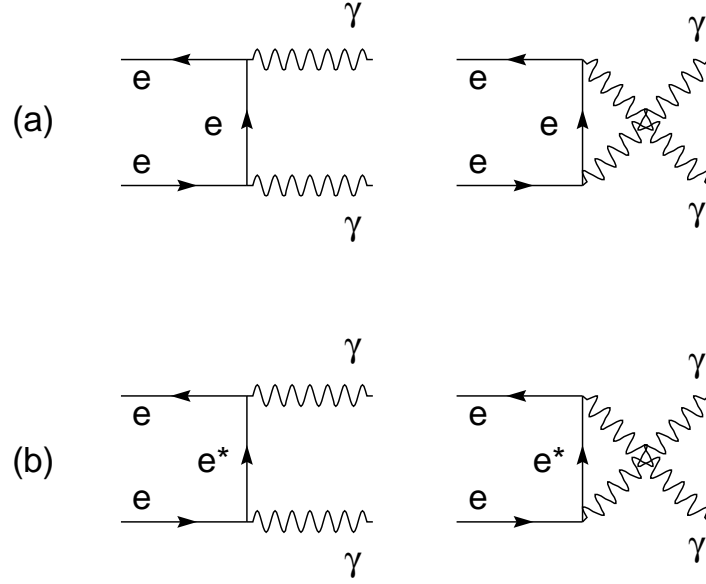


Figure F.1: Diagrams showing the (a) Standard Model and (b) excited electron contributions to the process $e^+e^- \rightarrow \gamma\gamma$ considered in the calculations of the differential cross-section presented in the text.

where $F^{\mu\nu}$ denotes the electromagnetic field tensor¹, $\sigma_{\mu\nu}$ is the covariant bilinear tensor and m_* is the mass of the excited lepton. The parameter κ is a measure of the coupling strength. The $e^+e^- \rightarrow \gamma\gamma$ differential cross-section using this purely magnetic coupling is explicitly calculated in [70] and given by

$$\begin{aligned}
\left(\frac{d\sigma}{d\Omega}\right)_{e^*} = & \left(\frac{d\sigma}{d\Omega}\right)_{\text{QED}} \\
& + \alpha^2 \left\{ \frac{1}{2} \left(\frac{\kappa}{m_*}\right)^4 (E^2 \sin^2 \theta + m_*^2) \left(\frac{q^4}{(q^2 - m_*^2)^2} + \frac{q'^4}{(q'^2 - m_*^2)^2} \right) \right. \\
& + 4 \left(\frac{\kappa}{m_*}\right)^4 \frac{m_*^2 E^4 \sin^2 \theta}{(q^2 - m_*^2)(q'^2 - m_*^2)} \\
& \left. + \left(\frac{\kappa}{m_*}\right)^2 \left[\frac{q^2}{q^2 - m_*^2} + \frac{q'^2}{q'^2 - m_*^2} + E^2 \sin^2 \theta \left(\frac{1}{q^2 - m_*^2} + \frac{1}{q'^2 - m_*^2} \right) \right] \right\} \quad (\text{F.2})
\end{aligned}$$

where $\left(\frac{d\sigma}{d\Omega}\right)_{\text{QED}}$ is the Born level Standard Model differential cross-section, θ is the polar

¹ $F_{\mu\nu} = \partial_\mu A_\nu - \partial_\nu A_\mu$

angle of one of the photons with respect to the incoming electron, E is the beam energy ($E = \sqrt{s}/2$), $q^2 = -2E^2(1 - \cos\theta)$ and $q'^2 = -2E^2(1 + \cos\theta)$. Since the two outgoing photons are indistinguishable, $\cos\theta$ is defined to be positive. Limits on the strength of the $e^*e\gamma$ coupling, κ , are expressed as a function of m_* [69].

The interaction Lagrangian of Equation F.1 leads to large contributions to the anomalous magnetic moment of electrons and muons and the size of the coupling, κ , is therefore already severely constrained by existing g-2 precision measurements [60]. In fact, limits on κ from g-2 measurements are approximately an order of magnitude better than limits from $e^+e^- \rightarrow \gamma\gamma$ calculated using Equation F.2. It therefore does not appear relevant to express limits on the strength of the coupling assuming a purely magnetic interaction.

On the other hand, limits on the $e^*e\gamma$ coupling strength from the search for singly produced excited leptons are calculated using the theoretical framework described in Section 2.3. The effective Lagrangian density describing the L^*LV interaction, Equation 2.8, is chosen to have a chiral symmetry which protects Standard Model leptons from acquiring large anomalous magnetic moments.

When expressed in terms of the physical gauge fields observed in nature using the transformation of Equation 2.3, this Lagrangian density leads to the following chiral magnetic vertex [6]

$$\Gamma_\mu^{L^*LV} = \frac{e}{2\Lambda} f_V q^\nu \sigma_{\mu\nu} (1 - \gamma_5) \quad (\text{F.3})$$

where q^ν is the momentum of the gauge boson and f_V are defined in Equation 2.10-2.12. Assuming this chiral conserving interaction, the coupling $e^*e\gamma$ is less severely constrained since contributions to the electron and muon anomalous magnetic moments are suppressed, by definition. It still however permits observable deviations in the process $e^+e^- \rightarrow \gamma\gamma$ which are not excluded by g-2 measurements. In addition, limits from indirect searches expressed in this framework can be easily compared and combined with limits obtained from searches for singly produced excited electrons.

To achieve this, deviations from the Standard Model $e^+e^- \rightarrow \gamma\gamma$ differential cross-section need to be calculated assuming a chiral conserving $e^*e\gamma$ coupling. With the existence of excited electrons, the four diagrams shown in Figure F.1 are considered. The differential cross-section is calculated using the L^*LV vertex given in Equation F.3 and combined with the standard QED interaction $e\bar{L}\gamma_\mu LA_\mu$. The excited electron propagator is taken to be the usual fermion expression with a mass m_* , $i(\gamma^\mu q_\mu + m_*)/(q^2 - m_*^2)$, where q_μ is the momentum vector of the excited lepton. Summing over the outgoing photon polarisations and neglecting the mass of the electron, the resulting differential cross-section

is

$$\begin{aligned} \left(\frac{d\sigma}{d\Omega}\right)_{e^*} &= \left(\frac{d\sigma}{d\Omega}\right)_{\text{QED}} \\ &+ \frac{\alpha^2 f_\gamma^4 m_*^2}{4 \Lambda^4} \left[\frac{q^4}{(q^2 - m_*^2)^2} + \frac{q'^4}{(q'^2 - m_*^2)^2} + \frac{8 E^4 \sin^2 \theta}{(q^2 - m_*^2)(q'^2 - m_*^2)} \right] \end{aligned} \quad (\text{F.4})$$

where the same notation as for Equation F.2 is used. There are no terms of order $(f_\gamma/\Lambda)^2$ in Equation F.4 since the chiral conserving coupling ensures that the excited electron diagrams do not interfere with the Standard Model diagrams.

Equation F.4 is now being widely used among the four LEP experiments [57] to calculate constraints on the existence of excited electron from studies of the process $e^+e^- \rightarrow \gamma\gamma$.

Bibliography

- [1] S.L. Glashow, Nucl. Phys. **22** (1961) 579;
S. Weinberg, Phys. Rev. Lett. **19** (1967) 1264;
A. Salam, in “Elementary Particle Theory”, N. Svartholm ed., Almqvist and Wiksell, Stockholm (1968).
- [2] G. 't Hooft, Nucl. Phys. **B33** (1971) 173;
G. 't Hooft, Nucl. Phys. **B35** (1971) 167.
- [3] P.W. Higgs, Phys. Rev. **145** (1966) 1156.
- [4] See for example, H. Terazawa, Phys. Rev. **D22** (1980) 184.
- [5] K. Hagiwara, D. Zeppenfeld and S. Komamiya, Z. Phys. **C29** (1985) 115.
- [6] F. Boudjema, A. Djouadi and J.L. Kneur, Z. Phys. **C57** (1993) 425.
- [7] J. Kühn and P.M. Zerwas, Phys. Lett. **B147** (1984) 189.
- [8] S. Myers and E. Picasso, Sci. Am. **C263** (1990) 54.
- [9] A. Blondel *et al.*, LEP Energy Working Group Collaboration, Eur. Phys. J. **C11** (1999) 573.
- [10] R. Assmann *et al.*, Eur. Phys. J. **C6** (1999) 187.
- [11] J. Prochnow, “The LEP energy spectrometer”, Diplommat Thesis, Rheinisch-Westfälischen Technischen Hochschule Aachen, PITHA-00-10, CERN-THESIS-2000-026.
- [12] K. Ahmet *et al.*, OPAL Collaboration, Nucl. Instr. Meth. **A305** (1991) 275.
- [13] S. Anderson *et al.*, Nucl. Instr. Meth. **A403** (1998) 326.
- [14] J.M. Roney *et al.*, Nucl. Instr. Meth. **A279** (1989) 236.

- [15] H.M. Fisher *et al.*, Nucl. Instr. Meth. **A252** (1986) 331;
R.-D. Heuer and A. Wagner, Nucl. Instr. Meth. **A265** (1988) 11.
- [16] H. Bethe and W. Heitler, Proc. Roy. Soc. Lond. **A146** (1934) 83;
F. Block and A. Nordsieck, Phys. Rev. **52** (1937) 54.
- [17] H. Mes *et al.*, Nucl. Instr. Meth. **A265** (1988) 445.
- [18] P.W. Jeffreys *et al.*, Nucl. Instr. Meth. **AA290** (1990) 76.
- [19] P. Mättig, OPAL Technical Note TN324, 1995.
- [20] G. Abbiendi *et al.*, OPAL Collaboration, “Multi-Photon Production in e^+e^- Collisions at 181-209 GeV”, submitted to Eur. Phys. J. C.
- [21] S. Dado *et al.*, Nucl. Instr. Meth. **AA252** (1986) 511;
G. Artusi *et al.*, OPAL Collaboration, Nucl. Instr. Meth. **AA279** (1989) 523.
- [22] G. Abbiendi *et al.*, OPAL Collaboration, Eur. Phys. J. **C13** (2000) 213.
- [23] R.J. Akers *et al.*, Nucl. Instr. Meth. **A357** (1995) 253.
- [24] See for example, R.Y. Rubinstein, “Simulation and the Monte Carlo Method”, John Wiley and Sons Inc., New York, 1981.
- [25] R. Brun *et al.*, GEANT3, CERN Report DD/EE/84-1 (1989).
- [26] S. Jadach, W. Placzek and B.F.L. Ward, Phys. Lett. **B390** (1997) 298.
- [27] D. Karlen, Nucl. Phys. **B289** (1987) 23.
- [28] S. Jadach, B.F. Ward and Z. Wąs, Phys. Lett. **B449** (1999) 97;
<http://home.cern.ch/~jadach/KKindex.html>;
S. Jadach, B.F.L. Ward and Z. Wąs, “The precision Monte Carlo Event Generator KK for two-fermion final states in e^+e^- Collisions”, hep-ph/9912214, Dec 1999;
Submitted to Comp. Phys. Comm.
- [29] T. Sjöstrand, Comp. Phys. Comm. **82** (1994) 74.
- [30] G. Montagna, O. Nicrosini and F. Piccinini, Comp. Phys. Comm. **98** (1996) 206.
- [31] F.A. Berends, R. Kleiss, Nucl. Phys. **B186** (1981) 22.
- [32] S. Jadach, W. Placzek, M. Skrzypek, B.F.L. Ward and Z. Wąs, Comp. Phys. Comm. **119** (1999) 272.
- [33] J. Fujimoto *et al.*, Comp. Phys. Comm. **100** (1996) 128.
- [34] R. Engel and J. Ranft, Phys. Rev. **D54** (1996) 4244.

- [35] G. Marchesini *et al.*, *Comp. Phys. Comm.* **67** (1992) 465.
- [36] R. Bhattacharya, J. Smith and G. Grammer, *Phys. Rev.* **D15** (1977) 3267;
J. Smith, J.A.M. Vermaseren and G. Grammer, *Phys. Rev.* **D15** (1977) 3280.
- [37] R. Tafirout and G. Azeulos, *Comp. Phys. Comm.* **126** (2000) 244.
- [38] A. Djouadi, *Comp. Phys. Comm.* **63** (1994) 317;
J.H. Kühn, A. Reiter and P.M. Zerwas, *Nucl. Phys.* **B272** (1986) 560.
- [39] OPAL Collaboration, R. Akers *et al.*, *Z. Phys.* **C63** (1994) 197.
- [40] G. Alexander *et al.*, OPAL Collaboration, *Z. Phys.* **C70** (1996) 357;
G. Abbiendi *et al.*, OPAL Collaboration, *Eur. Phys. J.* **C8** (1999) 217;
G. Abbiendi *et al.*, OPAL Collaboration, *Eur. Phys. J.* **C16** (2000) 41.
- [41] G. Arfken, “Mathematical Methods for Physicists”, third edition, Academic Press Inc., 1985, ISBN 0-12-059820-5.
- [42] J. Neyman, E.S. Pearson, *Biometrika*, **20A** (1928) 263.
- [43] M.G. Kendall and A. Stuart, “The Advanced Theory of Statistics”, Vol. 2, Charles Griffen and Company Limited, 1967, SBN 85264-011-0.
- [44] S.L. Meyer, “Data Analysis for Scientists and Engineers”, John Wiley and Sons, 1975, ISBN 0-471-59995-6.
- [45] G. Cowan, “Statistical Data Analysis”, Oxford University Press, 1998, ISBN 0-19-850156-2.
- [46] J. Neyman and E.S. Pearson, *Phil. Trans.* **A231** (1933) 289.
- [47] K. Cranmer, *Comp. Phys. Comm.* **136** (2001) 198.
- [48] G. Abbiendi *et al.*, OPAL Collaboration, *Phys. Lett.* **B499** (2001) 38.
- [49] S. Jadach, B. F. L. Ward and Z. Wąs, *Phys. Rev.* **D63** (2001) 113009.
- [50] R.D. Cousins and V.L. Highland, *Nucl. Instr. Meth.* **A320** (1992) 331.
- [51] G. Abbiendi *et al.*, OPAL Collaboration, *Eur. Phys. J.* **C14** (2000) 73.
- [52] K. Ackerstaff *et al.*, OPAL Collaboration, *Eur. Phys. J.* **C1** (1998) 45;
K. Ackerstaff *et al.*, OPAL Collaboration, *Phys. Lett.* **B391** (1997) 197;
G. Alexander *et al.*, OPAL Collaboration, *Phys. Lett.* **B386** (1996) 463.
- [53] D. Buskulic *et al.*, ALEPH Collaboration, *Phys. Lett.* **B385** (1996) 445.

- [54] B. Tome, *Int. J. Mod. Phys.* **A16S1B** (2001) 869;
P. Abreu *et al.*, DELPHI Collaboration, *Eur. Phys. J.* **C8** (1999) 41;
P. Abreu *et al.*, DELPHI Collaboration, *Phys. Lett.* **B393** (1997) 245;
P. Abreu *et al.*, DELPHI Collaboration, *Phys. Lett.* **B380** (1996) 480.
- [55] M. Acciarri *et al.*, L3 Collaboration, *Phys. Lett.* **B502** (2001) 37;
M. Acciarri *et al.*, L3 Collaboration, *Phys. Lett.* **B473** (2000) 177;
M. Acciarri *et al.*, L3 Collaboration, *Phys. Lett.* **B401** (1997) 139;
M. Acciarri *et al.*, L3 Collaboration, *Phys. Lett.* **B370** (1996) 211;
- [56] R. Barate *et al.*, ALEPH Collaboration, *Eur. Phys. J.* **C4** (1998) 571;
D. Decamp *et al.*, ALEPH Collaboration, *Phys. Lett.* **B250** (1990) 172;
D. Decamp *et al.*, ALEPH Collaboration, *Phys. Lett.* **B236** (1990) 501;
P. Abreu *et al.*, DELPHI Collaboration, *Z. Phys.* **C53** (1992) 41;
B. Adeva *et al.*, L3 Collaboration, *Phys. Lett.* **B252** (1990) 525;
B. Adeva *et al.*, L3 Collaboration, *Phys. Lett.* **B250** (1990) 205;
B. Adeva *et al.*, L3 Collaboration, *Phys. Lett.* **B247** (1990) 177;
M. Z. Akrawy *et al.*, OPAL Collaboration, *Phys. Lett.* **B244** (1990) 135.
- [57] A. Heister *et al.*, ALEPH Collaboration, “Single photon and multiphoton production in e^+e^- collisions at \sqrt{s} up to 209 GeV”, CERN-EP-2002-033, submitted to *Eur. Phys. J. C*;
D. Abbaneo *et al.*, ALEPH, DELPHI, L3 and OPAL Collaborations, “A combination of preliminary electroweak measurements and constraints on the Standard Model”, hep-ex/0112021.
- [58] C. Adloff *et al.*, H1 Collaboration, *Eur. Phys. J.* **C17** (2000) 567;
S. Aid *et al.*, H1 Collaboration, *Nucl. Phys.* **B483** (1997) 44;
I. Abt *et al.*, H1 Collaboration, *Nucl. Phys.* **B396** (1993) 3.
- [59] S. Chekanov *et al.*, ZEUS Collaboration, hep-ex/0109018, submitted to *Phys. Lett. B*;
J. Breitweg *et al.*, ZEUS Collaboration, *Z. Phys.* **C76** (1997) 631;
M. Derrick *et al.*, ZEUS Collaboration, *Z. Phys.* **C65** (1995) 627;
M. Derrick *et al.*, ZEUS Collaboration, *Phys. Lett.* **B316** (1993) 207.
- [60] P. Mery, S. E. Moubarik, M. Perrottet and F. M. Renard, *Z. Phys.* **C46** (1990) 229;
F. M. Renard, *Phys. Lett.* **B116** (1982) 264;
S. J. Brodsky and S. D. Drell, *Phys. Rev.* **D22** (2236) 1980.
- [61] P. J. Mohr and B. N. Taylor, *Rev. Mod. Phys.* **72** (2000) 351.
- [62] H. N. Brown *et al.*, Muon g-2 Collaboration, *Phys. Rev. Lett.* **86** (2001) 2227.

- [63] O. J. Eboli, S. M. Lietti and P. Mathews, Phys. Rev. **D65** (2002) 075003.
- [64] The LHC Study Group, “The Large Hadron Collider Conceptual Design”, CERN/AC/95-05, 1995.
- [65] E. M. Gregores, M. C. Gonzalez-Garcia and S. F. Novaes, Phys. Rev. **D56** (1997) 2920.
- [66] R.K. Bock *et al.*, “Formulae and Methods in Experimental Data Evaluation with Emphasis on High Energy Physics”, Volume 3, European Physical Society, 1983; R.K. Bock *et al.*, “Data Analysis Techniques for High-Energy Physics Experiments”, Cambridge University Press, 1990.
- [67] A.L. Read, “Modified Frequentist Analysis of Search Results (The CL_s Method)”, in proceedings of the 1st Workshop on Confidence Limits, CERN-OPEN-2000-205, Geneva 2000, 81-101.
- [68] T. Junk, Nucl. Instr. Meth. **A434** (1999) 435.
- [69] P. Abreu *et al.*, DELPHI Collaboration, Phys. Lett. **B491** (2000) 67;
G. Abbiendi *et al.*, OPAL Collaboration, Phys. Lett. **B465** (1999) 303;
D. Buskulic *et al.*, ALEPH Collaboration, Phys. Lett. **B384** (1996) 333.
- [70] A. Litke, “Experiments with electron-positron colliding beams”, Ph.D. thesis, Harvard University, 1970.

VITA

Surname: Vachon
Given Names: Brigitte Marie Christine
Place of Birth: Ste-Marie de Beauce, Québec, Canada

Educational Institutions Attended:

University of Victoria	1998-2002
McGill University	1994-1997

Degree Awarded:

B.Sc. (Honours Physics)	McGill University	1997
-------------------------	-------------------	------

Honours and Awards:

NSERC Postdoctoral Fellowship	2002
Charles S. Humphrey Graduate Student Award, University of Victoria	2001-2002
NSERC Postgraduate Research Scholarship (PGSB)	2001-2002
President Research Scholarship, University of Victoria	1999-2002
NSERC Postgraduate Research Scholarship (PGSA)	1999-2001
Petch Research Scholarship, University of Victoria	1999
Best Graduate Student Presentation Award at Western Regional Nuclear and Particle Physics Conference, Lake Louise, Alberta	1999
University of Victoria Entrance Award	1998
FCAR Postgraduate Research Scholarship	1997-1999
E.R. Pounder prize in physics, McGill University	1997
James McGill Entrance Scholarship, McGill University	1994
Canadian Merit Scholarship Foundation	1994
Governor's medal for academic excellence	1992

Publications:

1. G. Abbiendi *et al.*, OPAL Collaboration,
“Search for charged excited leptons in e^+e^- collisions at $\sqrt{s} = 183\text{-}209$ GeV”,
CERN-EP/2002-043, accepted for publication in Phys. Lett. B.
2. B. Vachon, “Search for exotics and extra dimensions at LEP”,
To be published in the proceedings of the 16th International Workshop on High
Energy Physics and Quantum Field Theory, Moscow, Russia, hep-ex/0201029.
3. B. Vachon, “Search for heavy and excited leptons at LEP”,
Nucl. Phys. B (Proc. Suppl.) **98** (2001) 148.
4. G. Abbiendi *et al.*, OPAL Collaboration,
“ W^+W^- production and triple gauge boson couplings at LEP energies up to 183 GeV”,
Eur. Phys. J. C **8** (1999) 191.

UNIVERSITY OF VICTORIA PARTIAL COPYRIGHT LICENSE

I hereby grant the right to lend my dissertation to users of the University of Victoria Library, and to make single copies only for such users or in response to a request from the Library of any other university, or similar institution, on its behalf or for one of its users. I further agree that permission for extensive copying of this thesis for scholarly purposes may be granted by me or a member of the University designated by me. It is understood that copying or publication of this thesis for financial gain shall not be allowed without my written permission.

Title of Dissertation:

Search for Excited Charged Leptons in Electron-Positron Collisions

Author: _____

Brigitte Marie Christine Vachon

July 13, 2006